Raman Spectroscopy of Librons and Phonons in Crystalline C_{60}

by

Peter J. Horoyski
B.Sc., University of Guelph, 1991

Thesis submitted in partial fulfillment of
the requirements for the degree of
DOCTOR OF PHILOSOPHY
in the Department of
PHYSICS

Simon Fraser University
January 1996

ISBN 0-612-16923-5

PARTIAL COPYRIGHT LICENSE

I hereby grant to Simon Fraser University the right to lend my thesis, project or extended essay (the title of which is shown below) to users of the Simon Fraser University Library, and to make partial or single copies only for such users or in response to a request from the library of any other university, or other educational institution, on its own behalf or for one of its users. I further agree that permission for multiple copying of this work for scholarly purposes may be granted by me or the Dean of Graduate Studies. It is understood that copying or publication of this work for financial gain shall not be allowed without my written permission.

Title of Thesis/~~Project/Extended Essay~~

Raman Spectroscopy of Librons and Phonons in Crystalline C60.

Author:
(signature)

(name)

15 January 1996
(date)

APPROVAL

Name: Peter J. Horoyski

Degree: Ph. D. (Physics)

Title of Thesis: Raman Spectroscopy of Librons and Phonons in Crystalline C_{60}

Examining Committee:

Chairman: Dr. J. R. Dahn

Dr. M. L. W. Thewalt
Senior Supervisor

Dr. J. C. Irwin

Dr. S. P. Watkins

Dr. A. E. Curzon

Dr. T. Timusk
Department of Physics,
McMaster Univeristy
External Examiner

Date Approved: Jan 16, 1996

ABSTRACT

A new era of carbon research has appeared virtually overnight following the 1985 discovery of the fullerenes and the development in 1990 of an efficient means for their production. Considerable theoretical and experimental activity has been focused on C_{60}, the most symmetrical and readily available member of the fullerene family, particularly the vibrational and rotational dynamics of its solid state phase.

In this thesis, the phonon spectrum of crystalline C_{60} is studied using the technique of Raman spectroscopy. The Raman-active intramolecular phonons are shown to be richly-structured, revealing crystal field splittings of the molecular vibrations both above and below the 260 K order-disorder phase transition temperature. Surprisingly, the majority of the vibrational fine-structure is shown to be dependent upon the presence of merohedral disorder (misoriented molecules) within the ordered phase. The influence of isotopic disorder arising from C_{60} made from naturally abundant carbon is revealed to be a minor one through the use of isotopically engineered crystals. The exception to this behaviour is the $A_{g(2)}$-derived phonon, in which a complex interaction between solid state and isotopic effects is seen.

The first optical detection of libron modes (orientational excitations of the crystal) in solid C_{60} is reported. Greater structure is seen within the Raman-active lattice mode spectrum than would be expected from a group-theoretical analysis of the ordered phase. The additional structure is proposed to stem from the orientational disorder of the low-temperature phase.

This thesis also presents the discovery of a new, metastable phase of solid C_{60}. The new structure is heralded by pronounced changes within the intramolecular and intermolecular mode fine-structure with the application of hydrostatic pressure. While the new phase is stabilized by high pressures, it remains metastable with respect to the conventional low-pressure structure of solid C_{60} provided the crystal is kept below ~90K, the orientational glass transition temperature. A model based upon a pressure-induced orientational reordering of the molecules is proposed for the metastable phase.

ACKNOWLEDGMENTS

I gratefully acknowledge the support of my supervisor, Dr. Mike Thewalt; the fruition of this project was made possible only through his interest, guidance, and unflagging assistance. I count myself lucky for having worked with him, and thank him for trying to impart to me a small measure of his knowledge of physics, lab wizardry, and pacman-playing skills.

I wish to thank Dr. Jeff Wolk for his contributions to the hydrostatic pressure experiments. Jeff's assistance was invaluable, both because of his experience in the technique of high-pressure spectroscopy, and because of his good form when sapphires cracked on weekends or late nights.

Thanks to Dr. Tom Anthony, GE Research & Development, who supplied the isotopically enriched graphite rods which were used as starting material for the isotopically engineered C_{60} crystals. Without Dr. Anthony, the isotope studies would, in all likelihood, not have taken place.

Financial support from the Natural Sciences and Engineering Research Council, Simon Fraser University, Newport Inc., Petro-Canada, and Dr. Thewalt is gratefully acknowledged. I am also indebted to Cambridge Isotope Labs which supplied the isotopically enriched methane gas.

A special thank you to my parents for their unwavering support and love. Most of all, I wish to thank Sue for, well, everything (in particular, enduring the writing of this thesis).

TABLE OF CONTENTS

LIST OF FIGURES

LIST OF TABLES

CHAPTER 1

INTRODUCTION

1.1 A New Form of Carbon: The Fullerenes

Since antiquity, carbon has been subjected to far more study than all the other elements taken together. Millions of carbon-containing compounds are known, but only two pure-carbon allotropes were thought to exist: graphite and diamond. Then in 1985, the fullerenes, a third allotrope and the first molecular forms of carbon, were discovered.

The fullerenes are a family of closed carbon-cage clusters, discovered by Kroto and Smalley [85K] using a laser-vaporization cluster beam apparatus. This technique consisted of laser ablating a graphite target and cooling the resultant plasma in a supersonic helium jet. Mass spectroscopy of the carbon clusters in the jet revealed an abundant distribution of even-numbered cluster sizes from ~C_{32} to well beyond C_{100}, the dominant species being C_{60}. The appearance of only even-numbered species stemmed from the clusters being closed cages of carbon formed from hexagons and pentagons. The closed carbon-cage can be thought of as a "rolled-up" graphene sheet (a single layer of crystalline graphite) with pentagon "defects" which allow for curvature of the sheet. The most symmetrical of the cages is C_{60}, shown in Figure 1.1. This soccer-ball, or truncated icosahedron shape of C_{60} was first proposed by Kroto and Smalley [85K] who dubbed the molecule "Buckminsterfullerene", and the family of higher weight closed-cage molecules "fullerenes", because of their resemblance to the geodesic domes designed and built by R. Buckminster Fuller.

In the fall of 1990, Krätschmer, Huffman, and co-workers [90K] developed a simple method for synthesizing gram-sized quantities of C_{60} which previously had only been available in trace quantities in the gas phase [85K]. They showed that a carbon arc-

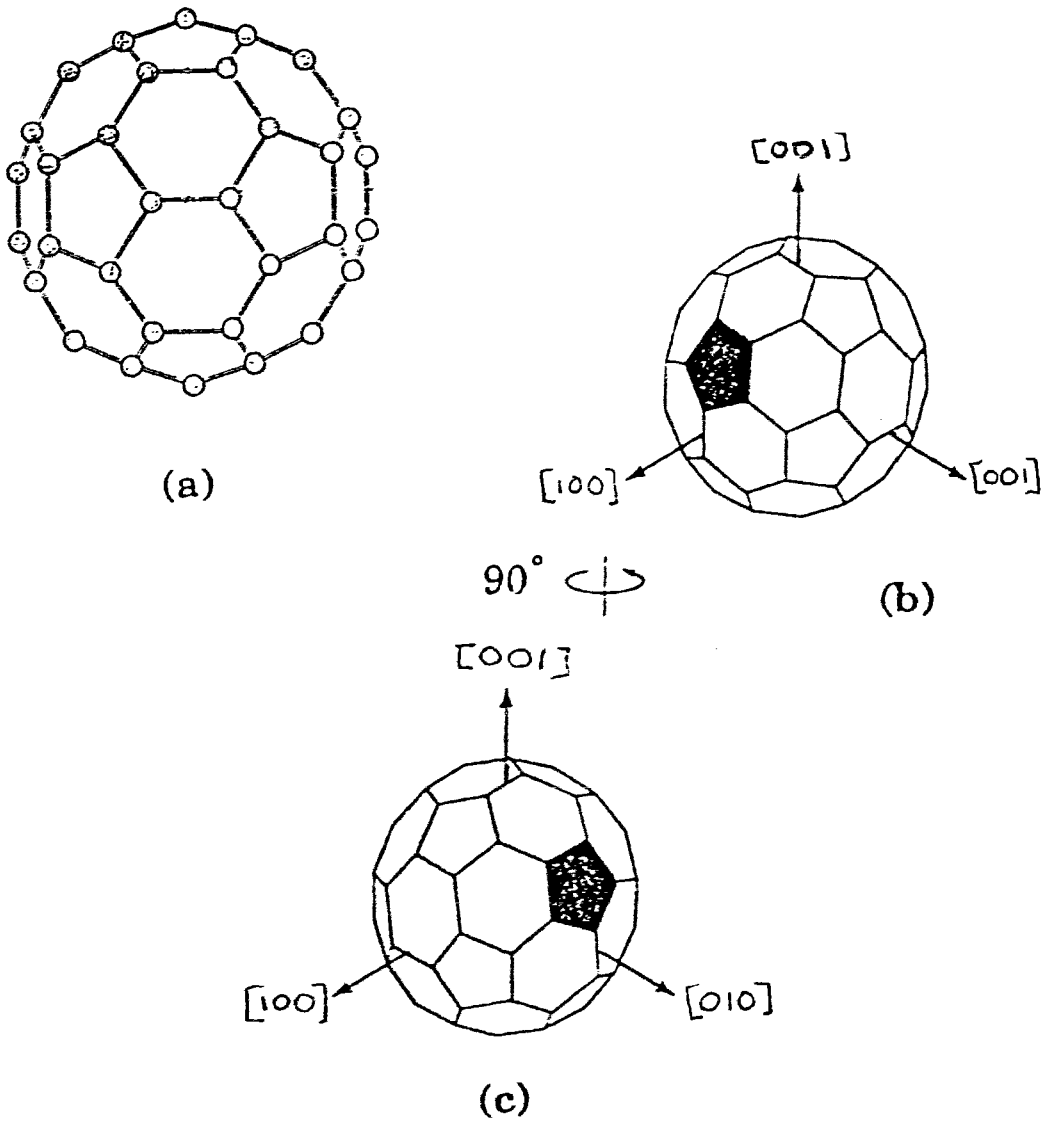

Fig. 1.1 a) Truncated icosahedron structure of the C_{60} molecule. b) the "standard orientation" of the molecule, in which two-fold and three-fold molecular axes are aligned with [100] and [111] cubic crystal axes, respectively. c) The second unique "standard orientation" which is arrived at by rotating the molecule 90° about <010> or <001>.

discharge in a helium atmosphere would generate carbon soot which contained up to 15% C_{60}. The fullerenes were found to be soluble in benzene, which led to a new solid form of pure carbon: crystalline C_{60}. Thin, flake-like crystals deposited from an evaporated solution of C_{60} in benzene provided the first view of this new form of solid [90K]. It was also reported [90K] that C_{60} would readily sublime at temperatures above 400°C, allowing for vapour-transport growth of larger crystals, formed free of any residual solvents. Purification of C_{60} from its higher weight cousins (most notably C_{70}) can be readily achieved by liquid chromatography, using a range of non-polar solvents such as toluene, benzene, and hexane [90A, 90T].

The large-scale C_{60} production method of Krätschmer and co-workers was quickly taken up by many other groups who in turn proved beyond any doubt that the proposal made by Kroto, Smalley, and co-workers of a soccer-ball shaped C_{60} molecule was correct.

A new era of carbon chemistry, physics, and materials science has followed almost overnight the discovery of the fullerenes and the development of an efficient means for their production. The large family of new compounds which can be prepared from the fullerenes has attracted tremendous interest from the chemistry community. Fullerene-derived solids are equally exciting to physicists and materials scientists; the fullerenes represent a source of mono-disperse nanostructures that can be assembled in film and crystal form, and whose properties can be tremendously altered by doping and intercalation.

1.2 C_{60} as a Molecular Solid

In the solid state, the C_{60} molecules (whose mean molecular diameter is 6.83 Å) crystallize into a cubic structure with a lattice constant of 14.17 Å [91D,91F,91H]. At room temperature, the molecules are arranged on a face centered cubic (fcc) lattice with one C_{60} molecule per primitive fcc unit cell, or four molecules per simple cubic (sc) unit

cell [91F]. A variety of experimental techniques, including NMR [91T,91Tb] and μSR measurements [92K], revealed that while the centers-of-mass of the C_{60} molecules remain on fcc lattice sites, the molecules rotate freely with no time-averaged preferred orientation in space. Rotational correlation times at room temperature are 9-12 ps, only three to four times longer than expected for unhindered gas phase rotation, and faster than any other known solid state rotator. Thus the high-temperature description of crystalline C_{60} is that of a prototypical molecular crystal: well-defined translational order with a smooth rotational potential with many shallow minima, leading to continuous molecular reorientations. The space group of the high-temperature phase is $Fm\bar{3}m$ or O_h^5 [91F,91S].

Below 260 K, the rotational dynamics of the C_{60} molecules become more complicated. A first-order orientational phase transition occurs at 260 K, in which the C_{60} molecules assume preferred orientations in the crystal. In this phase the C_{60} molecules remain on fcc lattice sites but the four molecules of the conventional fcc unit cell become orientationally inequivalent. Thus, while the molecules remain on fcc lattice sites, the structure becomes sc with a four molecule basis. The crystal structure is $Pa\bar{3}$ or T_h^6, as determined first by powder x-ray diffraction [91H] and later confirmed by single crystal x-ray diffraction [91L], neutron powder diffraction [91D], and electron diffraction [92T,92Y].

In order to describe the orientational ordering of solid C_{60}, we imagine putting all the molecules in the lattice in the same "standard orientation" with respect to the cubic crystal lattice, as shown in Fig. 1.1. In the standard orientation, <100> crystal axes pass through three orthogonal hexagon-hexagon, or "6:6" edges. As can be seen in Fig. 1.1, the axes which r ss through the hexagon-hexagon bonds are two-fold symmetry axes of the molecule. A consequence of the icosahedral molecular symmetry is that this alignment also orients three-fold molecular symmetry axes with <111> crystal directions. There are actually two such standard orientations in which the <100> crystal axes are

two-fold symmetry axes of the molecule and the <111> crystal axes are three-fold symmetry axes. The second standard orientation, also shown in Fig. 1.1, is arrived at by a 90° rotation of the first orientation about a <100> direction. To construct the low temperature (T < 260 K) crystal structure, we start with all four molecules of the sc unit cell in one of the two standard orientations. Each molecule is then rotated by an angle Γ about one of the <111> axes (there are four such axes, one for each molecule of the sc unit cell). The angle Γ through which each molecule is rotated is not fixed by symmetry, and is experimentally determined to be in the range of 22-26° [91D,91S,92D]. A unit cell of the ordered phase is shown in Fig. 1.2.

The origin of this orientational ordering lies in recognizing that the C_{60} molecules, while highly symmetric, are not smooth polarizable spherical shells attracting one another via a purely van der Waals interaction. A C_{60} molecule is a granular structure made up of covalently bonded atoms. Moreover, the bond lengths within the molecule are not uniform. The bonds which form the pentagons on the molecule are longer single bonds while those between two contiguous hexagons are shorter double bonds [91D]. This non-uniform charge distribution contributes an orientation-dependent electrostatic component to the predominantly van der Waals intermolecular potential. The electrostatic interactions are stabilized by a ~22° rotation because such a rotation places electron-rich double bonds fusing two hexagons immediately adjacent to electron-poor pentagon faces of nearest-neighbour molecules [92D]. Such an alignment is shown schematically in Figure 1.2. Detailed numerical calculations [92L,92S] have in fact shown that a Lennard-Jones model of the van der Waals interaction does not lead to the $Pa\bar{3}$ ground state, while the addition of an *ad hoc* bond-centered Coulomb potential does stabilize the $Pa\bar{3}$ structure and gives reasonable agreement with other experimentally observed properties such as the rotational melting temperature and the pressure dependence of the transition temperature.

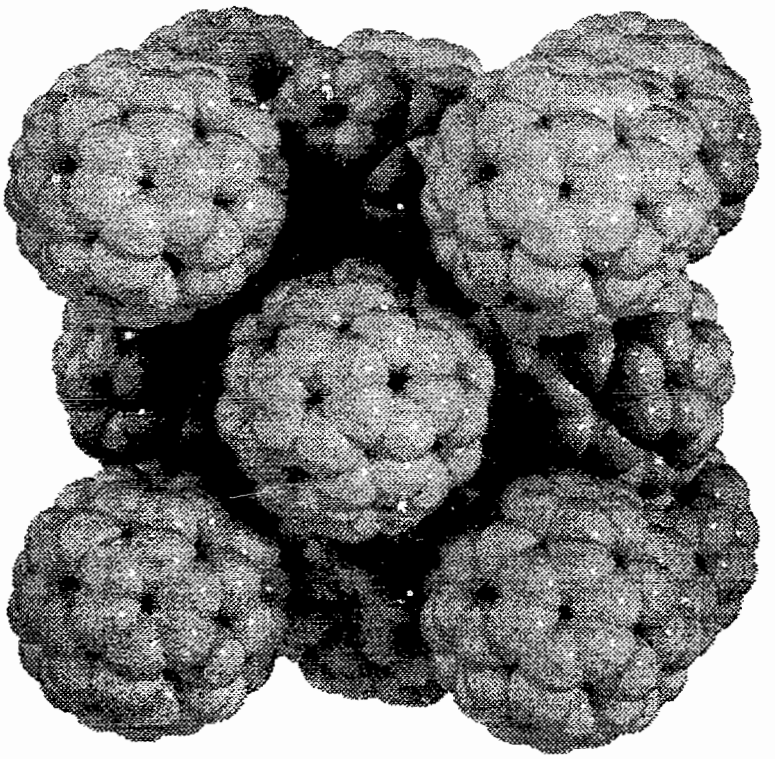

Figure 1.2 A unit cell of the low-temperature phase of solid C_{60}. If the molecules were rotating freely, the crystal structure would be face centered cubic; the orientational ordering of the molecules leads to a simple cubic structure with four inequivalent molecules per unit cell. The ordering of the molecules places the electron-rich double bonds fusing two contiguous hexagons of a molecule (B) opposite the electron-deficient pentagon faces of neighbouring molecules (A), as shown schematically.

Since the ground state is reached by orienting the molecules such that the electron-rich double bonds of one molecule are adjacent to electron-deficient *pentagon* faces of neighbouring molecules, a second orientation in which the double bonds of a molecule are adjacent to neighbouring *hexagon* faces should also be an energetic local minimum. This leads to the possibility of two rotation angles, Γ_1 and Γ_2 for the low temperature structure of solid C_{60}. Shown in Figure 1.3 is a theoretical model of the rotational potential energy of a C_{60} molecule as it is rotated by an angle Γ about a [111] axis (taken from Ref. 92L). The model uses an atom-centered Lennard-Jones potential plus a bond-centered Coloumb potential. The zero of the Γ axis corresponds to the molecule in the standard orientation, while the global and local minima at $\Gamma_1 \sim 23°$ and $\Gamma_2 \sim 83°$ correspond to the electron-rich double bonds of the molecule adjacent to the electron-deficient pentagon or hexagon faces of nearest neighbours, respectively. As can be seen from Fig. 1.3, a large rotational energy barrier of approximately 250 meV between the global and local minima sets the energy scale for reorientations between these two configurations, while the predicted difference in energy, approximately 100 meV, controls the temperature dependent populations.

The theoretical modeling shown in Fig. 1.3 corroborates earlier experimental work which found the low-temperature phase was not completely ordered. To fit x-ray diffraction [92H] and neutron scattering [92D] data of the low-temperature phase, a significant fraction of disorder in the form of a second molecular orientation was needed. The best fit incorporated the majority of the molecules in the $\Gamma_1 \sim 23°$ orientation and approximately 17% of the molecules in the $\Gamma_2 \sim 83°$ orientation at 15 K. Models incorporating an adjustable fraction of molecules with *random* orientations were also examined and shown to provide a substantially worse fit.

The amount of disorder in the crystal is not a static quantity below 260 K, as the molecules are able to make thermally-activated reorientations. Shown in Figure 1.4 is the temperature evolution of the disorder in the crystal as determined by neutron

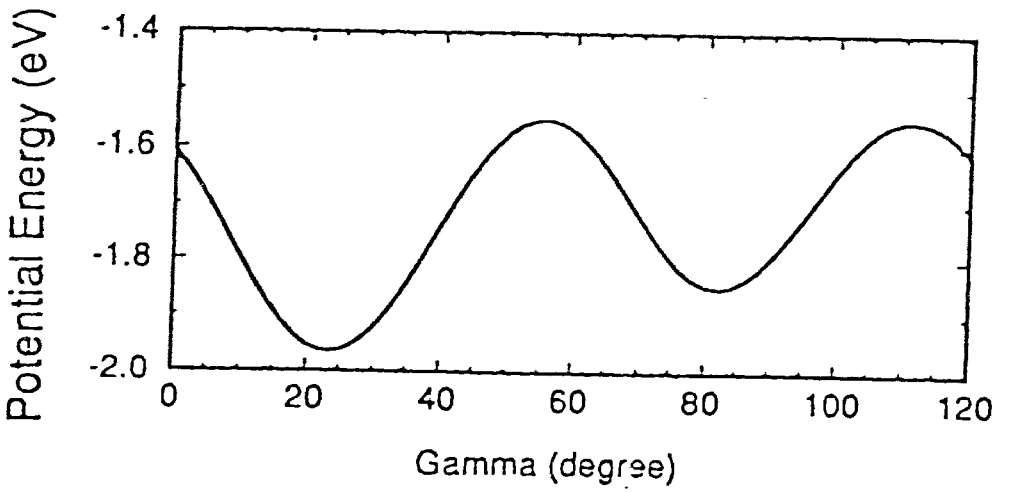

Fig. 1.3 Model orientational potential energy of a single molecule (in the low-temperature, ordered phase) as it is rotated through an angle Γ about a [111] axis (taken from Ref. 92L). The global minimum at ~22° places the double bonds of the molecule opposite pentagon faces of neighbouring molecules, while the local minimum at ~83° places the double bonds opposite hexagon faces of neighbouring molecules.

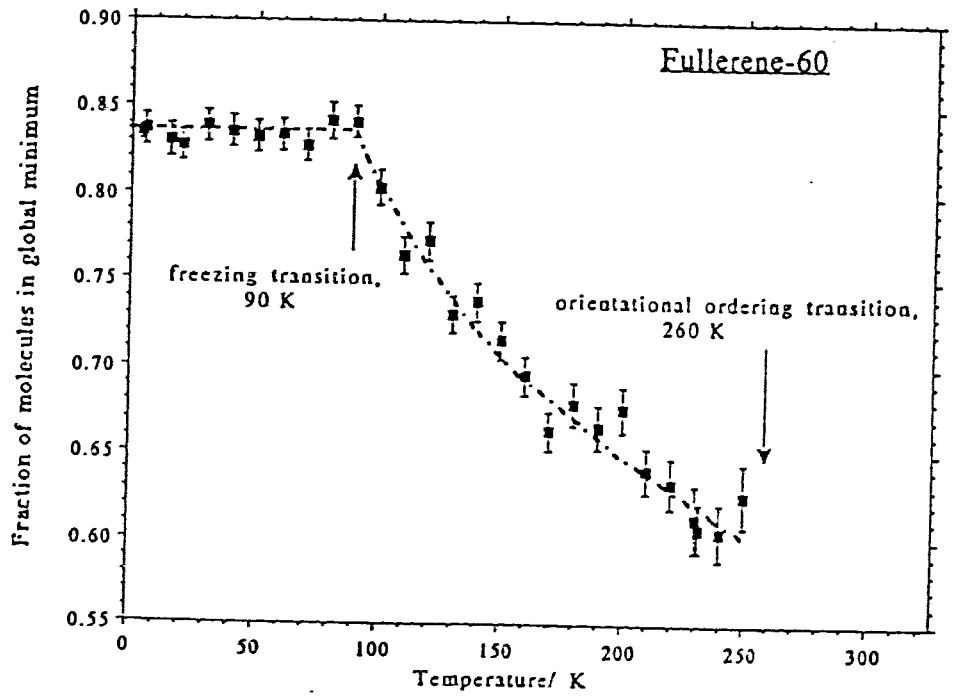

Fig. 1.4 Temperature variation of the fraction of C_{60} molecules locked into the "pentagon orientation" (taken from Ref. 92D).

diffraction [92D]. The fraction of molecules in the ordered orientation (a rotation of Γ_1 from the standard position) increases smoothly from its value of ~60% just below the order-disorder transition at 260 K to a maximum value of approximately 83% at ~90 K, below which temperature it remains constant. The structure of solid C_{60} below ~90 K is therefore described as an orientational glass; a finite amount of orientational disorder is frozen in as the thermal energies become much smaller than the rotational barriers. The orientational disorder of solid C_{60} is also referred to as 'merohedral' disorder [92H], to emphasize the fact that the molecules are distributed amongst a finite number of distinct, rather than continuously random, orientations.

In the intermediate temperature range (90-260 K), where the amount of disorder is in thermal equilibrium, the fraction of the crystal which is in the ordered state will be governed by the energy difference ΔE between the two nearly degenerate configurations. More precisely, the ordered fraction, p, will be given by (assuming the degeracies of the two energy levels is equal):

$$p = \frac{1}{1 + \exp(-\Delta E / kT)} \qquad (1.1)$$

Fitting equation 1.1 to the data shown in Fig. 1.4 gives an energy difference ΔE of 11.4 meV [92P], a value which is an order of magnitude smaller than that predicted by the numerical calculations illustrated in Fig. 1.3.

The coexistence of two energetically favourable orientations has been subsequently confirmed by high-resolution dilatometry [92G], sound velocity and attenuation [92Sb], and thermal conductivity [92Yb] measurements of single-crystal C_{60}. In these studies, the activation energy for reorientation between the two states is found to be 250-300 meV, while the energy difference of the two states is found to be 10-15 meV, in good agreement with the value extracted from fitting the temperature dependence of the diffraction data.

The amount of merohedral disorder in the ordered phase has been shown to be pressure dependent as well as temperature dependent [93D]. The Γ_2 orientation (in which the double bonds of the molecule face neighbouring hexagons) becomes energetically favourable over that of the Γ_1 orientation (in which the double bonds of the molecule face neighbouring pentagons) with the application of hydrostatic pressure due to the smaller volume of the Γ_2 orientation. Using the technique of neutron diffraction, David and Ibberson [93D] showed that at 150 K the proportion of Γ_2 oriented molecules increased from approximately 30% at 0 kbar to 60% at 3 kbar. Assuming the energy difference between the two orientations continues to increase with increasing pressure, there should exist a region in the pressure-temperature phase diagram of solid C_{60} in which virtually all of the crystal is in a single orientation. The use of hydrostatic pressure, therefore, holds the promise of providing researchers with a completely ordered phase of C_{60}.

1.3 Vibrational Spectroscopy of Crystalline C_{60}

The bulk measurements discussed in Section 1.2 have provided a wealth of structural information on the solid phase of C_{60}. Further elucidation of the intermolecular interactions is possible through the technique of vibrational spectroscopy. The atomic vibrations of the crystal arise from, and are governed by the intra- and intermolecular potentials. Vibrational spectroscopy therefore provides a microscopic probe of the forces which dictate the rotational dynamics and orientational ordering of the solid state.

The C_{60} molecule, due to its large number of constituent atoms, could have a daunting number of normal-mode vibrations. Fortunately, the high symmetry of the molecule (I_h) leads to a tremendous degeneracy within the vibrational spectrum of an isolated molecule; of the 174 (3x60 - 6) normal modes of vibration, only 46 non-

degenerate modes arise, which can be classified using the I_h point group as follows [90B]:

$$\Gamma_{vib} = 2A_g + 3F_{1g} + 4F_{2g} + 6G_g + 8H_g + A_u + 4F_{1u} + 5F_{2u} + 6G_u + 7H_u \quad (1.2)$$

Of these 46 fundamentals, only four (F_{1u}) are infra-red active and ten ($2A_g$ and $8H_g$) are Raman-active, leaving 32 optically inactive modes.

In the solid state, the phonon spectrum is dominated by these internal vibrations of the molecules. The loss of molecular identity is very small in van der Waals crystals and the internal vibrations are, to a first approximation, little changed upon condensation into the solid state. There are forces between the molecules of course - otherwise the material would never crystallize. The most obvious impact of this intermolecular potential is the creation of lattice, or external modes - translational and rotational motions of the molecular units. While there are no optical branches of the lattice modes at room temperature (only one molecule per primitive cell), optically-active translational phonons are present in the low-temperature phase. Since *orientational* order as well as *translational* order exists in the low-temperature phase, optically-active librons (quasi-rotational phonons) will also be present. The 12 libron modes (3 x 4 molecules per unit cell) are all of gerade symmetry (even under inversion) and so are Raman-active [92Yc]. The 9 translational phonons (3 x 4 molecules per unit cell minus 3 acoustic branches) are all of ungerade symmetry (odd under inversion) and so are infra-red active [92Yc]. Since solid C_{60} is a centro-symmetric crystal, no vibration is expected to be active in both Raman scattering and infrared absorption, which allows the complementary techniques of Raman scattering and infrared absorption to provide a clear delineation between the librons and translational phonons. As the external modes owe their entire existence to the intermolecular potential, they provide an excellent benchmark for the testing of present and future theoretical descriptions of the intermolecular forces.

Unfortunately, the large mass and moment of inertia of the molecules, combined with a relatively weak intermolecular potential, leads to external modes energies which are extremely small. In contrast to the intramolecular vibrations which span an energy range of 260 cm^{-1} to ~1600 cm^{-1}, numerical calculations based upon the model potential outlined in section 1.2 give libron mode energies in the range of 7-20 cm^{-1}, and translational phonon energies in the range of 30-45 cm^{-1}. This is an extremely difficult energy region to study, both in infra-red absorption and Raman scattering. Witness to this fact is the existence of several erroneous experimental reports of Raman scattering from librons [92Lb,92Lc,93M] and infra-red absorption measurements of the translational phonons [92Hb]. Inelastic neutron scattering (INS) measurements of single crystal [92Pb] and powder [92N] samples of C_{60} have measured weak, broad features at ~20, 29, and 37 cm^{-1} but the inherently low energy resolution of INS, the poor signal-to-noise of these measurements due to the unavailability of large samples, and the absence of optical selection rules to distinguish between gerade and ungerade modes makes comparison of these results with theory difficult.

As mentioned earlier, the internal vibrations of the C_{60} molecules are, to a first approximation, unaffected by the condensation of the molecules into a solid. The minimum separation between any pair of atoms on different C_{60} molecules is large compared with the carbon-carbon covalent bond length (~1.4 Å) [91D], supporting the interpretation of crystalline C_{60} as a typical molecular crystal. But while the influence of intermolecular forces on the internal modes may be small in magnitude, it is nonetheless present. The crystal environment is of a lower symmetry than that of an isolated molecule, leading to a static field splitting of the molecular modes. The vibrations which were degenerate under the I_h symmetry of the molecule can be both shifted in frequency and split by the crystal field. The static crystal field should also lead to the Raman-activation of all the gerade modes of an isolated C_{60} molecule [92Dc]. In addition to the static field splitting, in the ordered phase of the crystal, a correlation field splitting due to

interactions with internal vibrations of other molecules in the same unit cell of the crystal should lead to further splittings of the vibrational bands. Both degenerate and non-degenerate vibrations of the molecule may be split, since the potential energy will differ as the vibrations are in phase, or partly out of phase in the unit cell. Over and above these influences of an ordered crystal environment, the seemingly unavoidable inclusion of orientationally disordered molecules in the low-temperature phase (see Section 1.2) should also be reflected in the vibrational spectrum of solid C_{60}.

Needless to say, the magnitudes of the splittings induced by the crystal field cannot be arrived at purely from symmetry arguments - detailed numerical calculations are required, based upon model intra- and intermolecular potentials. However, the vast majority of theoretical studies of the vibrational spectrum of C_{60} have dealt with the intramolecular bonding only. A large variety of treatments have been undertaken to account for the internal vibrations of the C_{60} molecule [87W, 88W, 89W, 92F, 92J, 92Jb, 92Nb, 92O, 93S, 93W], and have been compared with the experimentally determined vibrational energies of solid C_{60} [91C, 91P, 92C, 92Db, 92Lb, 92Lc, 93Db, 93M, 93Wb]. This has lead to the identification of all the coarse features of the vibrational spectrum of solid C_{60}, including the weakly-activated modes, but obviously does not provide any information on the crystal field splittings of the modes. One theoretical calculation of the vibrational spectrum has been recently reported, in which the intra- and intermolecular forces are dealt with in a unified approach [93Y]. Band structures for all of the C_{60} phonons (both external and internal vibrations) were calculated. In this study, strong dispersions of most of the lower energy phonons (< 600 cm^{-1}) was predicted. For example, the lowest energy intramolecular mode at ~265 cm^{-1} was predicted to split into a broad band with a bandwidth of about 20 cm^{-1}.

None of the inelastic neutron scattering studies of crystalline C_{60} reported to date have detected a measurable splitting of the internal modes. Several recent Raman scattering studies have measured splittings of a small number of intramolecular

modes [92Lb,92Lc,93M] along with the weak activation of many additional first-order modes [93Db]. The origin of these splittings and weak activations remains open to debate, however. The reported Raman studies were all carried out using solid C_{60} fabricated from naturally abundant carbon. Naturally abundant carbon contains 1.11% ^{13}C, which implies that nearly half of all the C_{60} molecules formed from natural carbon will contain at least one ^{13}C atom. While a mass shift of 1 part in 720 is a small perturbation, the presence of a ^{13}C atom represents a dramatic reduction in the symmetry of the molecule. The splittings of the molecular modes and the weak activation of many other gerade modes seen in Raman scattering may stem from this isotopic disorder rather than a crystal field effect. Also unknown is the contribution of orientational disorder to the observed splittings.

1.4 Relevance of this Work.

In this thesis, the intramolecular phonons and intermolecular librons and phonons of crystalline C_{60} are studied using Raman spectroscopy. The first optical measurements of the libron modes, the rotational excitations of the lattice, are presented in Chapter 3. The lowest energy mode seen is at 18.5 cm^{-1} at 10 K, a value which is more than double the energy predicted by early theoretical treatments of the intermolecular potential. The low-energy bands seen in Raman scattering are unequivocally assigned to lattice modes of the solid by fabricating isotopically pure $^{12}C_{60}$ and $^{13}C_{60}$ single crystals and observing the mass shift of the bands. The libron bands are richly structured at low temperature, and contain more than five modes (the number expected from a group-theoretical analysis of the low-temperature phase). The additional fine-structure in the libron bands does not arise from isotopic disorder, as determined by a comparison between natural C_{60} and isotopically pure $^{12}C_{60}$ crystals. Through a series of quench-rate experiments, in which differing amounts of residual orientational disorder are incorporated into the crystal at a fixed temperature, the orientational disorder of the solid is shown to influence the

energies and intensities of the libron modes. It is proposed, therefore, that the appearance of additional modes in the Raman spectrum stems from this orientational disorder.

In Chapter 4, a high-resolution Raman scattering study of the intramolecular mode spectrum of crystalline C_{60} is presented. The linewidths of many of the internal phonons are shown to be an order of magnitude narrower than previously reported, permitting the discovery of splittings of many of these modes. In addition to the first report of splittings of many of these internal modes, Chapter 4 presents the only experimental study of the intramolecular phonons in which the influences of isotopic and orientational disorder are delineated from that of the crystal field of the ordered solid. While clear evidence of simple crystal field splittings are observed in the low-temperature phase (as well as in the high-temperature, freely rotating phase), a large fraction of the phonon fine-structure is shown to arise from the presence of merohedral disorder. By comparing the spectra of natural and isotopically enriched crystals, the effect of isotopic disorder on the intramolecular phonon spectrum is proven to be a minor one, except for the $A_g(2)$ mode. The $A_g(2)$ mode of crystalline C_{60} displays a complex dependence on the isotopic content and orientational disorder of the molecules which is presently not well-understood.

In Chapter 5, a new metastable phase of crystalline C_{60} is reported, stabilized by hydrostatic pressure. At pressures as low as 2 kbar, the normal low-temperature sc phase is metastable with respect to a new structure which manifests itself through very pronounced changes in the Raman-active intermolecular and intramolecular phonon spectra. The new phase appears when the pressurized sample is warmed above a minimum temperature. Once formed, the pressure can be subsequently released and the new phase will remain metastable with respect to the conventional low-pressure sc phase, provided the crystal is cooled below the (zero pressure) glass transition prior to releasing the pressure. It will be shown that the most probable explanation for these changes is a purely orientational transformation resulting from the pressure-induced lowering of the energy of the Γ_2 (or 'hexagon') orientation relative to the Γ_1 (or 'pentagon') orientation.

At even modest pressures (12 kbar), the energy difference between hexagon and pentagon orientations is projected to be large enough that the concentration of misoriented molecules (now misoriented refers to the pentagon configuration) is less than 1%. The metastability of the new phase therefore allows a near-completely ordered crystal of C_{60} to be studied at ambient pressure.

1.5 Optical Properties of Crystalline C_{60}

As this thesis consists of light scattering studies of crystalline C_{60}, a description of the optical properties of the material is clearly warranted.

Because of the molecular nature of solid C_{60}, the electronic structure of the solid phase is expected to be closely related to that of the free molecule, and so a molecular approach is often used to describe the solid [95Wb]. The lowest unoccupied molecular orbital (LUMO) of C_{60} is found to have the same odd parity as the highest occupied molecular orbital (HOMO) and so optical transitions at the HOMO-LUMO gap are dipole forbidden [92Nd]. Experimentally, the absorption edge of C_{60} in solution is found to be ~1.9 eV [92Nd], and higher energy sharp features in the absorption spectrum are attributed to transitions between vibronic states (many-electron molecular electronic states coupled to intramolecular vibrations of appropriate symmetry) [92Nd,92Yd,93Sc].

The optical absorption threshold of solid C_{60} is near 1.7 eV (~730 nm) [92Wb], and the optical absorption spectrum contains higher energy features similar to those of C_{60} in solution [95Wb]. Weak photoluminescence bands are seen in solid C_{60} spanning the spectral range of ~730 nm to 1 μm. As was the case with the optical absorption spectra, the photoluminescence features of solid C_{60} are similar to those of C_{60} in solution, apart from a redshift [95Wb].

These optical properties of solid C_{60} impact very seriously on the implementation of a light scattering experiment. Popular excitation sources for Raman spectroscopy are the 488 nm and 514.5 nm lines of an argon-ion gas laser. The argon-ion laser is widely

available, and sensitive detectors exist for the detection of light near these wavelengths. Unfortunately, the 1.7 eV (≈ 730 nm) absorption edge of solid C_{60} implies that a substantial amount of fluorescence will be seen underlying the Raman bands of interest (while the fluorescence yield is quite small, the Raman intensities are weaker yet). As the sample is absorbing the incident photons as well as scattering them, sample heating also becomes a concern at higher power densities. More importantly still, solid C_{60} has been widely documented to undergo a photophysical degradation when exposed to even modest power densities of visible - UV wavelength light [91Db,92Z,93I,94B]. The molecules are believed to polymerize through a cyclo-addition reaction, in which neighbouring molecules are cross-linked by having two double bonds, one from each molecule, form four single bonds [93Z]. The most pronounced impact of this photo-polymerization is to shift the second A_g internal vibration down in energy from ~1468 cm^{-1} to ~1458 cm^{-1}. The intrinsic value of the $A_g(2)$ mode was in fact a much debated quantity; samples which have not been exposed to air prior to measuring their Raman spectrum showed the $A_g(2)$ mode at 1458 cm^{-1}, while those which did receive air-exposure would initially show the $A_g(2)$ mode at 1468 cm^{-1}, but upon irradiation with higher power densities of visible excitation, the mode would down-shift to 1458 cm^{-1}. It was eventually shown that molecular oxygen would readily diffuse into the C_{60} lattice and would act to quench the excited state of the C_{60} molecules, thereby suppressing the photo-polymerization effect [92Z,93Z]. Pristine samples would photo-degrade at quite low power densities (50 $^{mW}/_{mm^2}$), while samples exposed to oxygen could endure higher power densities before degrading.

The success of the experiments described in this thesis stems in a large part from the use of near-infrared excitation wavelengths. The laser excitation used for all the Raman spectroscopy ranged from 780 - 895 nm, which was below the absorption edge of the sample, and so the adverse effects of C_{60} fluorescence and potential photo-degradation were completely avoided. This was particularly crucial for the measurement

of the libron modes. The libron mode intensities were extremely weak (see Chapter 4), requiring higher laser intensities which would have readily photo polymerized the material had above-gap excitation been employed. Also, the weak intensity libron modes would have been completely masked by the sample fluorescence generated at shorter excitation wavelengths. While the detectors employed in this study were less sensitive to these longer wavelength emissions, the Raman signal is increased due to the transparency of the sample. The penetration depth of green excitation is only a few microns in solid C_{60}, while it is several orders of magnitude larger for 895 nm light [92Lc].

CHAPTER 2

EXPERIMENTAL

2.1 Introduction

A spectroscopic study of a 'conventional' semiconductor such as silicon or gallium arsenide almost invariably involves a collaboration between a spectroscopist and a crystal grower. The production of research grade semiconductors requires a growth facility which costs hundreds of thousands of dollars (molecular beam epitaxy, chemical vapour deposition, etc.), and an operator who is adroit in the art of crystal growth. This makes it unlikely that a researcher whose bailiwick is that of solid state spectroscopy will be able to independently supply himself/herself with samples. The exception to this is solid C_{60}. Crystalline material with large*, well defined facets can be readily achieved by sublimation growth of commercially available C_{60} powder. Should there exist a need for specially prepared starting powder, as was the case in this work, the synthesis of the C_{60} molecules can also be performed in-house, with reasonably little expense. The ability to fabricate one's own samples lends a tremendous amount of flexibility to an experiment; the researcher knows both what sample properties (size, morphology, impurity concentration, etc.) are desired for a given experiment, and what range of properties can actually be fabricated (and hopefully the two do not differ too greatly!).

The details of the C_{60} synthesis and crystal growth are covered in sections 2.2 and 2.3, while the latter half of this chapter is devoted to the practical aspects of the Raman scattering experiments described in this work.

---

* large by the requirements of optical characterization techniques; samples weighing only tens of milligrams and with facets measuring ~1 mm in length are of a sufficient size for a Raman scattering study.

2.2 C_{60} Molecular Formation

While a number of techniques have been used for the formation of fullerenes from graphitic starting material [85K,91Hb,92Pc], the simplest to implement is the carbon arc-discharge method, first described by Wolfgang Krätschmer *et al.* [90K]. By striking an arc through two carbon electrodes in a low pressure helium atmosphere, the carbon atoms and clusters which are evaporated from the electrode tips will form into closed cage molecules (C_{60} and higher weight fullerenes) with reasonably high efficiency, and under an encouragingly broad range of growth conditions.

In Figure 2.1, a diagram is shown of the combustion chamber which was used in this study to produce fullerene containing soot. The vessel consists of a 4 inch diameter copper tube, closed at both ends with brass flanges containing o-ring feedthroughs for the brass rods which supported the graphite rods. O-rings between the flanges and the copper tube provided both a vacuum seal for the chamber and electrical insulation between the chamber and the brass rods. The rods were connected to an AC welding power supply, which could deliver up to 200 amps with a 20% duty cycle. Prior to burning the carbon rods, the vessel would be evacuated with a rotary pump and backfilled with helium gas. During combustion, helium gas was continuously flowed into the vessel through inlets near the plasma observation ports; the pressure in the vessel was maintained at 100-200 Torr by throttling the vacuum pump line. A continuous flow of helium gas prevented soot from collecting on the plasma observation ports which were, in turn, essential for keeping the graphite rods collinear and maintaining a spark-gap of ~5 mm.

Synthesis of the fullerenes is accomplished by first positioning the two carbon rods so that they are touching. Resistive heating occurs while the rods are touching, and the rods are not consumed. The electrodes are manually moved apart to ignite the arc, and continuously fed forward as the rods are vapourized to maintain a steady plasma. After the rods had been burnt down to the brass holders (the use of an AC drive current helps to ensure that the two electrodes are consumed at equal rates), the chamber pressure

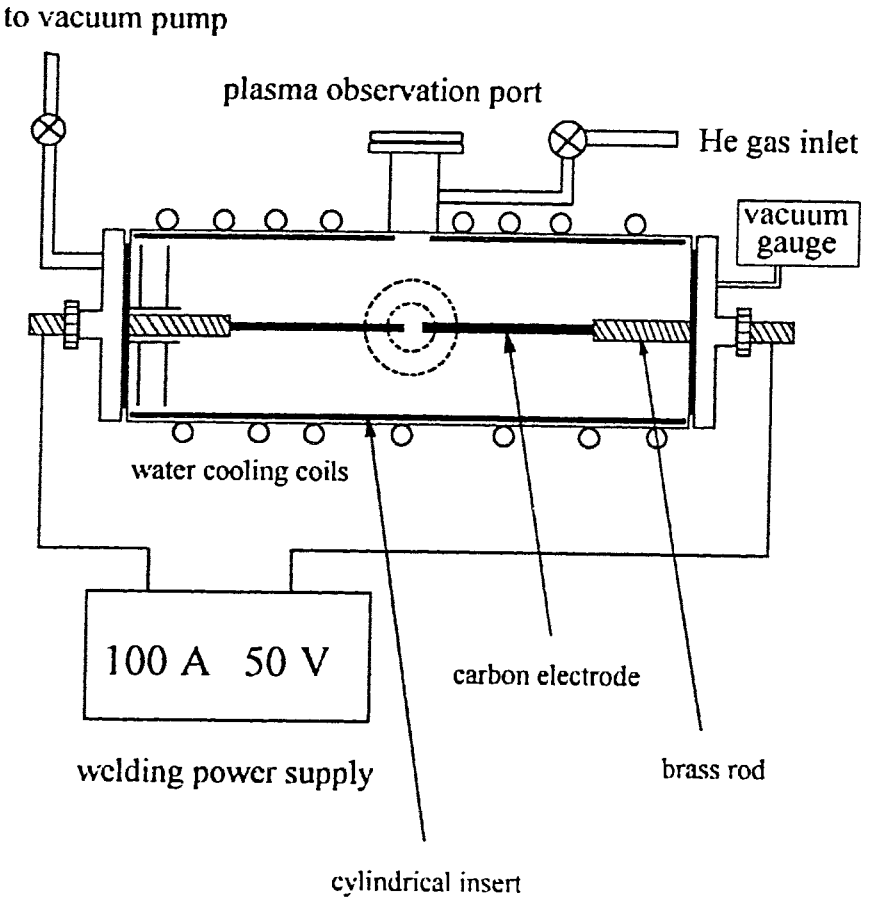

Fig. 2.1 Schematic diagram of the combustion chamber built for the production of fullerenes from the vaporization of carbon rods.

was brought up to atmosphere. The cylindrical copper insert upon which the soot had collected was removed from the vessel and washed with toluene, an effective solvent for the fullerenes.

To separate the fullerenes from the soot produced in the combustion of the carbon rods, a Soxhlet extractor was used, as depicted in Figure 2.2. The washed out contents of the combustion chamber were placed in a cellulose thimble and toluene was refluxed through the extractor. After the first siphoning of the thimble section, a deep reddish-brown colour was visible in the flask of boiling solvent, indicative of the presence of dissolved fullerenes [90K]. After several hours of refluxing solvent through the extractor, the thimble was no longer stained reddish-brown and the removal of the fullerenes from the insoluble graphitic soot was deemed complete.

The toluene solution after Soxhlet extraction is typically 75% C_{60}, 23% C_{70}, and the remainder higher weight fullerenes (C_{76}, C_{84}, etc.) [92Pd]. In order to separate C_{60} from its higher weight cousins, a liquid chromatography column was used. The toluene solution was first evaporated in a dish containing neutral alumina. The dried mixture was then loaded onto a chromatography column which was packed with neutral alumina and eluted with cyclo-hexane. Conventional liquid chromatography affords excellent separation of C_{60}, but has the drawbacks of requiring large amounts of solvent and considerable patience. For a typical column of length ~20 cm, a single run can require approximately twelve hours to complete, during which time an unlucky graduate student must be present to constantly add the 10-12 litres of solvent needed to prevent the column from running dry. One can overcome these drawbacks by using a Kauffman column, which is in essence a liquid chromatography column coupled to a Soxhlet extractor. Such a column is shown in Figure 2.3. The boiling rate of the bottom flask is adjusted so that a head of liquid is always present at the top of the column. As the eluent passes through the neutral alumina, it partially dissolves the fullerenes present in the column. Since the

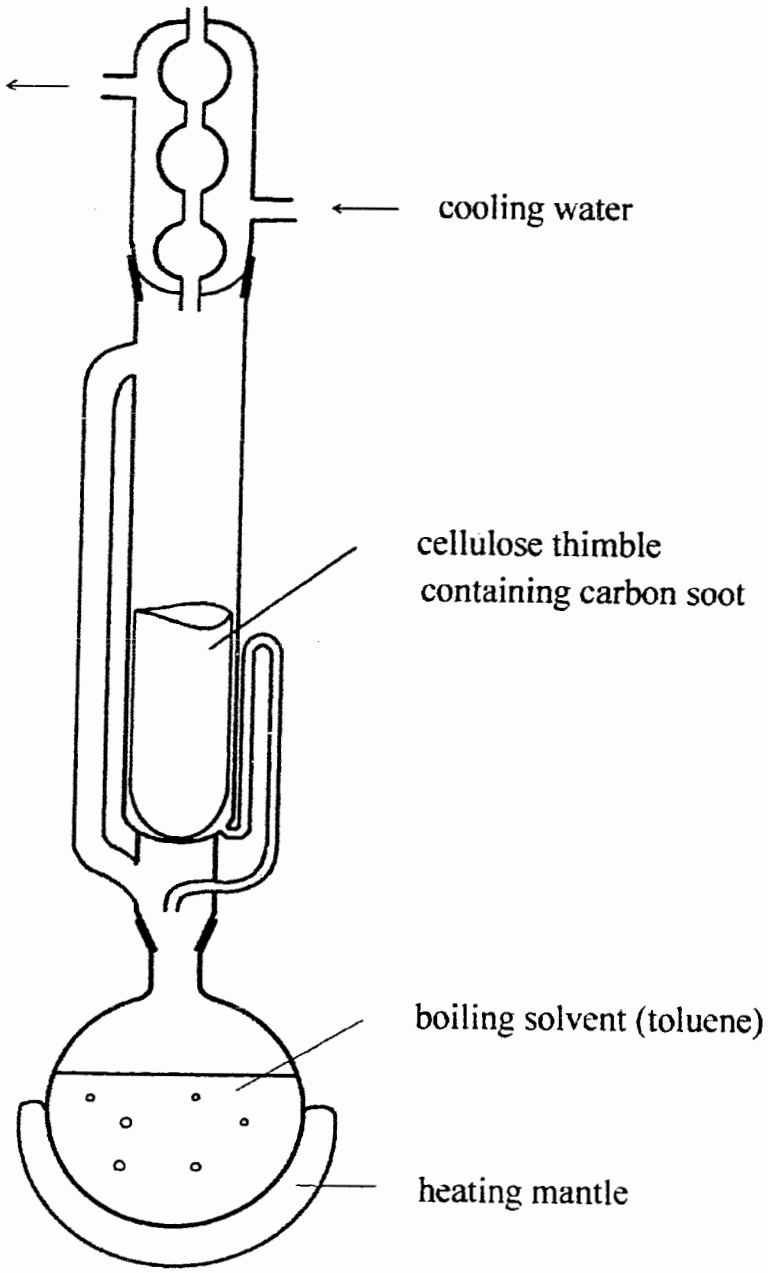

Fig. 2.2 Schematic diagram of the Soxhlet extractor which was used to separate the toluene-soluble fullerenes from the insoluble carbon soot produced during the combustion of carbon rods.

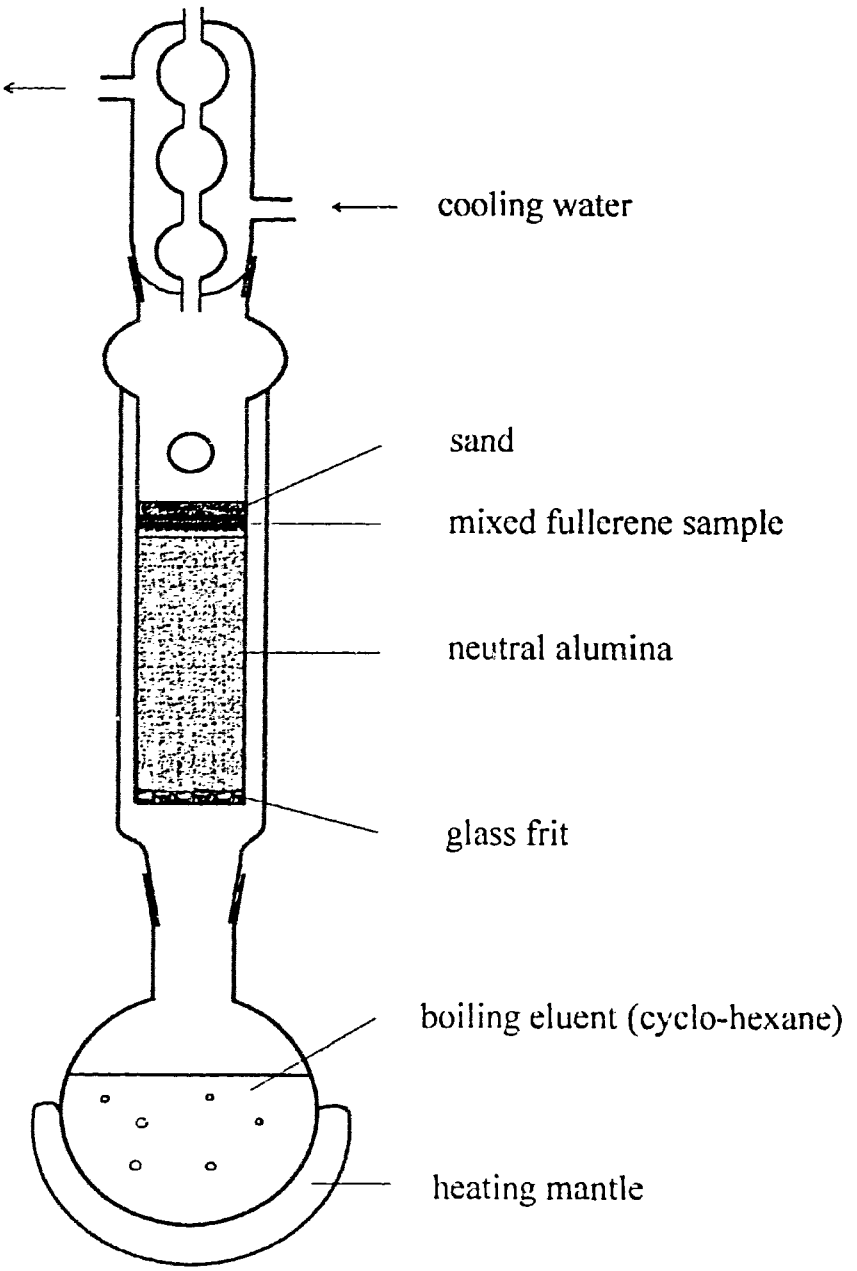

Fig. 2.3 Schematic diagram of the Kauffman chromatography column used to separate C_{60} from its higher-weight cousins (most notably C_{70}). The Kauffman column is simply a conventional liquid chromatography column coupled to a Soxhlet extractor.

different molecular weight fullerenes have different solubilities in the eluent, they will become spatially separated in the column with increasing time. The highest solubility material is C_{60}, and so it will be furthest down the column at any given moment. The separation between it and C_{70} increases with increasing time, until a band of C_{60} is fully visible in the column. C_{60} dissolved in cyclo-hexane displays a brilliant magenta colour, while C_{70} appears red, much like the original solution of mixed fullerenes. After the magenta band had moved through the column and into the boiling flask, it was removed and replaced with another flask of cyclo-hexane to capture the C_{70} band. In this manner, a solution of C_{60} which is at least 99.9% pure (in terms of other fullerenes) is achieved. The solution was then evaporated onto a watchplate, leaving a microcrystalline C_{60} powder.

The average efficiency of the C_{60} formation using the above apparatus was found to be 4.6%, while that of C_{70} was approximately 1%. The initial mass of the carbon rods was typically 5 gm, and so from a single run, approximately 200 mg of C_{60} powder was produced. Efficiencies of twice this have been reported in the literature, a result which is achieved by systematically varying the rather large number of relevant growth parameters. The diameters of the carbon rods, the discharge current, whether AC or DC current flow is used, the geometry of the combustion chamber, the length of the spark gap, and how efficiently the vapourized material is cooled have all been shown to be important parameters in optimizing the production efficiency [92Pd].

While the complete synthesis of C_{60} is reasonably straightforward, commercial sources of high-purity C_{60} powder are presently available, at a cost-per-gram* which is less than that of the in-house produced powder. Thus for the experimental studies of solid C_{60} made from naturally abundant carbon, commercially available powder (Hoechst, Texas Fullerenes) was used for the crystal growth. An important component of

---

* At the time of this writing, 99.9% pure C_{60} powder is available for approximately $200/gm

this thesis, however, required the use of isotopically controlled crystals, for which no commercial sources existed. It was for this reason that the combustion chamber and separation apparatus was built.

A number of researchers have studied isotopically enriched C_{60} crystals, fabricated by simply boring out a graphite rod made from naturally abundant material, and then packing the cavity with enriched carbon powder [93N,95M,95R]. Unfortunately, when such rods are burnt in an arc-discharge, the resulting fullerenes display a bimodal mass distribution, reflecting an incomplete mixing of the natural and enriched regions of the electrode. The gas-phase mixing of the ^{12}C and ^{13}C regions is too slow to compete with the kinetics of carbon condensation, and so fullerenes are formed with both a natural carbon abundance and an enriched ^{13}C concentration. A more obvious drawback of this technique is the fact that neither pure $^{12}C_{60}$ nor pure $^{13}C_{60}$ can be produced.

To fabricate pure $^{12}C_{60}$ and $^{13}C_{60}$ as well as unimodal distributions of intermediate ^{13}C concentrations, while retaining the simplicity of the arc-discharge technique (the only technique which affords the production of macroscopic quantities of fullerenes), we have used carbon rods made from the pyrolysis of isotopically controlled methane gas. When a tantalum filament is heated to 2000-2100°C in a methane atmosphere, the carbon from the methane gas will deposit onto the filament, producing a solid rod which has a spatially homogeneous isotope composition given by the isotope content of the methane gas. After growing a rod to the desired dimensions, the tantalum filament is removed, leaving a hollow carbon rod, formed free of any carbonaceous binders (which would introduce a source of naturally abundant carbon). The ^{13}C concentrations used in this study, and the resulting mass distributions of the C_{60} molecules are discussed in detail in Chapters 3 and 4. The pyrolytic fabrication of carbon rods was performed by Dr. Tom Anthony.

2.3 C_{60} Crystal Growth

Crystalline C_{60} was grown from powder via a straightforward vapour transport method [92V]. The starting powder was placed in the closed end of a 90 cm long and 2 cm diameter quartz tube which was then evacuated to ~10^{-5} Torr. The powder, and approximately 50 cm of the quartz tube was placed in a three zone furnace and heated to 200°C for 24 hours to purify the powder of any residual solvents and absorbed atmospheric gases. After vacuum drying the powder, the evacuated quartz tube was sealed, producing a completely closed tube approximately 40 cm in length, a length which was sufficient to span the three zones of the furnace. A temperature gradient was established in the furnace such that the starting powder was kept at ~550°C while the far end of the growth tube was 50°C cooler. The C_{60} powder would readily sublime at these temperatures, and in the coolest zone the supersaturated vapour would condense into either single crystals or a polycrystalline film.

When the starting material for the crystal growth was C_{60} powder, nearly a third of the initial mass would not sublime at temperatures up to 600°C. Using Raman spectroscopy, this left-over powder was seen to still contain C_{60}, although it was no longer soluble in toluene. However, by using C_{60} which had been sublimed once as the source material for another growth run, virtually 100% conversion efficiency could be achieved. Also, the temperature gradient under which this material would sublime and condense into well-formed crystals was much more reproducible than that of the never-sublimed powder. Therefore a second growth was always used to fabricate C_{60} crystals for study.

The procedure for growing crystals from previously sublimed C_{60} involved first heating the quartz tube which contained the source material to 200°C while the tube was kept under vacuum. After several hours of allowing the material to outgas, the tube was sealed. The central zone of the three zone furnace was then heated to 550-600°C for one hour in order to evaporate any C_{60} particles which might be present. A double

temperature gradient was then established by raising the end zones of the furnace to T while the central zone was lowered to T-ΔT. There was a broad range of values of T and ΔT for which well-developed, highly faceted crystals of C_{60} could be grown. Generally, for T < 400°C the vapour pressure of C_{60} is too small to support vapour transport growth, while for

T > 550°C the vapour pressure is too large to allow a controlled growth. Similarly, if ΔT is too large, the condensation of the vapour in the coolest zone will occur too quickly, and a polycrystalline film or many small crystallites will result. The range of values of ΔT which constitutes "too large" is of course dependent on the value of T; the higher the source temperature and concomitant vapour pressure of C_{60} in the growth tube, the smaller the tolerance on ΔT. Using a value of T~500°C and ΔT~20°C, crystals with several shiny, smooth crystal faces could be produced, examples of which are shown in Figure 2.4.

2.4 Raman Spectroscopy Tools

The principle ingredients in a Raman scattering experiment are an excitation source, a sample holder which controls the sample geometry, temperature, and/or pressure, a spectrometer which analyzes the frequency content of the light emitted from the sample, and a detector which, as the name implies, detects the light selected by the spectrometer. The exact implementation of each of these components is tailored whenever possible to suit the sample under study. The vibrational studies of crystalline C_{60} presented in this work involved high-resolution spectroscopy over a very broad spectral range as well as spectroscopy of extremely weak features at small Raman shifts from a near-infrared laser source. Since no single Raman scattering setup was suitable for such a study, several different implementations were used, as discussed in detail in the following sections.

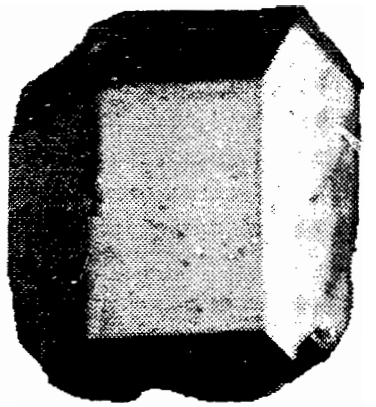

1 mm

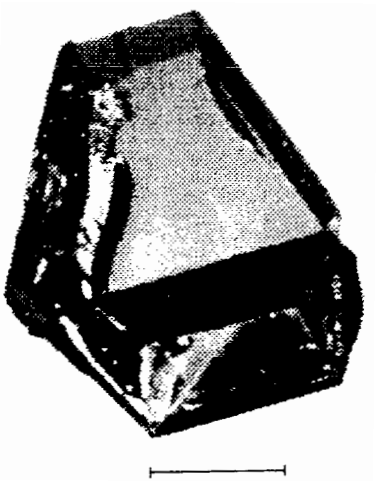

2 mm

Fig. 2.4 Two typical crystals formed during the vapour transport growth of solid C_{60}.

2.4.1 Excitation Source

For all of the light scattering experiments presented in this thesis, the excitation source was a Spectra-Physics Model 3900 Ti:sapphire laser pumped by a 20 W Coherent Innova 400 Ar^+ laser. The Ti:sapphire laser is a solid state laser whose continuous wave output can be tuned over the range from 700 nm to ~1.07 μm. The gain media of the laser are Ti^{3+} ions dispersed in a sapphire matrix (Al_2O_3). The Ti^{3+} ions have broad absorption bands in the UV-visible wavelength range (400-600 nm) and broad fluorescence bands in the visible-near IR wavelength range (700-1100 nm). The fluorescence energy which is allowed to lase is determined by means of an intracavity birefringent tuner. The birefringent tuner is a quartz three-plate filter which causes the otherwise linearly polarized light to become elliptically polarized, dependent upon both the wavelength and the angle of the optical axis of the plate to the electric field of the laser light. Only a narrow range of wavelengths will experience a multiple of 2π phase shift within all three plates and return to linear polarization. Wavelengths which remain elliptically polarized suffer additional losses at all the Brewster angled surfaces within the laser cavity and are thus prevented from lasing. The laser is tuned to different wavelengths by simply rotating the birefringent filter with respect to the electric field of the laser light. For the high-resolution Raman studies presented in this thesis, the laser was further frequency stabilized and linewidth narrowed by means of a 0.5 mm thick intracavity etalon.

Continuous measurement of the laser wavelength was made using a Burleigh Wavemeter which consisted of a scanning Michelson interferometer with a prealigned, internal HeNe laser as a reference source. For the Fourier-transform Raman scattering experiments, the output intensity of the Ti:sapphire laser was stabilized by means of an acousto-optic power stabilization device (Liconix Inc.). The beam is passed through a glass medium in which a refractive index grating is established by a piezoelectric transducer driven by radio-frequency (RF) power. A fraction of the beam is Bragg

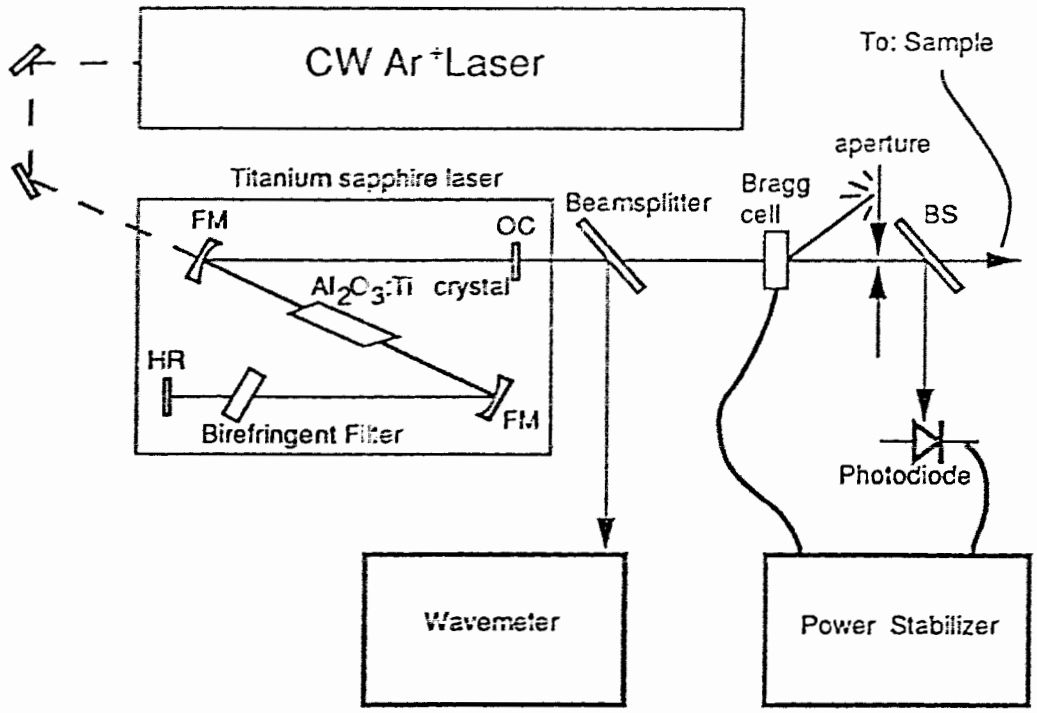

Fig. 2.5 Diagram of the excitation source used in this work. Shown schematically is the laser cavity defined by the high-reflector (HR), fold mirrors (FM), and output coupler (OC). Before reaching the sample, the beam is sampled by the wavemeter, and passes through the power stabilization unit (see text for descriptions).

reflected and subsequently blocked by an aperture. The intensity of the remaining beam is sampled and a servo-loop adjusts the RF power to maintain a constant light output. The Ti:sapphire laser, complete with wavelength meter and power stabilizer is shown schematically in Figure 2.5.

2.4.2 Spectrometers and Detectors

Two different spectrometers were employed in this Raman scattering study, a Bomem DA8.01 Fourier-transform (FT) interferometer, and a McPherson 1.0 m single-pass dispersive spectrometer. These two instruments are quite distinct and each has particular advantages over the other.

The Bomem interferometer, shown schematically in Figure 2.6, is based on the well-known Michelson interferometer. The scattered light emitted from the sample is collimated and directed towards a quartz beamsplitter by an f/4 off-axis paraboloid mirror. The beamsplitter divides the incident light into transmitted and reflected parts, each of which is returned to the beamsplitter by a flat mirror. One mirror is fixed while the other scans along a path collinear with the transmitted light, thereby introducing a time-varying path difference. The resulting interference signal (interferogram) is focused onto a detector whose output is then digitized and stored as a function of path difference. A Fourier-transform of the interferogram extracts the entire spectral content of the light incident onto the interferometer. A more detailed description of the operation of the Bomem interferometer can be found in several recent theses, such as Nissen [92N] and Lenchyshyn [93L]. The detector used with the interferometer was an RCA C30872 silicon avalanche photodiode detector.

The single-pass grating spectrometer, shown in Figure 2.7, is quite different from the Fourier-transform instrument in that only a small fraction of the frequency spectrum is simultaneously sent to the detector. The heart of the dispersive spectrometer is the grating. The grating consists of a series of closely spaced parallel grooves, each of which

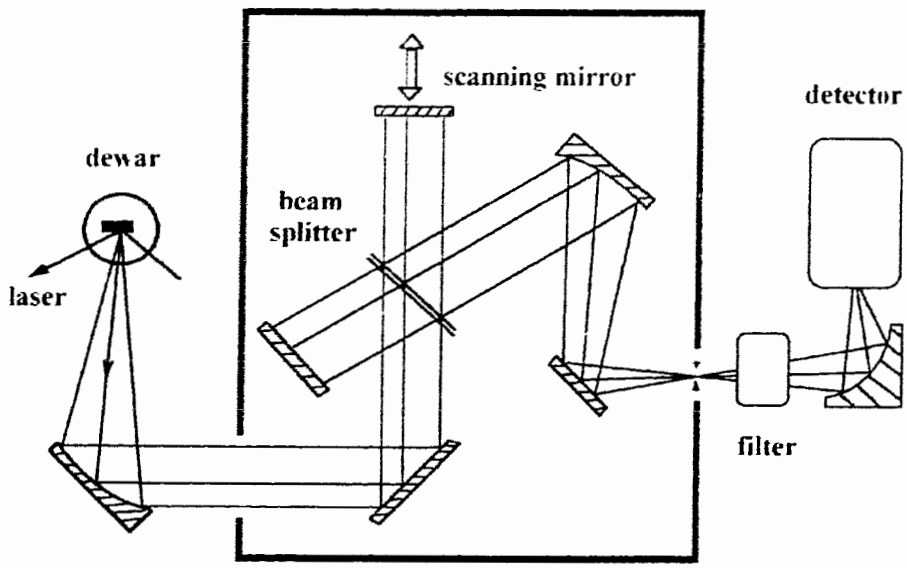

Fig. 2.6 Schematic diagram of the Bomem Fourier-transform spectrometer.

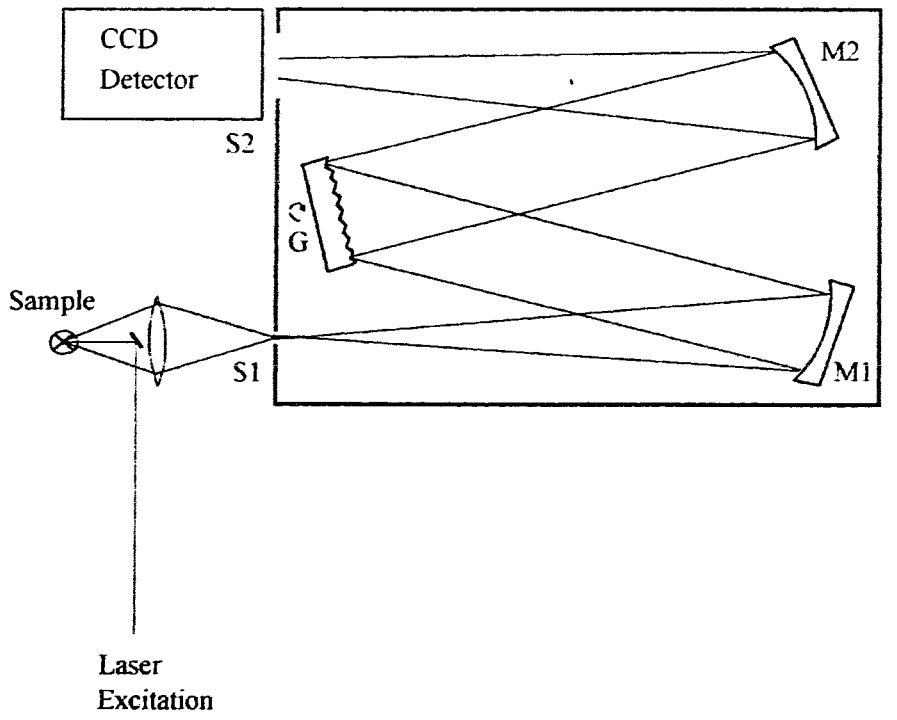

Fig. 2.7 Diagram of a single-stage grating spectrometer and imaging detector.

acts as a radiation source, diffracting the incoming light at various angles. For a given wavelength λ, there is a reflected angle r such that the path difference between light reflecting off successive grooves of the grating is an integral number of wavelengths, producing a maximum in the reflected light intensity (constructive interference). More precisely, the condition for constructive interference is given by

$$m\lambda = d\{\sin(i) + \sin(r)\}, \qquad 2.1$$

where m is the order of the maximum (the number of integral wavelengths in the path difference), d is the groove spacing, and i and r are the angles of incidence and reflection measured from the grating normal. Thus, the grating spectrometer analyzes the spectral content of the light incident onto the entrance slit by spatially separating the different frequency components. Traditionally, a second slit would appear over the exit port, thereby transmitting a small frequency interval to the detector. By simply rotating the grating, successive frequency intervals could be passed to the detector, and the full spectrum would be scanned in this fashion. The advent of charge-coupled device (CCD) array detectors has led to a significant improvement in the field of dispersive spectroscopy. A CCD detector is typically comprised of thousands of active elements, each of which is a photo-detector, and so rather than scanning the spectrum one frequency interval at a time, over a thousand such frequency intervals could be measured simultaneously. This obviously represents a tremendous reduction in the time required to collect the complete spectrum as compared to a single element detector such as a photomultiplier tube. In this study, a Photometrics silicon CCD detector with an active area of 1024 x 256 pixels was used. A more complete description of dispersive spectroscopy can be found in any one of a large number of reference texts (see for example W. Demtröder [81D]).

The advantages of the Bomem interferometer which were relied upon in this work are essentially two-fold: its superior energy resolution and its ability to collect the entire frequency spectrum of interest simultaneously. The spectral resolution of the

interferometer is determined by the maximum distance the moving mirror can scan from zero path difference; for the Bomem DA8.01, the maximum resolution is 0.02 cm^{-1}. The resolution of the grating spectrometer is determined by the entrance slit width, the width of the grating, the detector pixel width, and the grating diffraction angle. In this study, both a 1200 groove/mm grating operating in first order and a 600 groove/mm grating operating in third order were used, which, with a 50μm entrance slit width, gave an instrumental resolution of 0.5 cm^{-1} and 0.3 cm^{-1} respectively at 895 nm. As will be shown in later chapters, many of the vibrational modes of crystalline C_{60} have extremely narrow linewidths (~0.1 cm^{-1}) and fine-structure components which have very small energy separations. The greater resolution of the interferometer was essential to fully resolve these narrow components, the study of which makes up the bulk of this thesis. In addition to containing sharp fine-structure, the phonon spectrum of crystalline C_{60} spans a huge energy range; the lowest energy intermolecular phonon appears at 19 cm^{-1} while the first-order intramolecular phonons extend up to ~1600 cm^{-1}. Since the full frequency spectrum is collected and analyzed simultaneously by the interferometer, such a large spectral range does not pose any additional experimental hardship. When using the grating spectrometer, however, multiple spectral windows (grating positions) are required to measure the full phonon spectrum at modest resolutions, making it less convenient to use than the interferometer.

Despite its lower resolution, the grating spectrometer was used extensively in this work, due solely to the greater sensitivity of the CCD detector as compared to the photodiode detector used with the interferometer. The CCD detector has an extremely small dark current per pixel, and so is inherently superior to a photodiode which requires a large number of incident photons to generate a photocurrent above the noise level. As discussed earlier, the CCD detector is also an array of 1024 x 256 detectors, implying that 1024 energy intervals can be captured by the CCD detector for a given, fixed orientation of the grating.

2.4.3 Filters

Every spectroscopist who has ever performed a Raman scattering study, regardless of their particular experimental apparatus, appreciates the need to reject elastically scattered laser light. Scattering at the laser frequency is normally many orders of magnitude more intense than the strongest Raman signal. In dispersive spectroscopy, the conventional approach to reducing the amount of laser light reaching the detector while still passing low energy Raman signals is to use multiple stages of dispersion (e.g., double or triple spectrometers), at the cost of greatly reducing the overall throughput. This is not an option in FT-spectroscopy, where all the frequencies entering the interferometer are sent on to the detector. A notch or edge filter must be placed before the detector to attenuate any collected laser light while passing all frequencies of interest. Unfortunately, even high-quality holographic rejection filters require at least ~100 wavenumbers to pass from high rejection (optical density ≥ 4) to high transmission.

An alternative method of laser light rejection, used for many years in dispersive spectroscopy [30R, 71D, 92I, 92Pc] is based on the absorption of an atomic or molecular vapour. Alkali-metal vapours in particular have strong discrete optical transitions spanning the region from the UV to the near-IR. Operating at modest partial pressures and temperatures, the vapour represents a near-perfect filter which is completely transparent except at its electronic transitions, where optical densities exceeding 10 per centimeter of gas can be achieved with a Doppler-broadened linewidth of less than 1 cm^{-1}. In practice, the filter consists of an evacuated glass cell in which an excess of metal is placed. The vapour pressure in the cell is then controlled by varying the temperature. By placing the cell before the entrance slit of a spectrometer and tuning the excitation source onto the absorption band of the vapour, one achieves a compact and efficient filter for low-wavenumber Raman measurements. A major drawback of alkali-metal vapour cells, however, is the re-radiation of absorbed light in the form of fluorescence. The strong fluorescence of the alkali-metal vapours, centered at the laser

frequency, can complicate the use of the cell as a filter for low-energy Raman measurements by masking the signal of interest. The vapour cell fluorescence can be to a great extent collisionally quenched by introducing into the cell a buffer gas such as nitrogen, but at the cost of pressure broadening the absorption band of the atomic transition.

For the measurements of the intermolecular, or lattice modes of solid C_{60} (see Chapter 3), alkali-metal vapour filters were developed for use with both the grating spectrometer and the Bomem interferometer. The vapour filters consisted of cylindrical quartz cells in which a small nugget (~1 mg) of either rubidium or cesium metal was placed. The cells were evacuated and then sealed. A select number of cells were backfilled with 50 Torr of nitrogen gas to quench the alkali-metal fluorescence. The quartz cells were encased in segmented brass blocks which were heated in such a way that the flat window faces of the quartz cylinders were kept warmer than the center of the quartz cells, while still allowing optical access through the window faces. This prevented the metal vapour from condensing onto the windows, which would reduce the throughput of the cell. Rubidium metal vapour possesses optical transitions from the ground state to the first excited multiplet at 794.76 and 780.03 nm. The next ground-state optical absorption occurs at 421.7 nm, so a large window of transparency is available. Similarly, atomic cesium possesses two strong ground-state absorptions at 852.11 and 894.35 nm whose oscillator strengths are similar to those of rubidium. All of these energies are easily accessible with the Ti:sapphire laser, making these metals ideal choices for use as a Raman filter.

Since the partial pressure of the vapour phase is strongly dependent upon the temperature of the metal, the density of the vapour, and thus the absorbance of the filter, can be varied by varying the temperature of the cell. By 210°C, both the rubidium and cesium vapours are sufficiently dense to completely block 100 mW of collimated laser light sent *directly* into the cell. In addition to increasing the absorbance, raising the

temperature of the cell also broadens the width of the absorption peak, particularly if a buffer gas is used.

By heating a vapour cell to 210°C and placing it before the entrance slit of the grating spectrometer, Raman shifts as low as ± 10 cm^{-1} were measured from crystalline C_{60}, using only a single stage of dispersion. The limit on how low a shift could be measured was determined by the width of the absorption peak, rather than stray laser light passing through the cell. The rather large width of the vapour absorption peak stemmed from pressure-broadening of the 50 Torr of nitrogen gas in the cell. The nitrogen gas was necessary to quench the fluorescence of the alkali-metal vapour which was otherwise much more intense than Raman scattering from the lattice modes of C_{60}. By placing the same cell (T=210°C, 50 Torr nitrogen gas) before the entrance port of the interferometer, a similar result was achieved.

A simple, yet significantly improved, solution to the problem of cell fluorescence lies in the positioning of the cell. In the case of the interferometer, light entering the machine is modulated by the beamsplitter and moving mirror combination and then sent on to the detector. By placing the vapour cell between the interferometer and detector, rather than between the sample and the interferometer, one still prevents any collected laser light from directly reaching the detector. However, since the short lifetime fluorescence follows the modulation given to the laser wavelength, the fluorescence of the filter is modulated at a frequency which corresponds exactly to the modulation given the laser wavelength. When the Fourier transform of the detector signal is performed, the spectrally broad fluorescence is compressed into a peak centered at the laser frequency and with a width corresponding to the instrumental resolution. Thus the fluorescence of the filter can be suppressed without using a buffer gas, which provides a substantially narrower absorption peak width at the temperatures needed to suppress the stray laser light signal [94H]. Placing the vapour cell between the interferometer and detector

requires no modification whatsoever of the existing experimental set-up since a space between the two devices already exists for conventional filter placement.

In addition to the vapour filters discussed above, coloured glass filters were also used for the experiments presented in this work. A red filter (passing wavelengths longer than ~750 nm) was used at the entrance slit of the grating spectrometer and in the filter box of the interferometer. The red filter was used with the grating spectrometer to prevent stray, higher energy light from appearing in second or higher order, while the red filter was needed with the interferometer to block emission from the internal HeNe laser (which is used for measurement of the scanning mirror position) from reaching the detector.

4.2.4 Low Temperature, High Pressure Sample Mounts

The experiments presented in this work were carried out at both cryogenic temperatures and large hydrostatic pressures. Temperature control was achieved by mounting the samples in a Janis Varitemp dewar, in which the sample temperature could be varied from 1.6 K (superfluid helium) to room temperature. Liquid helium was contained in a reservoir surrounding the sample chamber into which cold gas or liquid was flowed by means of a throttling valve connecting the two chambers. The sample temperature was monitored by means of a Si-diode temperature sensor located on the sample mounting block. For the experiments conducted at ambient pressure, the samples were mounted in a stress-free manner by milling out a sample compartment in a copper block and enclosing the sample with a glass cover-plate. For the polarization measurements of the phonon modes (described in detail in Chapters 3 & 4) in which an oriented sample was needed, the platelet-shaped crystals of C_{60} were sandwiched between two glass cover-plates. Again, this was done in a stress-free manner by placing between the glass cover-plates a cardboard gasket which was slightly thicker than the sample.

The hydrostatic pressure studies of crystalline C_{60} were carried out in a sapphire-anvil cell, the central elements of which are shown schematically in Figure 2.8. The two sapphires are held diametrically opposed with a copper gasket placed between them. A hole is drilled in the gasket to form the sample space, which is filled with the sample, a hydrostatic pressure medium, and a small amount of ruby dust which is used for calibrating the pressure. Pressure is applied by an arrangement of six screws which pull the two halves of the cell together when tightened. The sapphire culets measured 3 mm in diameter while the preindented copper gasket was typically 0.5 mm in thickness with a hole diameter of 2 mm. This combination of sapphires and copper gasket allowed hydrostatic pressures of ~20 kbar to be reached, which was sufficient for studying the orientational metastability of solid C_{60} (see Chapter 5). Typical sample dimensions used with the sapphire-anvil cell were 1 mm x 1 mm x 0.2 mm.

For the pressure and temperature ranges used in this work, a large number of pressure media were potentially available. The most hydrostatic medium to use is liquid He, but it has been previously shown that the small He atoms will readily intercalate into the C_{60} lattice under pressure [93Sb]. For this reason, liquid N_2 was chosen for the bulk of the hydrostatic pressure studies shown in this work. The main results of this work were repeated using a 4:1 methanol:ethanol mixture as the pressure medium; no difference between it and the experiments done using liquid N_2 were seen, discounting the possibility that the results reported here stem from nitrogen intercalation into the C_{60} lattice.

The loading of the sapphire-anvil cell and subsequent spectroscopic measurements were done in the same Varitemp dewar used for the experiments conducted at ambient pressures and cryogenic temperatures. A typical set-up of the hydrostatic pressure experiments is shown in Figure 2.9. The open cell was loaded into the dewar which was then evacuated and backfilled with liquid nitrogen. The cell was sealed while immersed in the liquid, after the sample chamber was pressurized with

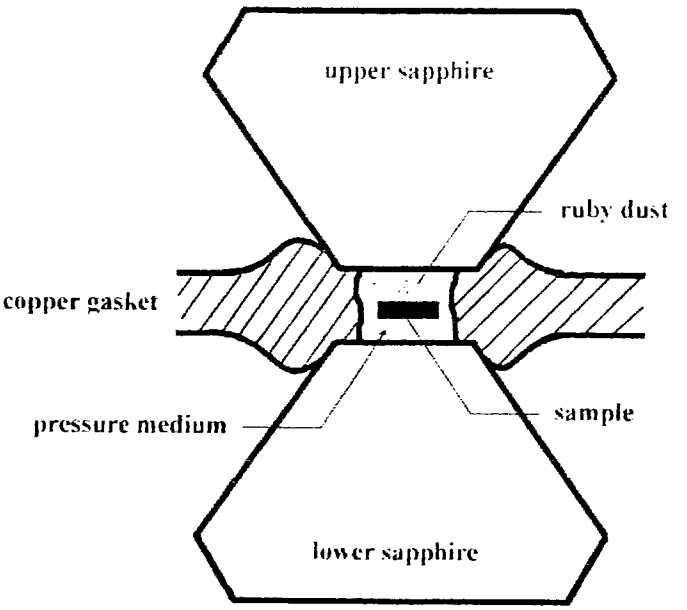

Fig. 2.8 Schematic cross-section of a sapphire-anvil cell illustrating the manner in which a sample is contained by a metal gasket while being squeezed between the culet faces of two sapphires. Ruby dust is used to measure the pressure.

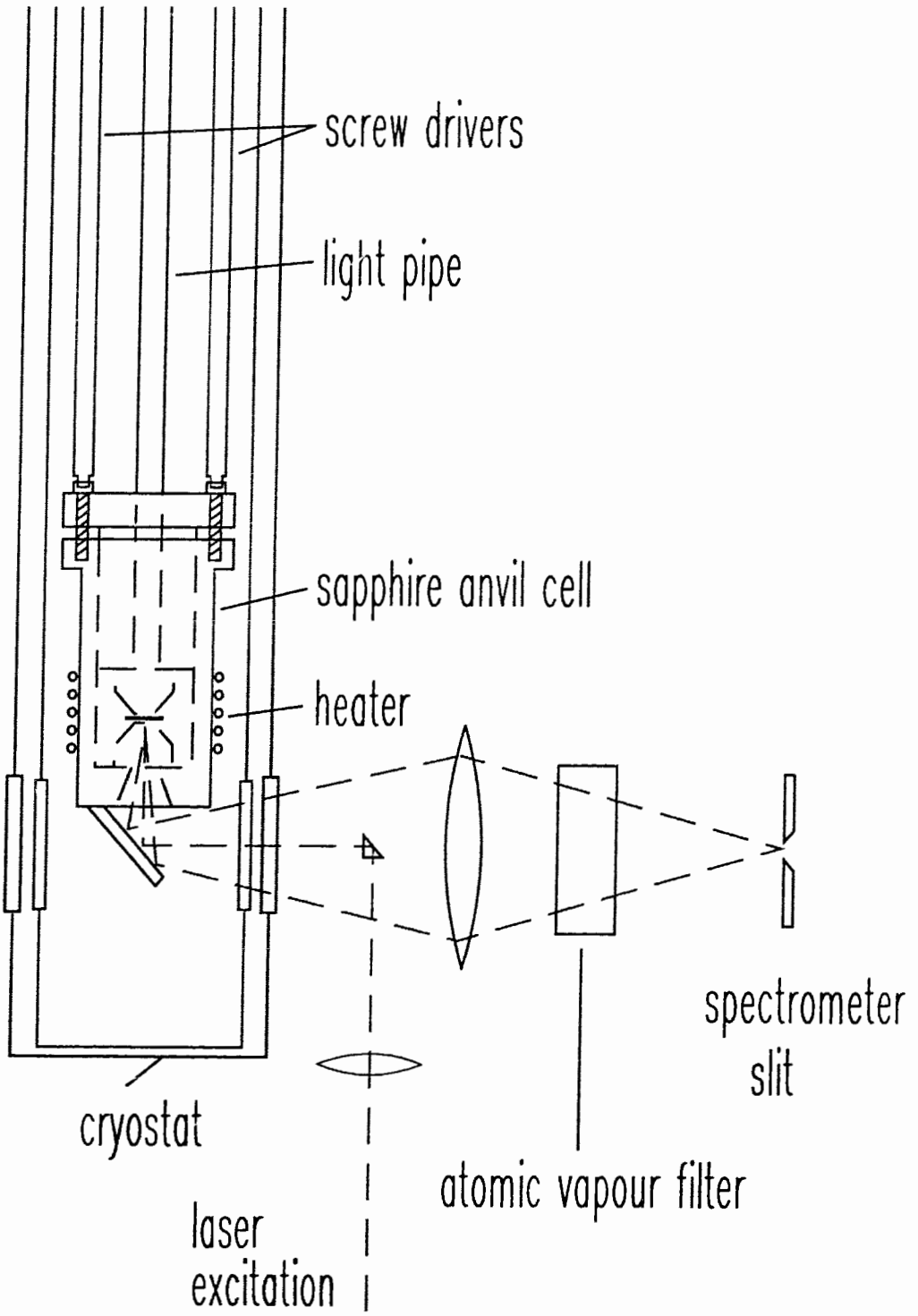

Fig. 2.9 Diagram of the hydrostatic pressure rig inside a varitemp dewar. The sample is excited in a backscattering geometry, through the bottom face and culet of the lower sapphire. Ruby fluorescence is generated by shining a light-bulb down the light-pipe and into the cell through the upper sapphire.

nitrogen gas to briefly stop the quiescent boiling of the liquid. This was essential to prevent a gas bubble from becoming trapped within the gasket hole. The sample was excited in a backscattering geometry through the transparent back-face and culet of the bottom sapphire.

The hydrostatic pressure was measured using the ruby fluorescence scale developed by Forman [72F] which is based on the pressure dependence of the wavelengths of the R_1 and R_2 fluorescence lines of the Cr^{3+} ion in ruby. These lines may be excited with blue or green light, typically a HeCd or Ar^+ laser, but owing to the sensitivity of the CCD detector (all of the pressure experiments were done using the grating spectrometer), a simple light-bulb shining down the light pipe and entering the cell through the top sapphire was sufficient to excite a measurable amount of ruby fluorescence. A blue filter was placed between the light-bulb and the light pipe to block longer wavelength emissions which would have masked the ruby fluorescence signal. The R_1 and R_2 fluorescence lines occur at 694 and 696 nm, respectively (at ambient pressure), and shift in a nearly linear fashion with small hydrostatic pressures, at the rate of 0.36 Å/kbar. The lines also shift with temperature at constant pressure, which was accounted for in determining the actual pressure [72F].

CHAPTER THREE

RAMAN SCATTERING FROM INTERMOLECULAR PHONONS

3.1 Introduction

Lattice phonons in solid C_{60} were first observed in 1992 using the technique of inelastic neutron scattering (INS) [92Pb,92N]. These measurements suggested that the model intermolecular potentials which had successfully reproduced the $Pa\bar{3}$ ground state of the ordered crystal were too soft by at least a factor of two. Detailed comparisons between theory and experiment were not possible, however, due to the low energy resolution of the measurements.

In contrast to INS, Raman spectroscopy should be an ideally suited technique for the measurement of the libron modes. While the scattering events are limited to the zone center of the libron bands, at least an order of magnitude improvement in energy resolution is possible over that of INS, and vastly smaller samples can be tolerated for adequate signal-to-noise. Several reports of Raman scattering from libron modes in crystalline C_{60} have appeared in the literature [92Lb, 92Lc, 93M], but all of the measurements were subsequently shown to be of extrinsic features, not related to scattering from lattice phonons [93H]. Moreover, while the libron modes of solid C_{60} are in principle Raman-active, it was theoretically predicted that Raman scattering from the lattice modes was not likely to *ever* be observed [92Yc, 94Y]. While Raman scattering from libron modes is allowed from a symmetry point of view, the intensity of Raman scattering from C_{60} librons was predicted to be virtually zero due to an isotropic molecular polarizability in the independent molecule approximation.

In this Chapter, the first optical measurements of C_{60} libron modes are presented [93H]. The low energy bands seen in Raman scattering are shown to vanish

abruptly at the 260 K order-disorder transition, consistent with their identification as lattice modes, and the assignment of the observed features to C_{60} lattice modes is made unequivocal by studying their dependence upon the carbon isotope content of the crystal. The linewidths of the libron modes seen in Raman scattering from high-quality single crystals are extremely narrow, leading to the discovery of rich fine-structure in the lattice mode spectrum. More features are seen in the Raman spectrum than expected from a group-theoretical analysis of the low-temperature phase of solid C_{60}. Group theory requires degeneracies of the twelve libron modes such that at most five modes are non-degenerate [92Yc, 92Dc]. In the Raman spectra shown in this Chapter, however, at least eight modes are resolved. These additional modes do not stem from the isotopic disorder present in crystals made from naturally abundant carbon; the Raman spectra of natural and $^{12}C_{60}$ crystals are shown to be identical [95H]. Conversely, the merohedral disorder of the low-temperature phase is shown to influence the energies and intensities of many of the Raman bands [95H]. The merohedral disorder is proposed, therefore, to be the symmetry-breaking mechanism which accounts for the excess libron fine-structure.

Several researchers have raised the possibility that the modes shown in this work are activated by impurities present in our samples [94Y, 94Bb], in keeping with the theoretical prediction that the intrinsic Raman intensity of the libron modes is virtually zero. Oxygen is known to readily diffuse into C_{60} crystals exposed to air, allowing the possibility that the libron mode intensities stem from the random perturbations of intercalated gases. To address this concern, crystals were grown in vacuum and studied without exposing them to atmosphere. The intensities of the libron bands of these air-free crystals will be shown to be identical to the intensities of the libron bands seen in the large collection of air-exposed crystals, grown under a wide variety of conditions, which we have studied. The libron bands we observe also display well-defined polarization dependences [95Hb], arguing against a random-impurity activation of the libron mode

intensities. These results strongly support the assertion that the Raman intensities reported in this work are intrinsic to the crystal.

3.2 The Libron Spectrum of Crystalline C_{60}

A typical low-temperature Raman spectrum of crystalline C_{60} is shown in the bottom curve of Figure 3.1. The spectra shown in Fig. 3.1 were collected using the Bomem interferometer, with a cesium vapour cell (λ_{laser} = 894.60 nm) placed between the interferometer and detector. The sharp peak centered at zero shift is therefore predominantly fluorescence from the atomic vapour filter, modulated at the laser modulation period, as opposed to break-through of the laser light itself. The data presented have not been corrected for the absorption of the atomic vapour filter, which accounts for the central dips in the high-temperature spectra of Fig. 3.1. Clearly visible in Stokes scattering at 10 K are two features centered at 18.5 and 21.8 cm^{-1}. These features are assigned to librational modes of the C_{60} crystal based upon their temperature evolution as shown in Fig. 3.1. The spectra are all on the same intensity scale, simply shifted for clarity, while the region ± 3 cm^{-1} of the laser line has been omitted for all but the 10 K spectrum. As the temperature is raised, the anti-Stokes scattering grows in intensity as one expects, as does the Stokes scattering due to the thermal population factor, allowing additional weaker modes to be observed.

If these features are libron modes, they must vanish at ~260 K, the temperature of the order-disorder phase transition. As can be seen from Fig. 3.1, between 257 K and 259 K, the features do indeed vanish, replaced by a strong Lorentzian background centered at the laser frequency. The presence of a Lorentzian background is expected, due to quasi-elastic light scattering from the freely rotating molecules [75H]. There appears to be a few degrees of laser heating of the sample, since Raman studies of the intramolecular modes on these same samples using much lower laser power (discussed in

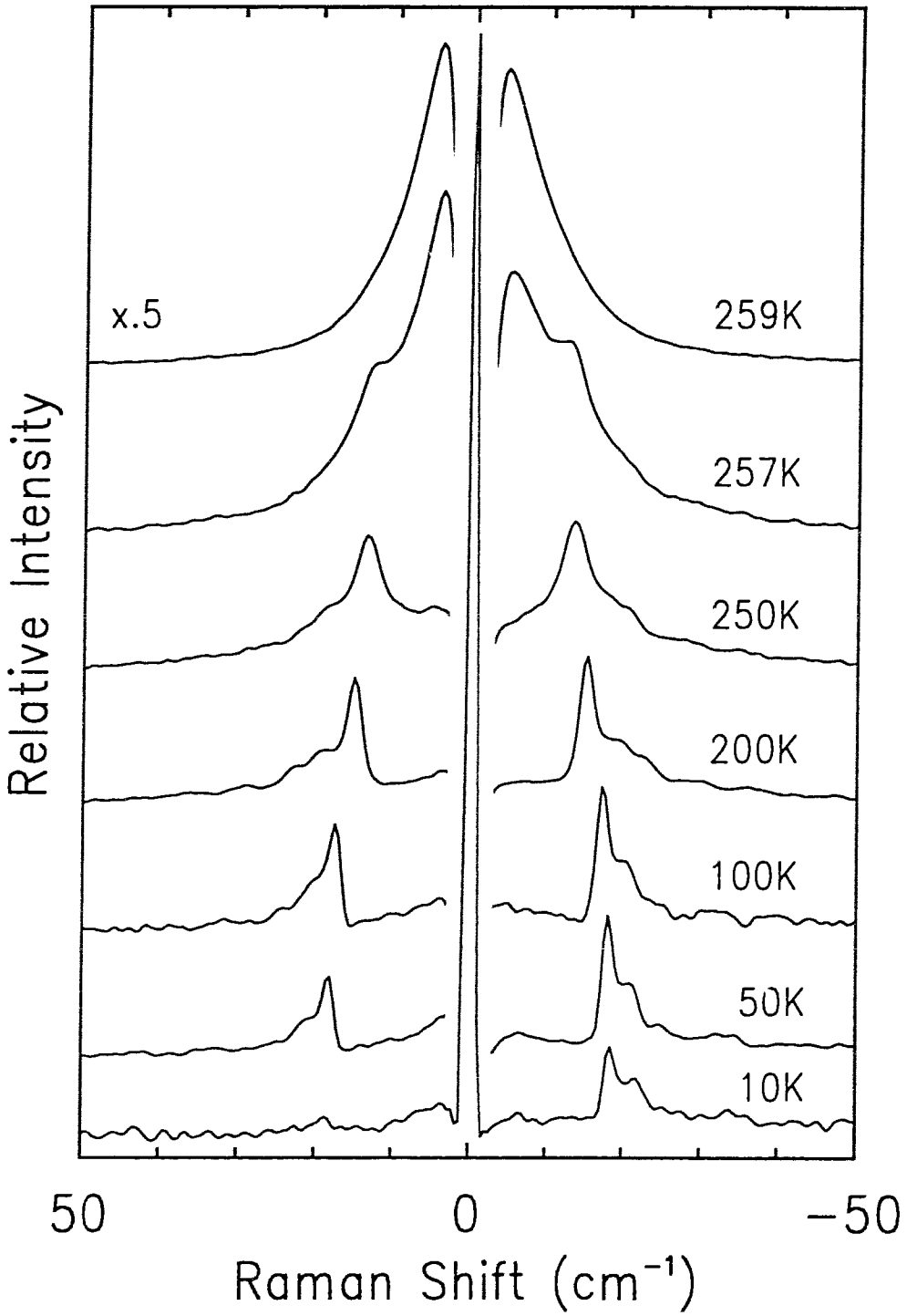

Fig. 3.1 Temperature evolution of the C_{60} librational modes. The spectra have not been corrected for the absorption of the laser rejection filter. All the spectra except the 259 K data are on the same scale, merely shifted for clarity. The region ± 3 cm^{-1} of the laser line has been omitted for all but the 10 K spectrum.

Chapter 4) have verified a sharp phase transition at 260.3 K (T increasing) and 259.4 K (T decreasing).

The energy of the strongest libron peaks softens by ~30% while the full-width at half-maximum (FWHM) of the observed band more than triples from 10 K to 250 K, as shown in Figure 3.2. The integrated intensity of the Stokes libron band is also shown, as is the intensity of the Lorentzian background. Fig. 3.2 shows that the librons do not soften to zero energy or broaden remarkably at the order-disorder transition. Instead, the librons abruptly decrease in intensity at the same time as the Lorentzian scattering grows rapidly in intensity.

The Raman data presented were collected using 894.60 nm excitation, although identical results were obtained using 780.25 and 794.98 nm excitation (these wavelengths correspond to the ground state absorptions of atomic rubidium which was also used as a filter medium). The features shown in Fig. 3.1 were reproducible and maintained the same intensity relative to the intramolecular modes in all of the large number of samples studied, although different samples did have different backgrounds underlying the Raman signal.

Figure 3.3 shows a Raman spectrum taken at 77 K in which librational fine-structure is clearly evident. INS studies of both powdered [92N]and single crystal [92Pb] C_{60} have observed a broad (8 cm^{-1} FWHM) librational peak at ~20 cm^{-1}, in good agreement with the sharp peaks appearing at 17.9, 20.9, and 24.5 cm^{-1} in Fig. 3.3. In their INS study of single-crystal C_{60}, Pintschovius *et al* [92Pb] also reported broader librational peaks at 29 and 37 cm^{-1}, in correspondence with some of the higher energy structure seen in Fig. 3.3. Pintschovius *et al* found no softening or broadening of the 20 cm^{-1} librational peak, although as mentioned previously, the poorer energy resolution of INS relative to Raman spectroscopy may account for the inability of INS to detect the mode softening and broadening which is clearly seen in our single-crystal samples. Also visible in Fig. 3.3 is weak scattering extending up to twice the energy of the highest

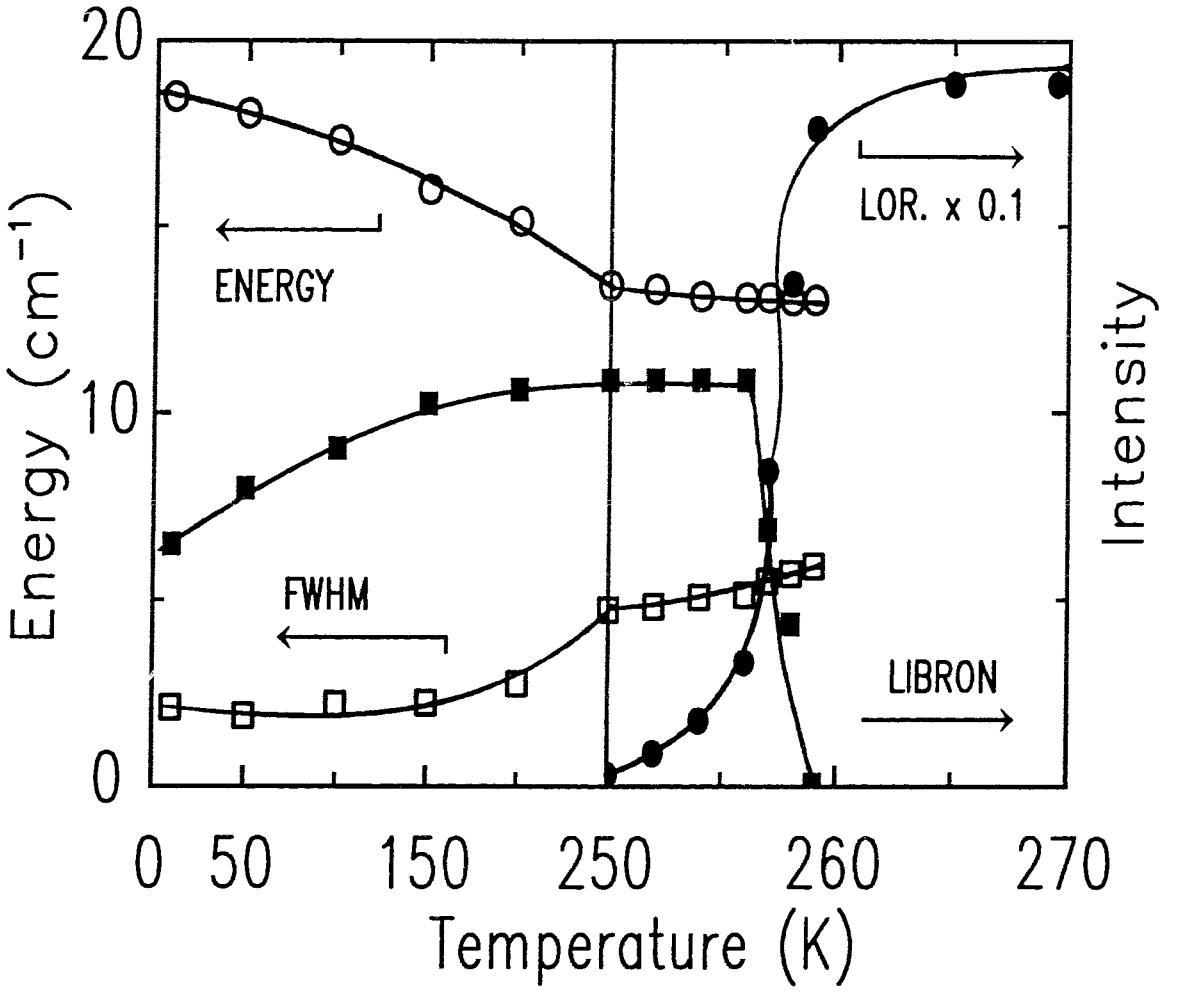

Fig. 3.2 Temperature dependence of the librational peak energy (○), FWHM (□), and integrated Stokes intensity (■). The uncorrected Lorentzian scattering intensity (●) has been scaled down by a factor of 10. Note that two different temperature scales are used above and below 250 K, so the apparent change of the slope of the energy and FWHM curves at 250 K is not real.

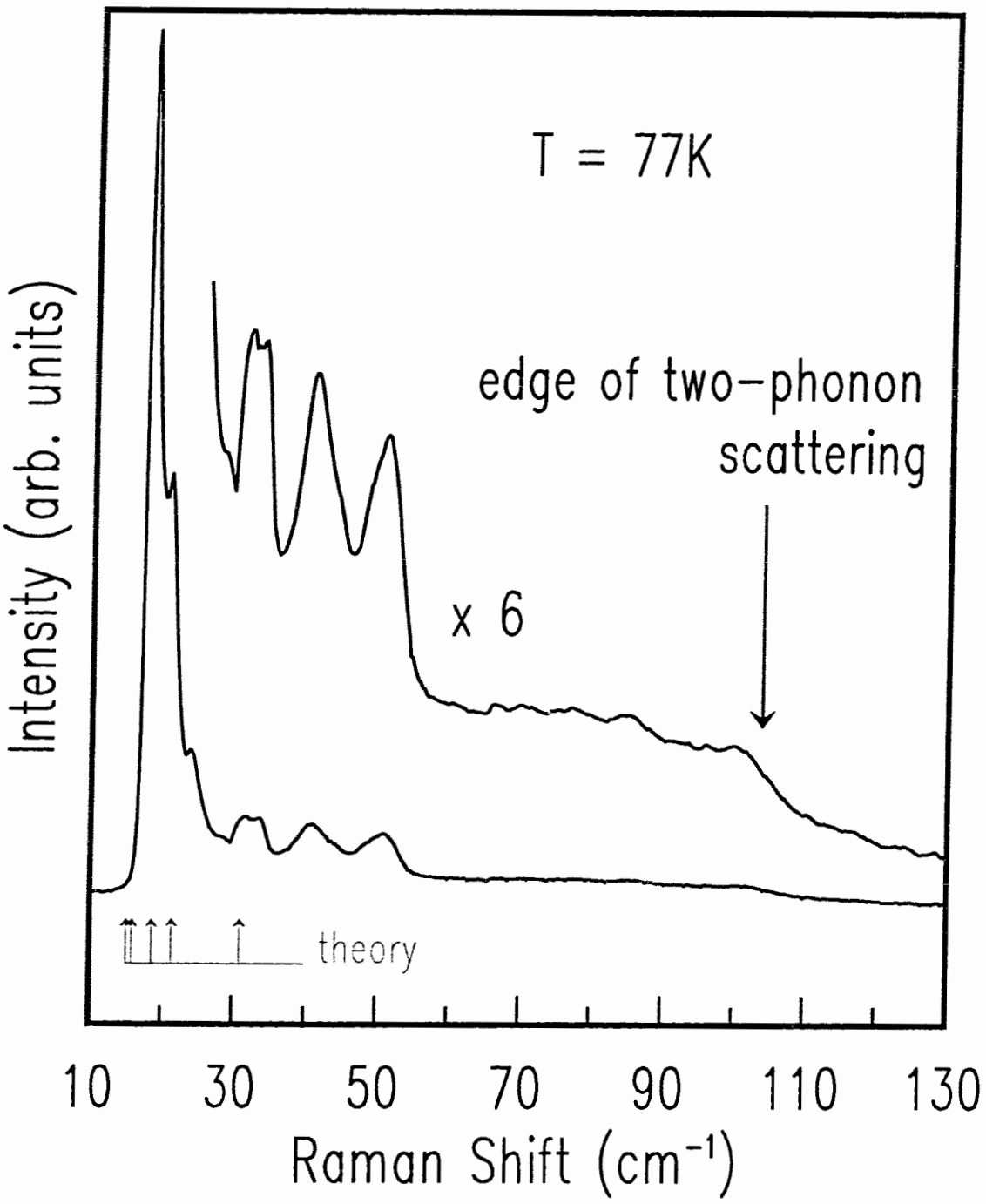

Fig. 3.3 Stokes scattering from crystalline C_{60} at 77 K. The peak intensity of the lowest energy libron (17.9 cm^{-1}) is $\sim 1/180$ that of the $A_g(1)$ intramolecular mode at this temperature. Arrows labeled theory are predictions of libron mode energies, taken from Ref. 94Yb.

energy peak. This scattering arises from the first overtone spectrum of the intermolecular modes, and the absence of sharp features within the overtone spectrum is indicative of broad dispersions within the libron bands.

The peak intensity of the strongest libron mode at 77 K is $^1/_{180}$ that of the first A_g *intramolecular* phonon (at ~497 cm^{-1}). It is this extremely weak Raman intensity of the librons, combined with their small Raman shift, which has conspired to make their detection so difficult, leading to a number of false reports of Raman scattering from libron modes prior to this work [92Lb, 92Lc, 93M].

For the completely ordered low-temperature phase of solid C_{60}, the group-theoretical representations to which the twelve zone-centre librons belong are given by [92Yc, 92Dc]:

$$\Gamma_L = A_g + E_g + 3F_g \qquad (3.1)$$

where A_g, E_g, and F_g are single, double, and triple degeneracy representations, respectively. In the absence of additional perturbations, therefore, one expects at most five Raman-active librons. Several numerical calculations of the five zone-center libron frequencies have been reported in the literature [91Cb, 92L, 92Ld, 92S, 92Yc] using a variety of model potentials for the intermolecular interactions. The libron energies are determined by the intermolecular interactions, not only the functional form of the potentials between interaction centers, but also the symmetry of the interaction centers. It has been demonstrated that models which include only interaction centers at carbon atom sites are unable to reproduce the correct ground-state configuration [91G, 91Cb]. Clearly, models incorporating interaction centers other than at carbon atom sites are needed. The most successful ones are the bond-bond charge interaction model proposed by Lu, Li, and Martin [92L], and the atom-bond interaction model proposed by Sprik, Cheng, and Klein [92S]. In the bond-bond interaction model, it is assumed that there is a net charge q at the

center of each bond. Since there are 30 short bonds and 60 long bonds in a C_{60} molecule, charge neutrality requires that $q_{\text{short bond}} = -2q_{\text{long bond}}$. The potential between two C_{60} molecules is given by a Lennard-Jones interaction between carbon atom sites plus an electrostatic interaction between bond centers. In the atom-bond model proposed by Sprik, Cheng, and Klein, the C_{60} molecule is represented by a rigid frame with Lennard-Jones interaction centers on carbon atoms as well as the midpoints of the short bonds. The magnitude of the interaction is assumed to be the same for all sites. In addition, all the sites carry charges. The interaction between molecules is therefore given by Lennard-Jones potentials between atom sites and short-bond centers, as well as electrostatic potentials between atom sites and short-bond centers. Although both of these models lack a firm theoretical basis, their simplicity and their success in describing the ground-state structure and orientational order-disorder phase transition make them popular starting points for theoretical studies of solid C_{60}.

Both the bond-bond and atom-bond models predict libron energies to vary between 7-24 cm^{-1}. Other detailed results are very much model dependent. For example, the atom-bond potential predicts that the lowest energy mode at the Γ point is an A_g mode, and there are five distinct libron frequencies, while for the bond-bond potential the lowest modes at the Γ point are accidentally degenerate E_g and F_g modes, with only four distinct libron frequencies appearing. While the theoretically predicted energy range of 7-24 cm^{-1} includes the lowest-energy experimentally observed modes, there is no indication in the Raman data shown in Figs. 3.1 and 3.3 of scattering lower in energy than the strongest mode, appearing at 18.5 cm^{-1} at 10 K.

A more recent theoretical study has been reported by Yu *et al* [94Yb] in which a modified bond-bond charge model was used. In contrast to assuming a rigid molecule, all degrees of freedom of the C_{60} molecules in the solid were treated explicitly. The libron frequencies predicted by the numerical calculations of Yu *et al* are shown in Fig. 3.3 by

arrows labeled "theory". As can be seen in Fig. 3.3, the agreement with the experimentally observed libron energies is much improved.

While the lowest energy modes shown in Fig. 3.3 are in approximate agreement with the most recent calculations of the libron frequencies, the broader, higher energy structure remains unaccounted for. Given the T_h^6 space group of the low-temperature phase, only five Raman-active zone-center librons are expected ($A_g + E_g + 3F_g$), while the four translational optic phonons are all of ungerade symmetry ($A_u + E_u + 2F_u$) and so should not be Raman-active. It is unlikely that the weaker structure seen in Fig. 3.3 arises from a splitting of the degenerate E_g or F_g modes given the large frequency shift of these features relative to the energies of the intense peaks. Activation of the otherwise silent translational phonons would be a more likely explanation. The two IR-allowed F_u phonons have in fact been measured at 40.8 and 54.8 cm^{-1} [93F, 93H], an energy range which is comparable to the observed Raman structure. Several symmetry-breaking mechanisms are available in the solid to account for silent mode activation, most notably the orientational disorder of the low-temperature phase, and the isotopic disorder present in the crystal due to the random substitutions of ^{13}C for ^{12}C. Both of these effects are discussed in detail in Sections 3.3 and 3.4.

3.3 The Isotope Effect in the Intermolecular Mode Spectrum

The 1.1% natural abundance of ^{13}C implies that approximately half of the C_{60} molecules made from natural carbon will contain at least one ^{13}C atom, which represents a dramatic reduction in the symmetry of the molecule. This isotopic disorder is often cited in the literature as a possible source of silent *intramolecular* mode activation [93Db, 93Wb], and could account for the additional structure seen in the low-energy Raman spectra of Figs. 3.1 and 3.3.

To explore the influence of isotopic disorder on the low-energy Raman spectra of solid C_{60}, crystals grown from isotopically controlled starting material were studied. In

addition to crystals grown from naturally abundant carbon (1.1% ^{13}C), C_{60} crystals were fabricated from 99.95% pure ^{12}C, and 99.7% pure ^{13}C starting powder. The mass spectra of these isotopically engineered crystals are shown in Figure 3.4. As can be seen in Fig. 3.4, natural C_{60} contains significant amounts of $^{13}C^{12}C_{59}$ and $^{13}C_2{}^{12}C_{58}$. However, by using a starting purity of 99.95% ^{12}C, crystals which are 99.7% $^{12}C_{60}$ were achieved. As shown in Fig. 3.4, a ^{13}C purity of 99.7% led to a solid in which 85% of the molecules are $^{13}C_{60}$. For the sake of simplicity, the 99.7% $^{12}C_{60}$ crystals and 85% $^{13}C_{60}$ crystals will be referred to as 'crystalline $^{12}C_{60}$' and 'crystalline $^{13}C_{60}$', respectively.

The dependence of the intermolecular Raman bands on the isotopic content of the C_{60} crystals is shown in Figure 3.5. The structure arising from crystalline $^{12}C_{60}$ and $^{13}C_{60}$ is identical to that of samples made from naturally abundant carbon, shown in Fig. 3.3. The intensity ratios of the strong modes to the weaker fine-structure is constant among the three materials, while the mode energies are identical, apart from a uniform softening of the $^{13}C_{60}$ frequencies by a factor of 0.96 ± 0.01. The libron (and phonon) energies should scale as $m^{-\frac{1}{2}}$, where m is the atomic mass, and so one expects a softening of the $^{13}C_{60}$ spectrum by the factor of $\left(\frac{12}{13}\right)^{\frac{1}{2}} = 0.96$ seen in Fig. 3.5. The mass shift of all the features seen in low-energy Raman scattering confirms their identity as lattice modes of solid C_{60}, while the invariance of the fine-structure intensities with isotopic content eliminates the possibility that any of the features arise from isotopic disorder.

The spectra shown in Fig. 3.5 have been scaled by matching the intensities of the $A_g(1)$ intramolecular mode. The absolute intensities of the $^{12}C_{60}$ and $^{13}C_{60}$ librons were in fact comparable, but since the collection efficiency can never be exactly duplicated from one sample to the next, absolute intensities are somewhat meaningless. The relative libron intensities are, however, identical; the ratio of the $A_g(1)$ mode peak intensity to the strongest libron peak is 180:1 at 77 K for all three isotopic compositions. A recent theoretical calculation has suggested that large differences between the libron spectrum of

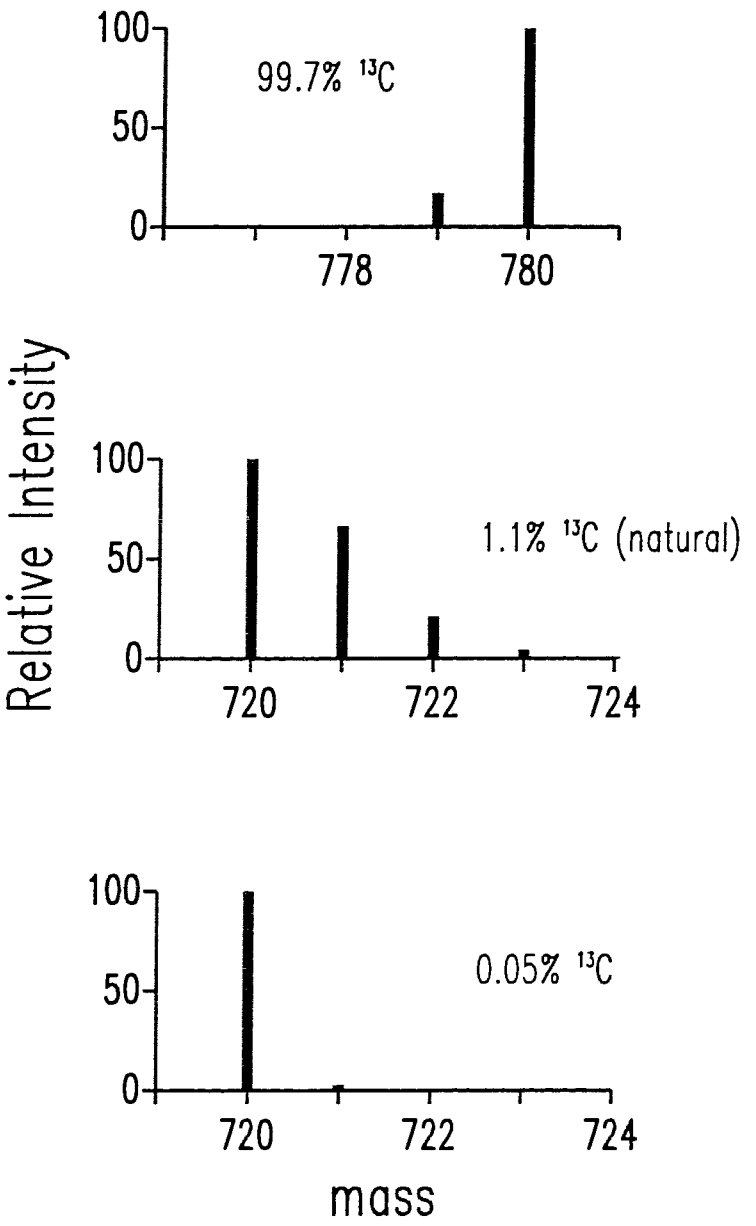

Fig. 3.4 The measured mass abundances of C_{60} molecules made from isotopically enriched graphite rods and rods made from naturally abundant carbon (1.1% ^{13}C).

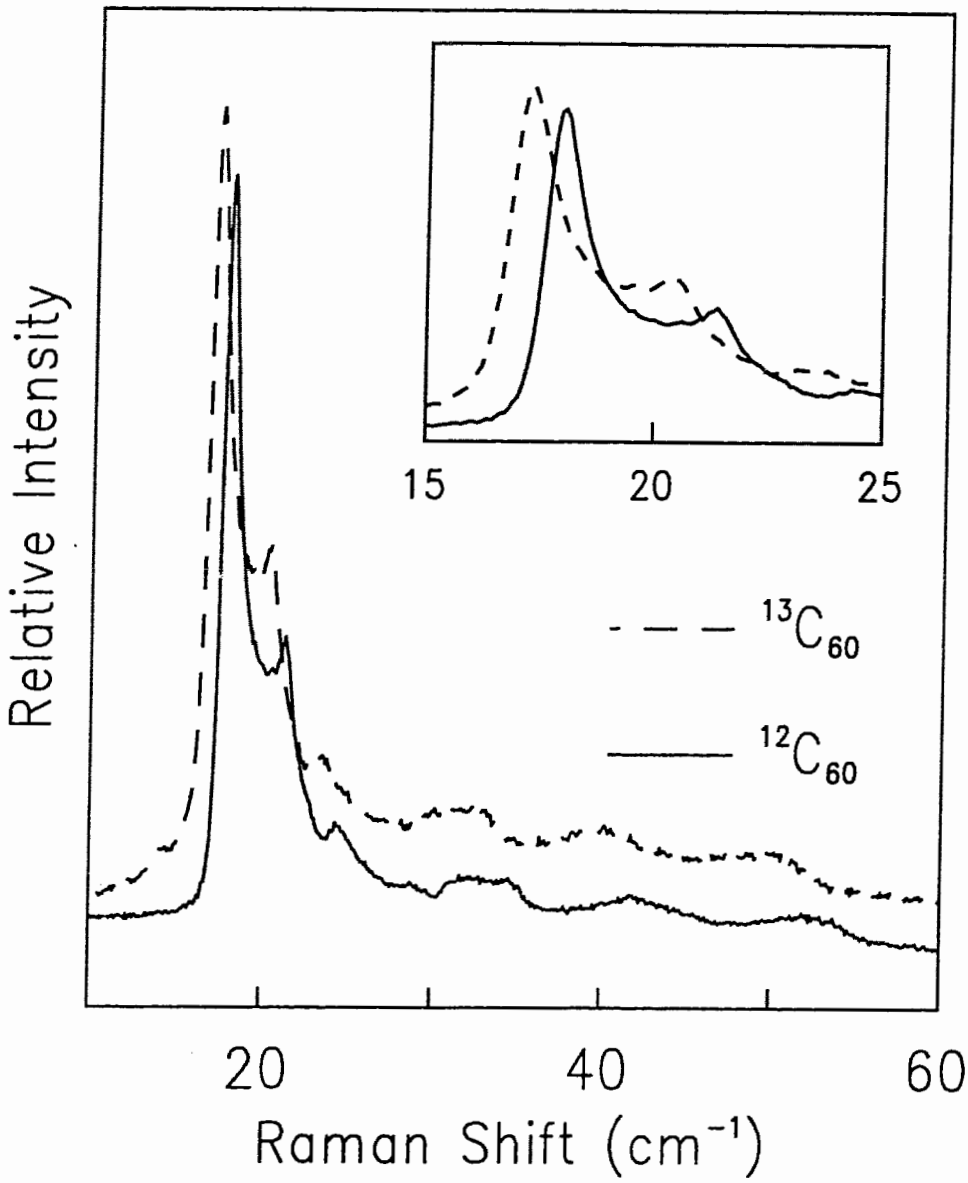

Fig. 3.5 Raman scattering from librons in isotopically purified $^{12}C_{60}$ and $^{13}C_{60}$ crystals, T=77 K. The spectra have been scaled by matching $A_g(1)$ intramolecular mode intensities, while the $^{13}C_{60}$ spectrum is shifted upward for clarity.

natural C_{60}, $^{12}C_{60}$, and $^{13}C_{60}$ would appear due to the differing nuclear spins of ^{12}C and ^{13}C [94S]. The additional symmetry restrictions arising from the nuclear-spin state imply that only A_g librations should appear in $^{12}C_{60}$ material, while $^{13}C_{60}$ allows all librations with varying (non-zero) probabilities. This prediction, however, is not borne out in experiment, as seen in Fig. 3.5.

3.4 Merohedral Disorder in the Intermolecular Mode Spectrum

In the previous section, the isotopic disorder of natural C_{60} crystals was shown to play no role in the activation of the libron fine-structure. Additional disorder is present in the low-temperature ($T < 260$ K) phase of solid C_{60}, however, in the form of misoriented molecules. This orientational, or merohedral, disorder of the solid can be reduced by lowering the temperature of the sample, but a residual amount will always be present given the glass transition at ~90 K, below which further reorientations are frozen out.

To explore the influence of the merohedral disorder on the libron spectrum, samples were studied in which differing amounts of disorder were incorporated at a fixed temperature. Varying the amount of disorder present in the crystal at a given temperature (below 90 K) was achieved by varying the rate at which the crystal was cooled into the glassy phase. The reorientations of the molecules freeze out on the laboratory time scale at ~90 K due to a ~260 meV barrier to reorientations [92G, 92Sb, 92Yb]. Given this and the approximately 12 meV energy difference between the ordered and disordered orientation of a molecule, ~17% of the molecules will be misoriented at the lowest temperatures if the sample is cooled slowly so that it enters the glassy state at ~90 K [92D]; a higher percentage of misorientations is possible by rapidly quenching the sample, which freezes in the disorder at a higher temperature. In Figure 3.6, the 77 K libron spectrum of crystalline C_{60} is shown for three different cooling rates. The 'slow' quench was achieved by cooling the sample from ~130 K to 85 K over the course of 24 hours and then cooling to 77 K, while a 'medium' quench corresponded to cooling the

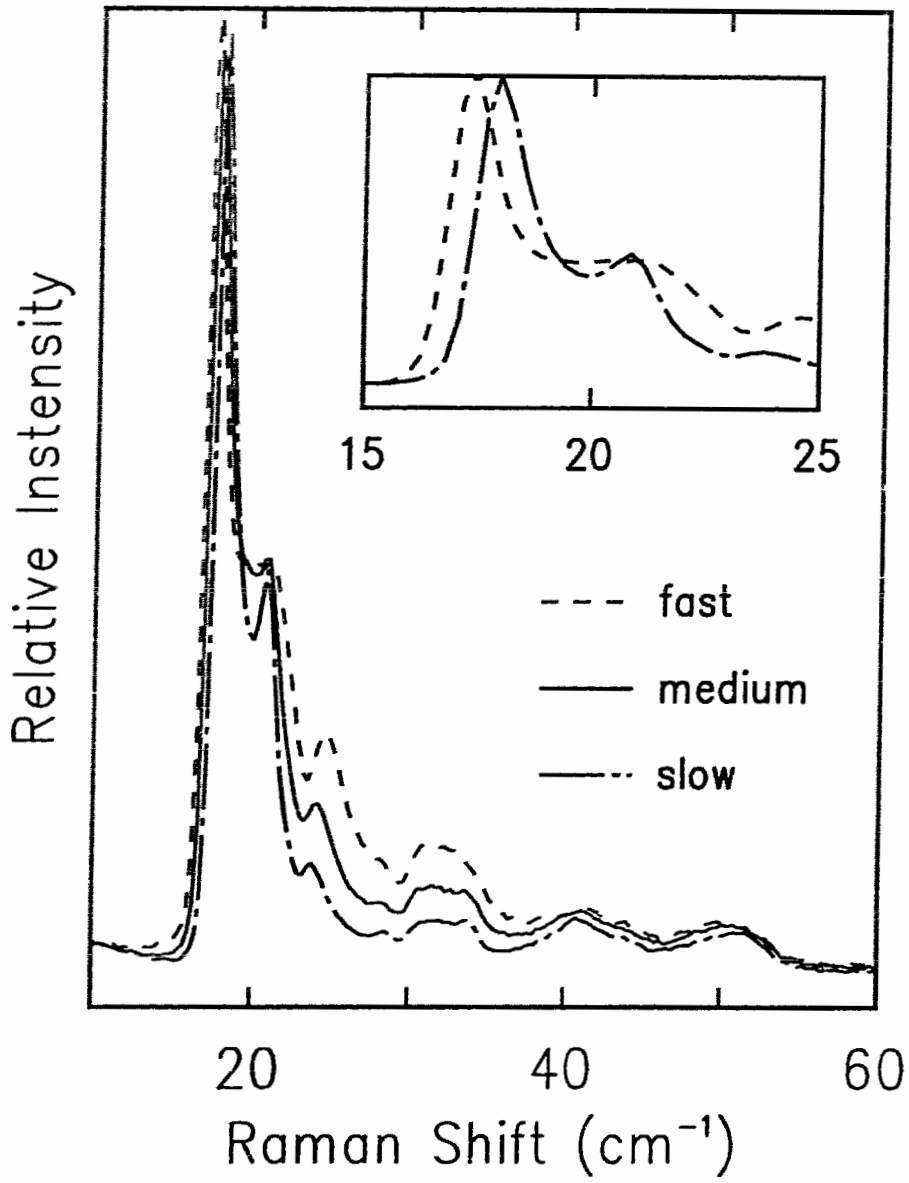

Fig. 3.6 Low-energy Stokes scattering from crystalline C_{60} at 77 K as a function of the rate at which the crystals were cooled. See text for an explanation of fast-, medium-, and slow-quench rates. Spectra have been scaled by matching $A_g(1)$ intramolecular mode intensities.

sample from room temperature to 77 K in a matter of minutes. The 'fast' quench spectrum was generated by dropping the crystals directly from room temperature into superfluid helium and then raising the temperature to 77 K. Samples were also quenched rapidly from 220 K into superfluid helium; no difference was found between these and samples quenched directly from room temperature, in which the crystals first pass through the ordering transition. The libron peaks shown in Fig. 3.6 have been scaled to the intensity of the $A_g(1)$ intramolecular mode. A measurement of the *intramolecular* mode spectrum under these exact conditions revealed that the 'fast' quench sample entered the glassy phase at approximately 115K. Significant differences between the three spectra are clearly visible. The intensity of most of the weaker features increases as the amount of orientational disorder is raised, while the inset of Fig. 3.6 shows that the strongest mode softens in energy. The second most intense libron peak also displays a dramatic increase in linewidth from the slow to the fast quench. All of these changes are independent of the exact temperature (below 90 K) at which the measurements are made; the same results are seen at 35 K or 4 K.

The pronounced increase in the intensity of the weaker Raman features with increasing disorder suggests that these transitions are indeed activated by the merohedral disorder. The ideal experiment, of course, would involve reducing the orientational disorder to zero and observing the resultant libron bands. Unfortunately, no means of preparing a crystal with 100% of its molecules in the Γ_1 orientation has been found. We have discovered, however, what may be the next best thing: the proportion of molecules in the alternate, 'misoriented' orientation (the Γ_2 orientation) can be made arbitrarily large through the application of hydrostatic pressure [95W]. Thus a completely ordered crystal is obtained, but the orientation of the molecules is rotated from that of the conventional low-temperature phase. In this completely ordered crystal, the new libron spectrum is drastically simplified, lending further evidence that the fine-structure seen in Fig. 3.6 does arise from the merohedral disorder of the conventional crystal. The method by which the

new, completely ordered state of solid C_{60} is arrived at is discussed in Chapter 5, where the effects of hydrostatic pressure on both the librons and intramolecular phonons is detailed.

Only one theoretical study of the effects of orientational disorder on the phonon modes of C_{60} has been reported. Using a simple, non-random simulation of the orientational disorder, Yu *et al* [94Yb] found that rotating one molecule per unit cell led to an energy softening of the libron density of states. This is in agreement with the experimentally observed softening of the main libron mode, shown in Fig. 3.6.

3.5 Impurity Effects in the Intermolecular Mode Spectrum

Raman scattering from librons in C_{60} remains a contentious subject in regard to the role played by impurities such as intercalated O_2. It has been suggested that the features we have observed in Raman scattering and ascribed to lattice modes of C_{60} were in fact due solely to impurities [94Y]. In the only experimental evidence for an extrinsic origin of these features, Burger and Kuzmany found that they were able to detect these bands in air-exposed crystals, but not in "oxygen-free" samples [94Yb]. They retained the idea that the observed features were due to C_{60} libron scattering, but induced by the random perturbations of impurities resulting from atmospheric exposure. Given oxygen's high diffusivity in C_{60}, it is conceivable that oxygen or similar impurities could influence the intermolecular mode spectrum.

The possibility that the features we see in low-energy Raman scattering are impurity modes can be discounted based upon the results of Section 3.3. The $m^{-\frac{1}{2}}$ dependence of the transition energies, where m is the mass of the constituent atoms in the crystal, unequivocally identifies the Raman bands as arising from carbon rotations and/or vibrations. To investigate the possibility that the optical activation of the libron modes stems from the presence of intercalated atmospheric gases, the libron modes have been studied as a function of air-exposure.

When exposed to ambient conditions, C_{60} crystals absorb molecular oxygen, as revealed by the characteristic luminescence at 1.3 μm of singlet molecular oxygen [92Nc]. While singlet O_2 luminescence has been observed in a wide range of host materials, C_{60} is the only solid state host from which singlet O_2 luminescence has been reported. Luminescence at 1.3 μm results from the singlet excited state of O_2 relaxing back to its triplet ground state, and provides therefore a means of verifying the presence of O_2 in solid C_{60}. On the left of Figure 3.7a), the singlet O_2 luminescence originating from a C_{60} crystal which was exposed to air for several months is shown, along with the Raman-active libron spectrum on the right. The luminescence was generated using 710 nm wavelength excitation, while 794.98 nm excitation was used to measure the low-energy Raman spectrum. In Fig. 3.7b), the same spectra are shown for a crystal which was grown in a quartz tube evacuated to better than 6×10^{-8} Torr during and after the growth. The quartz tube was then inserted into a liquid helium dewar without breaking vacuum. Pure helium gas was then backfilled into the cold quartz tube and condensed into liquid. The singlet O_2 luminescence spectra in Fig. 3.7 are scaled by matching the intensities of the near-gap luminescence spectra for each sample, while the Raman spectra are scaled by matching the $A_{g(1)}$ peak intensities, as discussed earlier. No molecular oxygen emission is visible in the sample which was kept free of atmospheric exposure, while the low-energy Raman bands remain unchanged both in structure and intensity.

The relative libron amplitudes of the air-free crystals are identical to those of the large collection of air-exposed crystals we have studied, produced both from commercial high-purity C_{60} powder and from various isotopic compositions made and purified in-house. The invariance of the low-energy Raman bands from sample to sample provides strong evidence that the Raman spectra shown in this work depict the intrinsic Raman intensity of the libron modes of pure, crystalline C_{60}. It is possible that intercalated gases such as O_2 may raise the libron scattering intensity above this intrinsic level, accounting

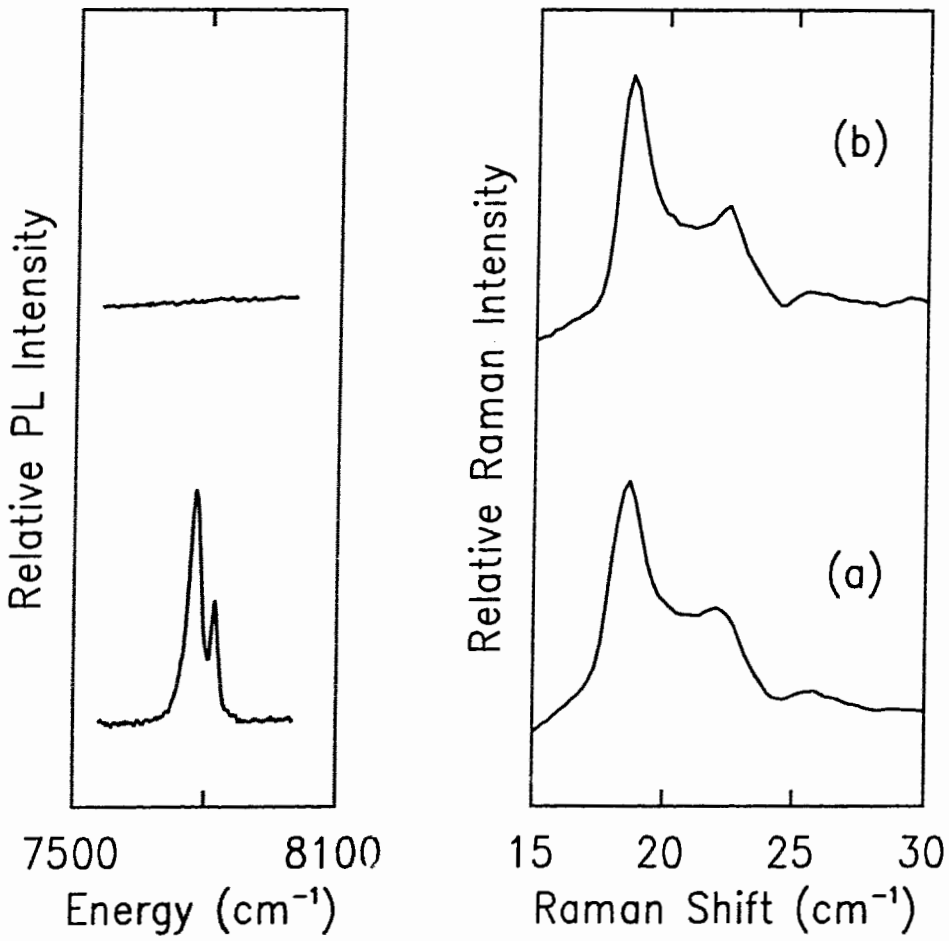

Fig. 3.7 Singlet O_2 luminescence (left) and C_{60} librons (right) at 4.2 K as a function of the intercalated O_2 content. Shown are (a) crystals which have been exposed to ambient conditions for several months, and (b) crystals which were grown and subsequently immersed in liquid He without breaking vacuum. The photoluminescence (PL) spectra are scaled by matching the near-gap luminescence intensities, while the libron spectra are scaled by matching the $A_g(1)$ intramolecular mode intensities.

for the variation with air exposure seen by Burger and Kuzmany [94Bb], but as no intensity scaling was provided in their report, direct comparison with our results is difficult.

3.6 Polarized Raman Scattering from the Intermolecular Modes

An additional strength of Raman spectroscopy is the ability to identify the symmetry of observed transitions by varying the scattering geometry used. The intensity of the scattered light due to a phonon with a Raman tensor $\vec{R}$ is proportional to $\left|\vec{E}_s \cdot \vec{R} \cdot \vec{E}_i\right|^2$, where $\vec{E}_i$ and $\vec{E}_s$ are the incident and scattered light electric field vectors. With the symmetry of the Raman tensor for a given phonon in hand, suitable scattering geometries (directions of $\vec{E}_i$ and $\vec{E}_s$) can be chosen to distinguish the symmetries of the observed bands. For the T_h^6 space-group of the low-temperature phase of C_{60}, the forms of the Raman tensors will be [78H]:

$$\begin{pmatrix} a & 0 & 0 \\ 0 & a & 0 \\ 0 & 0 & a \end{pmatrix} \quad ; \quad \begin{pmatrix} b & 0 & 0 \\ 0 & b & 0 \\ 0 & 0 & -2b \end{pmatrix}, \begin{pmatrix} 0 & 0 & 0 \\ 0 & -b & 0 \\ 0 & 0 & b \end{pmatrix} \quad ; \quad \begin{pmatrix} 0 & c & 0 \\ c & 0 & 0 \\ 0 & 0 & 0 \end{pmatrix}, \begin{pmatrix} 0 & 0 & c \\ 0 & 0 & 0 \\ c & 0 & 0 \end{pmatrix}, \begin{pmatrix} 0 & 0 & 0 \\ 0 & 0 & c \\ 0 & c & 0 \end{pmatrix} \qquad (3.2)$$

A_g E_g F_g

Using the above Raman tensors, a series of scattering geometries can be devised which will differentiate the A_g, E_g, and F_g mode symmetries. Such a series, for the simple case of collinear excitation and scattered beams, perpendicular to a <100> crystal face, is shown in Table 3.1. In Table 3.1, the setting angle ϕ refers to the angle of the incident light polarization relative to a <001> crystal direction while || and $\perp$ refer to the relative orientations of the incident and scattered light polarizations. Thus 0° || implies that

TABLE 3.1. Raman-active modes of solid C_{60} under various scattering geometries. The setting angle ϕ refers to the angle of the incident light polarization relative to the [001] crystal direction while $||$ and $\perp$ refer to the relative orientation of the incident and scattered light polarization.

setting angle ϕ	analyzer	backscattering from {100} face
0°	$\|\|$	$A_g + E_g$
	$\perp$	F_g
45°	$\|\|$	$A_g + E_g + F_g$
	$\perp$	E_g

$\vec{E}_i \propto (0,0,1)$ and $\vec{E}_s \propto (0,0,1)$, while 45° $||$ implies that $\vec{E}_i \propto (0,1,1)$ and $\vec{E}_s \propto (0,1,1)$, and so forth. Clearly, if Raman scattering measurements of the libron bands were made under all the geometries listed in Table 3.1, a complete symmetry identification of all the modes should be possible.

Unfortunately, no polarization dependence of the low-energy bands was initially detected. In contrast, well-defined polarization dependences are routinely reported in Raman scattering from the *intramolecular* modes [93M]. Were the libron modes activated by random impurity fields, one would not expect the bands to remain polarized, and so the apparently unpolarized nature of the libron Raman scattering was used by Burger and Kuzmany [94Bb] to argue for an extrinsic origin of the optical activity of the libron modes. However, all reported Raman scattering studies of the libron modes have been, by necessity, carried out using near-infrared excitation, while the polarization studies of the *intramolecular* modes were performed using visible excitation. The penetration depth of light in the blue-green range of the spectrum is only a few microns in

solid C_{60} [92Lc], and so, provided a smooth, shiny crystal face is used for the Raman experiments, no depolarization of the incident or emerging scattered light is likely to occur. In the near-infrared (0.8 -1 μm), C_{60} is quite transparent, and a significant fraction of the laser light incident on a crystal face will be back-reflected from the opposite face. If the back surface is rough, the back-reflected laser or Raman light will be strongly depolarized. The morphology of crystals grown via vapour transport was such that back-reflection from a rough surface was unavoidable (see for example the crystal depicted in Fig. 2.4). This surface roughening arose due to contact of the crystal with the quartz tube during growth. It is the diffuse scattering from the rough surface of the crystal, combined with the large refractive index of C_{60} (which leads to multiple internal reflections) which leads to the depolarization of the Raman signals. If near-infrared excitation is used, the intramolecular modes appear to be unpolarized as well.

To circumvent the depolarization of the Raman signal from rough crystal surfaces, several of the larger crystals (at least one face of the crystal measuring > 3 mm per side) were chosen for mechanical and chemical polishing. For each crystal, the side of the sample opposite a well-developed face was lapped smooth by means of a 0.3 μm grit alumina powder, and then chemically polished using a polishing pad soaked in cyclo-hexane (a weak solvent of C_{60}). The final thickness of the resultant platelets was typically 1 mm. The polished crystals were oriented in a cryostat such that the laser excitation was incident on the growth face, and exited the crystal through the polished face.

Shown in Fig. 3.8 is the polarization dependence of the low-energy Raman bands of solid C_{60}, at 50 K. The data in Fig. 3.8 were collected using the CCD array detector to capture only the Raman signal originating directly from the area of the incident laser spot and not the edges of the crystal. A {100} crystal face was used for the backscattering measurements, and the excitation and collection directions were normal to the sample surface. In Fig. 3.8, the setting angle ϕ refers to the angle of the incident light

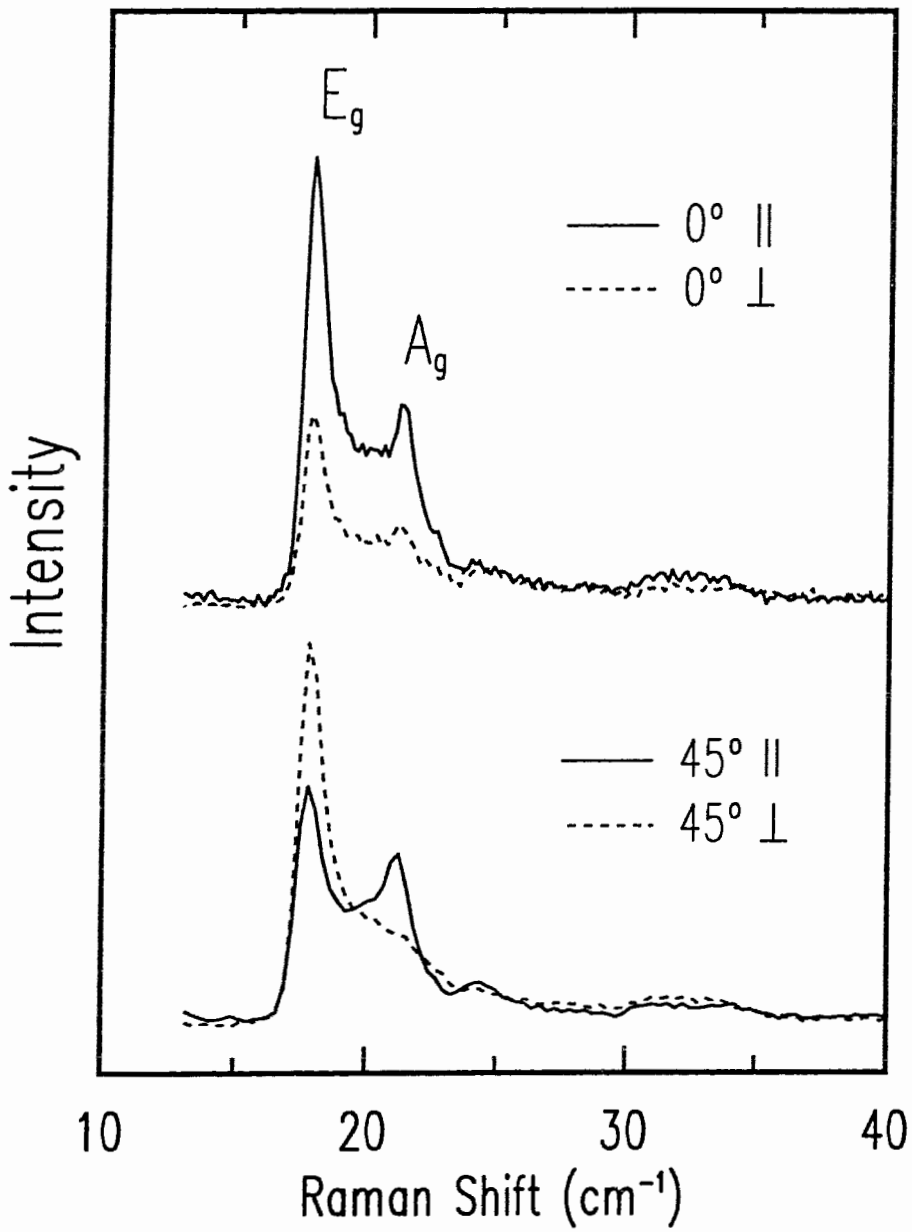

Fig. 3.8 Polarization dependence of the Raman-active lattice modes of crystalline C_{60}. The measurements were made from a {100} face of the crystal in a backscattering geometry; T=2 K. 0° and 45° refer to the angle of the laser polarization to the [001] direction, while parallel and perpendicular refer to the relative orientation of the incident and scattered light polarizations.

polarization relative to a <001> crystal direction while || and ⊥ refer to the relative orientations of the incident and scattered light polarizations. The depolarization ratio ρ (where $\rho = I_{\perp}/I_{||}$) of the $A_g(1)$ *intramolecular* mode was found to be 0.25, under the same conditions used for the measurement of the intermolecular modes, shown in Fig. 3.8. This value of ρ is an order of magnitude greater than the value which is typically reported using visible excitation [93M], indicating that some Raman light generated by diffusely scattered laser excitation is still being collected, thereby increasing the observed depolarization ratio from what would be expected. Thus, while the depolarization ratios seen in Fig. 3.8 are not the true values for the various modes under consideration, the trends indicated by the measurements do allow a symmetry identification of the components. By referring to Table 3.1, it is clear that the mode seen in Fig. 3.8 at 18.0 cm^{-1} is of E_g symmetry, while the second resolved libron mode at 21.3 cm^{-1} (at 50 K) is of A_g symmetry. Unfortunately, the higher energy, weaker modes which extend out to ~50 cm^{-1} are not seen with sufficient signal-to-noise to determine their polarization response.

3.7 Summary

Well resolved Raman scattering from the lattice modes of crystalline C_{60} has been observed. The low-energy bands seen in Raman scattering are proven to arise from carbon rotations and/or vibrations by fabricating isotopically pure $^{12}C_{60}$ and $^{13}C_{60}$ crystals and observing the expected $m^{-\frac{1}{2}}$ dependence of the mode energies. The assignment of the observed bands to lattice modes is confirmed by the abrupt disappearance of the bands above the order-disorder transition, combined with the reasonable agreement between the observed energies and the energies determined by inelastic neutron scattering. The Raman measurements presented in this Chapter indicate that the lowest-energy libron mode lies at 18.5 cm^{-1} (at 10 K), in contrast to popular

theoretical models of the intermolecular potential which are too soft by at least a factor of two.

The Raman spectrum of the libron modes is richly structured, with more peaks appearing at low temperature than would be expected from a group-theoretical analysis of a completely ordered crystal. The libron structure is identical between crystals made from naturally abundant carbon and 99.95% ^{12}C, indicating that isotopic disorder is not the source of the additional modes. The residual orientational disorder of the crystal, however, was shown to strongly affect the bulk of the libron spectrum. The orientational disorder could, therefore, be the source of the additional structure, either through splittings of the degenerate libron modes, or by activating the otherwise-silent translational phonons.

The intensity of the libron bands reported here is argued to be the intrinsic Raman activity of the modes. This is based upon the invariance of the mode intensities over the large collection of samples studied, including samples grown and studied without exposure to atmosphere. The apparently unpolarized nature of the Raman scattering from the librons has been shown to stem from the experimental conditions used to measure the modes, rather than evidence of an impurity activation of the Raman intensity. By using polished crystals, the polarization dependences of the librons has been determined, allowing a symmetry identification of the two most-intense modes.

CHAPTER FOUR

RAMAN SCATTERING FROM INTRAMOLECULAR PHONONS

4.1 Introduction

The paucity of experimental studies of the intermolecular phonons of C_{60} is sharply contrasted by the prodigious experimental effort which has been directed towards the intramolecular phonons [91C, 91P, 92C, 92Db, 92Lb, 92Lc, 93Db, 93M, 93Wb]. These studies have focused mainly on determining the energies of the modes, which in turn are used as benchmarks for testing the numerous theoretical descriptions of the bonding of molecular C_{60} [87W, 88W, 89W, 92F, 92J, 92Jb, 92Nb, 92O, 93S, 93W]. In Raman scattering from an isolated molecule, only 10 ($2A_g + 8\ H_g$) of the 46 ($2A_g + 3F_{1g} + 4F_{2g} + 6G_g + 8H_g + A_u + 4F_{1u} + 5F_{2u} + 6G_u + 7H_u$) non-degenerate molecular modes are active, while in the solid, the crystal field should lead to the Raman-activation of all 23 gerade modes. In practice, the activation of the additional gerade modes is very weak, and not all of the 23 expected modes are detected. This stems from the intermolecular forces present in the crystal being much weaker than the intramolecular forces, as is typical of a molecular solid. However, the majority of the internal modes, including the ungerade vibrations, have been measured in Raman scattering, via second-order scattering events [93Db]. The first combination mode spectrum of C_{60} (sums and differences of the first-order vibrations) contains many sharp features (again, reflective of the molecular nature of the solid) which have been used to extract the energies of modes which do not appear in the first-order spectrum. In this manner, virtually all of the vibrational mode energies have been determined.

While the coarser features of the crystalline C_{60} Raman spectrum are well understood, much less is known regarding vibrational fine-structure of the internal

modes. Raman fine-structure has been reported for a small number of the internal modes, and tentatively assigned to the expected crystal field splittings of the degenerate molecular vibrations [92Lb, 92Lc, 93M]. However, other possibilities for the origin of the vibrational fine-structure exist, most notably the orientational and isotopic disorder of the crystal, as discussed in Chapter 3 in the context of the intermolecular modes. A recent Raman study of isolated C_{60} molecules (a frozen solution of C_{60} in CS_2) made from natural carbon has shown that the $A_g(2)$ mode at ~1468 cm^{-1} can be resolved into components arising from $^{12}C_{60}$, $^{13}C^{12}C_{59}$, and $^{13}C_2{}^{12}C_{58}$ vibrations [94G]. It is not unreasonable, therefore, to expect a similar behaviour from the molecular solid.

In this Chapter, a high-resolution Raman scattering study of the intramolecular phonon spectrum of crystalline C_{60} is presented. Vibrational fine-structure, both above and below the 260 K phase-transition temperature is shown to be present in the vast majority of the Raman-active molecular modes, as well as in two of the silent modes (vibrations which are allowed in the solid state but optically-silent in an isolated molecule). The small splittings of the phonons are resolvable due to the narrow vibrational linewidths of the modes, many of which are more than an order of magnitude narrower than previously reported. The majority of the observed splittings do not arise from isotopic disorder, as determined by comparing spectra of crystals made from naturally abundant carbon and 99.95% ^{12}C. Several modes do show slightly reduced linewidths in the ^{12}C enriched samples, while other modes show virtually no change from the naturally abundant material to the 'pure' $^{12}C_{60}$ material. The exception to this behaviour is the $A_g(2)$ mode. In crystalline C_{60} made from naturally abundant carbon, the $A_g(2)$ mode shows a complex structure of at least five components, a structure which is greatly simplified in pure $^{12}C_{60}$ crystals [95Hc]. The $A_g(2)$ structure of crystalline C_{60} is entirely different from that reported earlier for C_{60} in CS_2 [94G], indicating that the fine-structure must arise from an interplay between isotopic and solid state effects. In order to further explore the unexplained behaviour of $A_g(2)$ with isotopic content, crystals with

^{13}C concentrations of 0.5%, 7.3%, 56.1%, and 99.7% have been fabricated and studied. The 0.5% ^{13}C sample is only a small departure from natural abundance, but substantial changes within the $A_g(2)$ band are apparent. In the 7.3% ^{13}C material, the $A_g(2)$ band broadens considerably, but additional splittings are resolvable, while the isotopic disorder of the 56.1% ^{13}C crystal completely 'smears out' the fine-structure of $A_g(2)$. The $A_g(2)$-band seen in the 99.7% ^{13}C material is identical to that of the 99.95% ^{12}C crystals, apart from a $\left(\frac{12}{13}\right)^{\frac{1}{2}}$ energy softening of the mode energies. The complex dependence of the $A_g(2)$ band on the isotopic content of the crystals is contrasted with that of lower energy phonon bands which show no additional splittings with increasing ^{13}C concentration, but simply soften by an energy given by a linear averaging of the isotopic masses present.

As the majority of the observed Raman fine-structure does not stem from isotopic disorder, it can be assigned to the crystal field. However, a significant component of the crystal field splittings observed in the low-temperature phase is shown to arise from merohedral disorder. The small fraction of misoriented molecules within the ordered crystal is seen to affect the energies and intensities of the majority of the vibrational fine-structure. While the influence of the merohedral disorder cannot be distinguished from that of a 'normal' crystal field for all of the Raman bands, the components of several modes will be shown, through a detailed temperature study of the bands, to arise solely from the merohedral disorder [95Hc].

In Section 4.2, the Raman-active intramolecular phonon spectrum of crystalline C_{60} is presented, both in the high-temperature, freely rotating phase, and in the low-temperature, ordered phase. The Raman spectra of isotopically engineered crystals are detailed in Section 4.3, while the effects of merohedral disorder are explored in Section 4.4.

4.2 The Intramolecular Phonon Spectrum

A typical low-temperature Raman spectrum of crystalline C_{60} made from naturally abundant carbon is depicted in Figure 4.1. The large energy gap of ~200 cm^{-1} between the intermolecular modes (which extend to ~60 cm^{-1}) and the lowest energy intramolecular phonon (at ~260 cm^{-1}) lends further support to the interpretation of crystalline C_{60} as a molecular solid. There is no hybridization of inter- and intramolecular vibrations, and the obvious starting point for discussing the intramolecular phonon spectrum is the vibrational mode spectrum of an isolated molecule.

The vibrational modes of a C_{60} molecule have been extensively modeled using a variety of techniques, and the energies are now well-established. The intramolecular phonons which originate from the ten Raman-allowed vibrations of the free molecule are indicated in Fig. 4.1, using the labels appropriate for the I_h symmetry of a free molecule. As can be seen in Fig. 4.1, however, more than simply ten H_g and two A_g molecular modes are visible in Raman scattering from the crystal, while splittings of several modes has occurred, most notably in the lowest energy, $H_g(1)$-derived phonon.

The intramolecular phonon spectrum, along with its temperature evolution is shown in an expanded energy scale in Figure 4.2 (the weak combination bands which have been detailed by others [93Db] are not studied in this work). As is clearly evident in Fig. 4.2, nearly all of the Raman modes display complex fine-structure at low temperature. While the splittings in many cases are small, the narrow linewidths of the modes make the structure resolvable. $H_g(1)$, the lowest energy intramolecular phonon, is clearly a doublet in the high-temperature fcc phase, while in the low-temperature (< 260 K) orientationally ordered phase, it appears as a quartet. $H_g(1)$ is well separated in energy from the nearest silent mode [93Db, 94Yb], and difference scattering can be neglected at the lowest temperatures, thereby allowing all of these components to be attributed with certainty to $H_g(1)$.

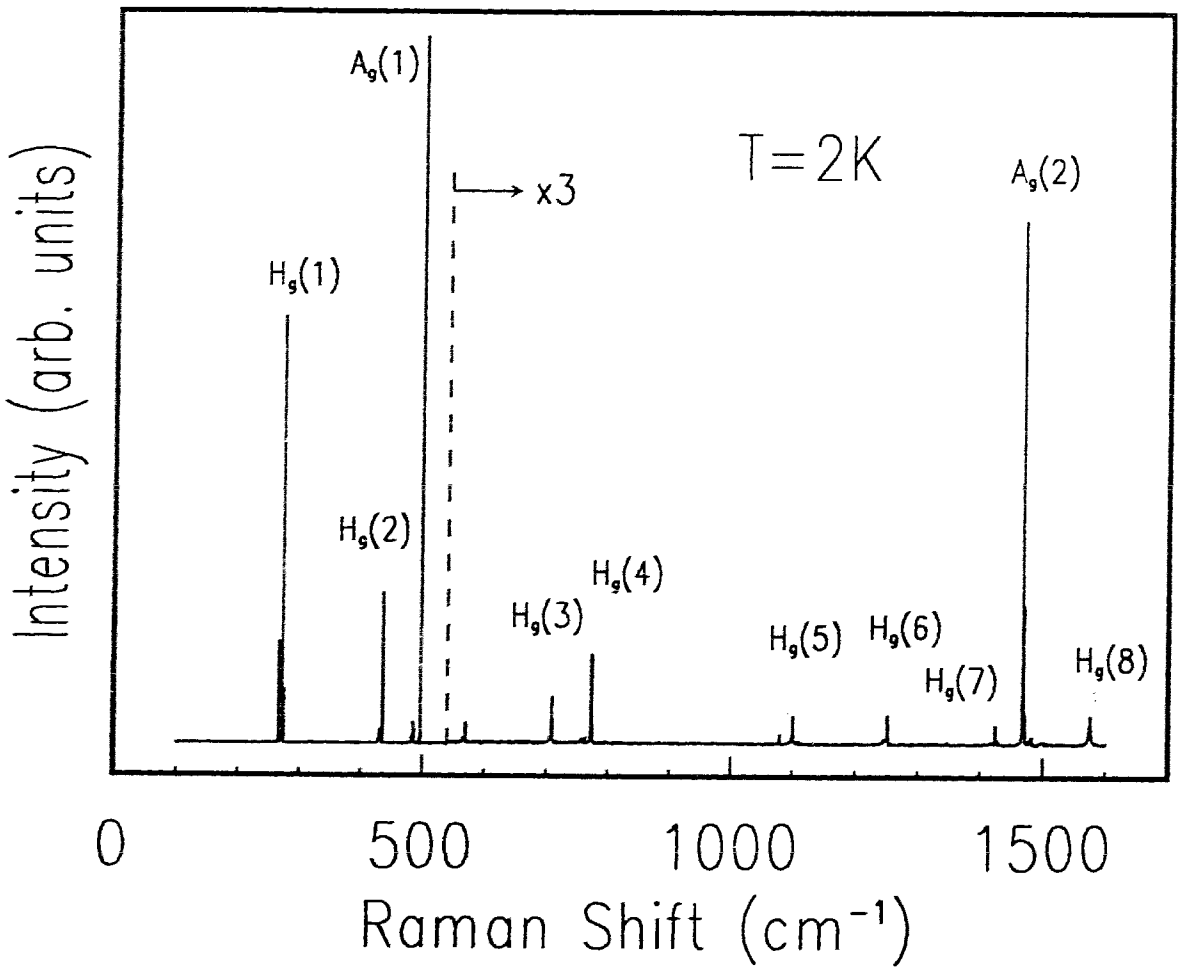

Fig. 4.1 Unpolarized Raman spectrum of crystalline C_{60} at 2 K (895 nm excitation and 0.1 cm^{-1} resolution). The higher energy portion of the spectrum (>600 cm^{-1} shift) has been scaled up in intensity by a factor of 3 for clarity. The mode labels are those of an isolated molecule (I_h symmetry).

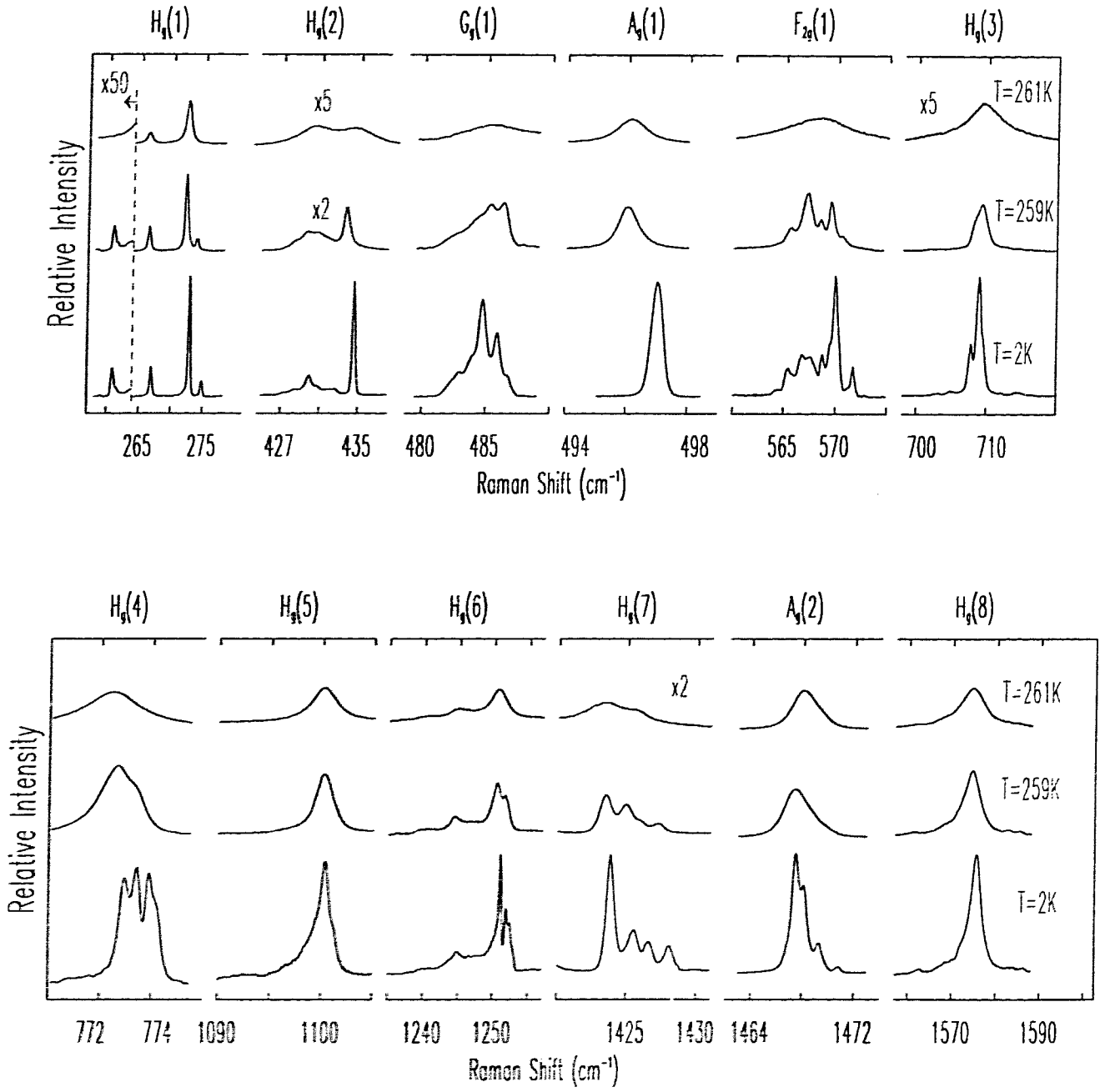

Fig. 4.2 The temperature evolution of the $H_g(1)$, $H_g(2)$, $G_g(1)$, $A_g(1)$, $F_{2g}(1)$, $H_g(3)$, $H_g(4)$, $H_g(5)$, $H_g(6)$, $H_g(7)$, $A_g(2)$, and $H_g(8)$ Raman components (from left to right) of crystalline C_{60}. The spectra within each subsection of the energy axis are plotted on the same scale, but shifted for clarity.

Next in Fig. 4.2 is shown the $H_g(2)$-derived band. As was the case with $H_g(1)$, $H_g(2)$ is well isolated in energy from neighbouring silent modes and possible overtones, and so all of the structure shown arises from splittings of the $H_g(2)$ mode. In the high-temperature (HT) phase, a doublet is resolvable. Upon cooling into the low-temperature (LT) ordered phase, the linewidths narrow considerably and the band becomes richly structured. The highest energy component of $H_g(2)$ possesses one of the narrowest linewidths seen in the entire phonon spectrum, measuring 0.10 cm^{-1} at 2 K.

Following the $H_g(2)$ band in Fig. 4.2 is seen a mode ascribed to $G_g(1)$ [93Db]. While this vibration is silent in the isolated molecule, it and all the gerade vibrations are symmetry allowed in the crystal state. In the HT phase, only a single broad band is observed, while in the LT phase, the integrated intensity increases, the linewidths narrow, and at least five components become resolvable. This behaviour is mirrored in the $F_{2g}(1)$ mode [93Db], seen in Fig. 4.2 centered at ~570 cm^{-1}. This silent mode also appears in the HT crystal as a single broad band, while many components are visible in the LT phase. None of the fine-structure present in either the $G_g(1)$ or $F_{2g}(1)$ bands corresponds to other nearby silent modes or overtone scattering, and so can be solely attributed to these two molecular modes.

In contrast to all of the phonon bands discussed so far, the $A_g(1)$-derived phonon at ~497 cm^{-1} is a single, unsplit peak in both the HT and LT phases. As can be seen in Fig. 4.2, $A_g(1)$ narrows and shifts to slightly higher energy as the temperature is lowered through the ordering transition, but no fine-structure develops.

The $H_g(3)$ mode, centered at ~710 cm^{-1}, and the $H_g(5)$ mode at ~1100 cm^{-1} both appear as a single broad band in the freely rotating HT phase, but upon cooling into the orientationally ordered LT phase, the linewidths narrow sufficiently to resolve small splittings of the main peaks. The assignment of all the observed structure centered at 710 cm^{-1} and 1100 cm^{-1} to $H_g(3)$ and $H_g(5)$ respectively is complicated by the presence of several sum modes within ~5 cm^{-1} of these two fundamentals [93Db, 93Wb, 94Yb]. For

instance, the weak feature below $H_g(3)$ at 706 cm^{-1} coincides in energy with $H_g(1)$ + $H_g(2)$, while its small integrated intensity relative to the main peak of $H_g(3)$ further suggests that it stems from an overtone mode.

The $H_g(4)$-derived phonon band, centered at ~774 cm^{-1} in Fig. 4.2, shows no structure beyond an asymmetric lineshape in the HT phase, but at low temperatures, four nearly equal intensity components are clearly present. $H_g(4)$ also has several nearby combination mode possibilities (the higher in energy one goes, the more likely this occurrence becomes). However, the four components seen in Fig. 4.2 all have a strong Raman signal and so can be attributed to $H_g(4)$, since combination mode scattering is expected to be much weaker than scattering from the allowed fundamental. The lower energy 'foot' at 771 cm^{-1} coincides in energy with $H_g(1)$ + $A_g(1)$, and so likely stems from this combination mode scattering.

Structure is visible both above and below the ordering transition for the $H_g(6)$ and $H_g(7)$ bands, centered at 1250 and 1425 cm^{-1}, respectively. At low temperature, $H_g(7)$ consists of a fundamental peak with three distinct, higher energy components, while $H_g(6)$ displays a complex combination of several sharp components and broad, unresolved background scattering. Like $H_g(7)$, the second A_g mode at ~1468 cm^{-1} also displays a series of resolved components at low temperature, but only an asymmetry in the lin shape remains in the HT phase.

Finally, the highest energy first-order phonon, $H_g(8)$, is also the intrinsically broadest band. Even at the lowest temperatures, no sharp fine-structure is visible, although the asymmetry of the band does suggest an unresolved splitting. As the temperature is raised, the mode softens, and as was the case for all the Raman modes, the integrated intensity decreases.

The first inclination one has when faced with the splittings depicted in Fig. 4.2 is to assign them to crystal-field splittings of the otherwise degenerate molecular modes. The sparseness of the vibrational spectrum of a free molecule stems from the I_h symmetry

of the molecule, a symmetry which is not preserved in any crystal structure. The factor-group analysis for both the high-temperature fcc structure and the low-temperature sc crystal has been previously reported [92Dc], and is reproduced in Table 4.1. As can be seen from Table 4.1, a low-temperature splitting of all the Raman-active phonons is expected, and so superficially, the results presented in Fig. 4.2 are not surprising.

A group-theoretical study of the crystal-field splittings will supply the minimum degeneracies of the phonon bands required by symmetry (see Table 4.1), but naturally cannot supply the magnitudes of the band splittings; for such one needs to actually calculate the phonon spectrum beginning with a model potential. Only one theoretical calculation of the phonon band structure of solid C_{60} has been reported to date [94Yb]. In it, substantial bandwidths were predicted for all of the intramolecular phonons below ~600 cm^{-1}, and virtually no dispersion for the higher energy modes. This appears to be at odds with the experimental data shown in Fig. 4.2, in which the higher energy phonons are also seen to be richly structured.

To identify the symmetry of the fine-structure components, a polarized Raman scattering study was undertaken, as was done with the libron modes (see Section 3.6). The Raman scattering selection rules associated with the low-temperature phase are listed in Table 4.2, where the setting angle ϕ refers the angle of the incident light polarization relative to a <001> crystal direction while $||$ and $\perp$ refer to the orientation of the scattered light polarization relative to the incident polarization. Polarized Raman scattering from the low-energy phonons (< 600 cm^{-1}) is shown in Figure 4.3, while the higher energy modes are shown in Figure 4.4. The data presented in Figs. 4.3 and 4.4 were collected using 794.98 nm excitation, a wavelength to which the sample is transparent. A polished sample was therefore used to reduce the amount of diffusely scattered light which was collected, as discussed in Section 3.6. The depolarization ratios ($I_\perp / I_{||}$) of the A_g modes shown in Figs. 4.3 and 4.4 have been measured using visible excitation [93M], and are reported to be an order of magnitude smaller than what is found

Table 4.1. Correlation table of the gerade modes of C_{60} for the low temperature phase of solid C_{60}. Only the ten H_g and two A_g modes are Raman-active in the isolated molecule, while all gerade modes are allowed by symmetry in the solid phase (LT and HT) (Ref. 3).

Molecule	HT phase (fcc)	LT phase (sc)
I_h	T_h^3	T_h^6
$2A_g$	$2A_g$	$2A_g + 2F_g$
$3F_{1g}$	$3F_g$	$3A_g + 3E_g + 9F_g$
$4F_{2g}$	$4F_g$	$4A_g + 4E_g + 12F_g$
$6G_g$	$6A_g + 6F_g$	$12A_g + 6E_g + 24F_g$
$8H_g$	$8E_g + 8F_g$	$8A_g + 16E_g + 40F_g$

Table 4.2. Raman-active modes of solid C_{60} under various scattering geometries. The setting angle ϕ refers to the angle of the incident light polarization relative to the [001] crystal direction while $||$ and $\perp$ refer to the relative orientation of the incident and scattered light polarization.

setting angle ϕ	analyzer	backscattering from {100} face
0°	$\|\|$	$A_g + E_g$
	$\perp$	F_g
45°	$\|\|$	$A_g + E_g + F_g$
	$\perp$	E_g

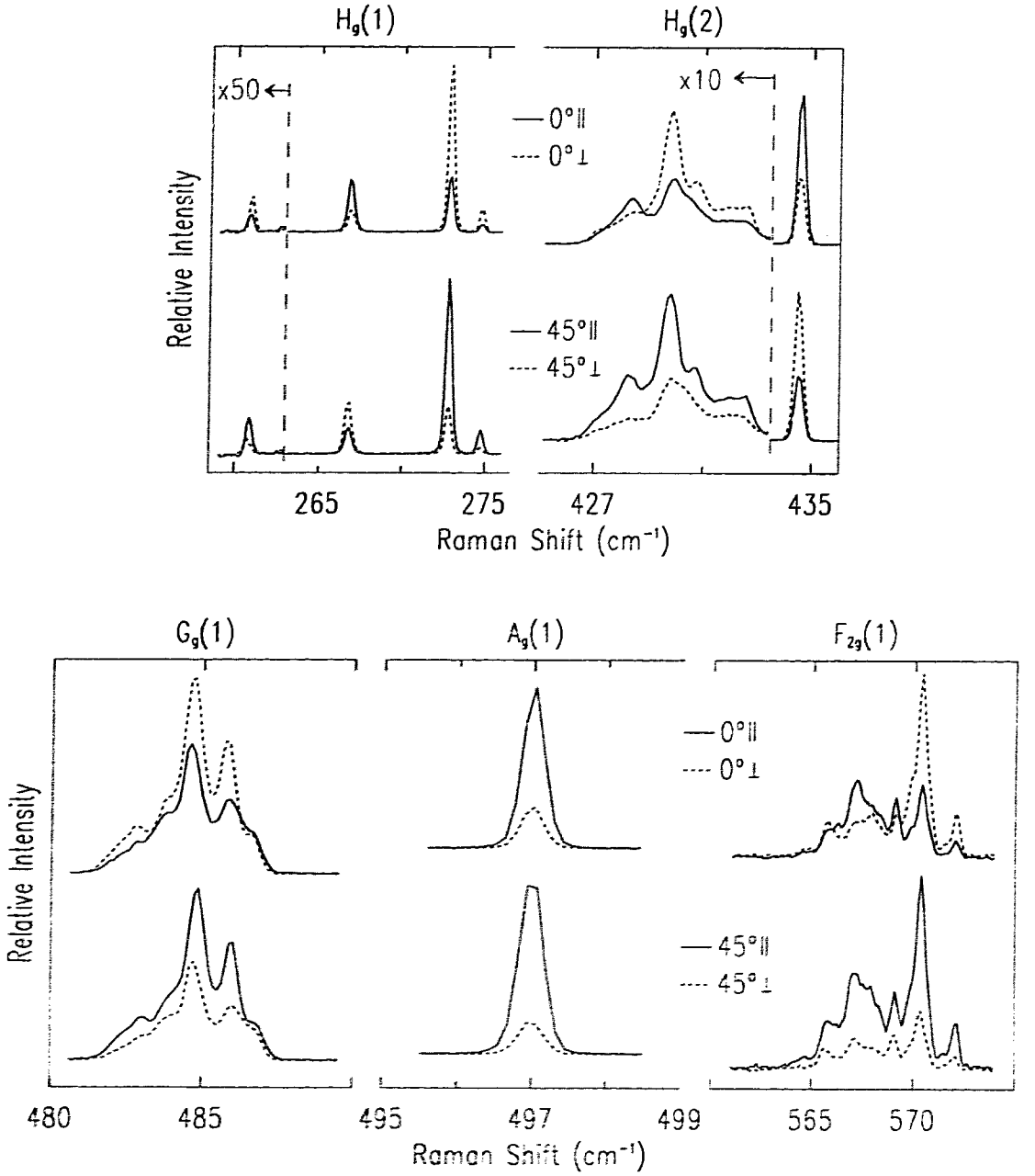

Fig. 4.3 Polarization dependence of the $H_g(1)$, $H_g(2)$, $G_g(1)$, $A_g(1)$, and $F_{2g}(1)$ modes of crystalline C_{60}; T=2 K. The measurements were made from a {100} face of the crystal in a backscattering geometry. 0° and 45° refer to the angle of the laser polarization to the [001] direction, while parallel and perpendicular refer to the relative orientation of the incident and scattered light polarizations.

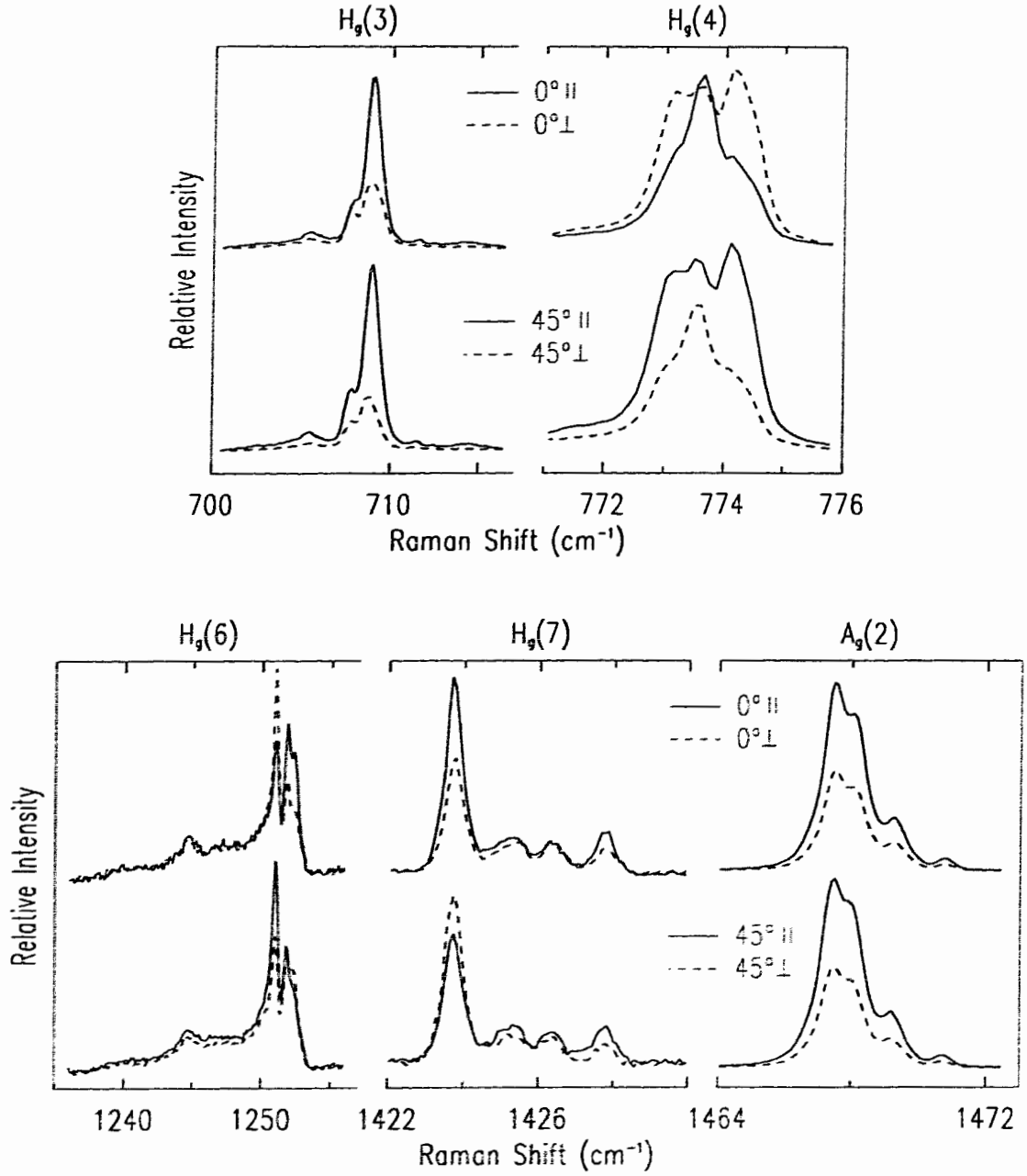

Fig. 4.4 Polarization dependence of the $H_g(3)$, $H_g(4)$, $H_g(6)$, $H_g(7)$, and $A_g(2)$ modes of crystalline C_{60}; T=2 K. The measurements were made from a {100} face of the crystal in a backscattering geometry. 0° and 45° refer to the angle of the laser polarization to the [001] direction, while parallel and perpendicular refer to the relative orientation of the incident and scattered light polarizations.

here ($I_{\perp} / I_{||} \cong 0.25$ for both $A_g(1)$ and $A_g(2)$ in this study). Therefore, the rejection of diffusely scattered light was not complete during these polarization measurements and the depolarization ratios depicted in Figs. 4.3 and 4.4 are not the true values. However, the trends indicated are clear, and the goal is to identify the symmetries of the fine-structure components, not to measure the absolute depolarization ratios of the modes.

With the selection rules listed in Table 4.2, one can proceed through the data shown in Figs. 4.3 and 4.4 and apply group-theory labels to the various fine-structure components. For example, the four components of $H_g(1)$ are clearly F_g, E_g, F_g, and F_g, in order of increasing energy. As one continues through the phonon spectrum, however, a number of glaring discrepancies arise. There are several components which show virtually no polarization dependence at all, such as the background scattering within the $H_g(6)$ band, and the weaker components of the $H_g(7)$ band. Also, more than a single fine-structure component with A_g symmetry is seen in the $F_{2g}(1)$ band, the $H_g(3)$ band, and most obviously the $A_g(2)$-derived band. This is in contradiction to the splittings expected from group-theory, as summarized in Table 4.2. Degeneracies beyond what are required from a symmetry standpoint, so-called accidental degeneracies, can, and often do, occur; such an example is the $A_g(1)$ mode which shows no splitting whatsoever in the low-temperature phase. Splittings above those predicted by group-theory are rigorously excluded. Thus, the observation of an $A_g(2)$ band which has at least five components, all of which have A_g symmetry, unequivocally proves that the splittings cannot be attributed to the $Pa\bar{3}$ crystal-field of the low-temperature phase. One must therefore search for additional perturbations within the solid phase to account for the vibrational fine-structure. Perhaps the most obvious deviation from the perfectly ordered crystal structure assumed in the factor-group analysis encapsulated in Table 4.2 is isotopic disorder, arising from a natural abundance of ^{13}C within the crystal. The influence of isotopic disorder on the phonon spectrum is the subject of Section 4.3.

4.3 Intramolecular Phonons in Isotopically Engineered Crystals

The 1.1% natural abundance of ^{13}C presents a conspicuous form of disorder within crystalline C_{60}. Nearly half of all the C_{60} molecules within the solid will contain at least one ^{13}C atom, which represents a tremendous reduction in the symmetry of the structure, and while a mass shift of one part in 720 is a small perturbation, it may nonetheless lead to measurable fine-structure given the large energy range of the phonon spectrum.

It was shown by Guha *et al* [94G] that the $A_g(2)$ mode of isolated C_{60} molecules made from natural carbon (a frozen solution of C_{60} in CS_2) displayed splittings reflective of the mass spectrum of the molecules. Using qualitative arguments within the framework of perturbation theory, it is straightforward to show that the presence of x ^{13}C atoms within a C_{60} molecule should shift the vibrational frequencies by a factor of $(1 + x/720)^{-0.5}$ [93N, 94G]. Guha *et al.* observed three fine-structure components, each separated by ~ 1 cm^{-1}, which agrees well with the expected energy shift of $^{12}C_{60}$, $^{13}C^{12}C_{59}$, and $^{13}C_2{}^{12}C_{58}$ vibrations.

In a 'conventional' crystal, such as diamond, the phonons sample a large number of unit cells, leading to a linear averaging of the isotopic masses present in the crystal [91Hc]. In such a case, the isotopic disorder of the crystal does not lead to additional splittings but simply produces a shift of the phonon frequencies by $m^{-\frac{1}{2}}$, where m is the average atomic mass. A broadening of the phonon linewidths due to the mass fluctuations is also usually seen [91Hc]. In crystalline C_{60}, one may anticipate a more complicated dependence of the phonon bands upon the isotopic content, given the molecular nature of the solid, and the observation of isotope splittings in isolated C_{60}.

To eliminate the influence of isotopic disorder within the intramolecular phonon spectrum, C_{60} single crystals with an enriched isotopic purity were fabricated and studied. Using 99.95% ^{12}C starting material, the $^{12}C_{60}$ purity was increased from 51.9% (natural abundance) to 99.7%. Isotopically enriched $^{13}C_{60}$ crystals were also made; a starting

purity of 99.7% ^{13}C produced crystals which were 85% pure $^{13}C_{60}$. The 99.7% $^{12}C_{60}$ crystals and 85% $^{13}C_{60}$ crystals will be herein referred to as 'crystalline $^{12}C_{60}$' and 'crystalline $^{13}C_{60}$', respectively.

In Figure 4.5, subsets of the low-temperature Raman spectrum of crystalline $^{12}C_{60}$, $^{13}C_{60}$, and natural C_{60} are shown. The natural C_{60} and $^{12}C_{60}$ spectra are shown on the same energy scale, while the $^{13}C_{60}$ spectra have been scaled up in energy by the factor $\left(\frac{13}{12}\right)^{\frac{1}{2}}$ to facilitate comparison. All of the modes shown in Fig. 4.5 display narrower linewidths in the isotopically purified materials as compared to natural C_{60}, but none of the fine-structure is absent. The random substitutions of ^{13}C for ^{12}C present in natural C_{60} are thus not responsible for the splittings seen in these modes. A line broadening due to random isotopic substitutions present in natural C_{60} is evident in all the modes shown in Fig. 4.5, most notably for $H_g(6)$, where additional components can be resolved in the $^{12}C_{60}$ and $^{13}C_{60}$ spectra, and the broad background scattering is reduced.

Linewidth broadening arising from isotopic disorder does not occur in all of the intramolecular phonon bands. Shown in Figure 4.6 are several modes which display little or no broadening in natural C_{60} relative to the isotopically purified samples. The $^{13}C_{60}$ spectra shown in Fig. 4.6 have been scaled up in energy by the factor $\left(\frac{13}{12}\right)^{\frac{1}{2}}$ as was done in Fig. 4.5. Immediately obvious from Fig. 4.6 is the fact that the phonon fine-structure is unchanged from natural C_{60} to the isotopically purified $^{12}C_{60}$ and $^{13}C_{60}$. Thus, as was the case for the phonon bands shown in Fig. 4.5, none of the fine-structure seen in these modes arises from isotopic disorder.

Isotopic disorder does lead to activation of additional fine-structure, rather than simply shifting components, in two intramolecular modes: $F_{2g}(1)$ and $A_g(2)$, shown in Figure 4.7. While $F_{2g}(1)$ is a complex band in both natural C_{60} and the isotopically purified $^{12}C_{60}$ sample, the component at 569.39 cm^{-1} is clearly present in only natural C_{60} crystals. The isotope dependence of the $A_g(2)$-derived band is the most pronounced

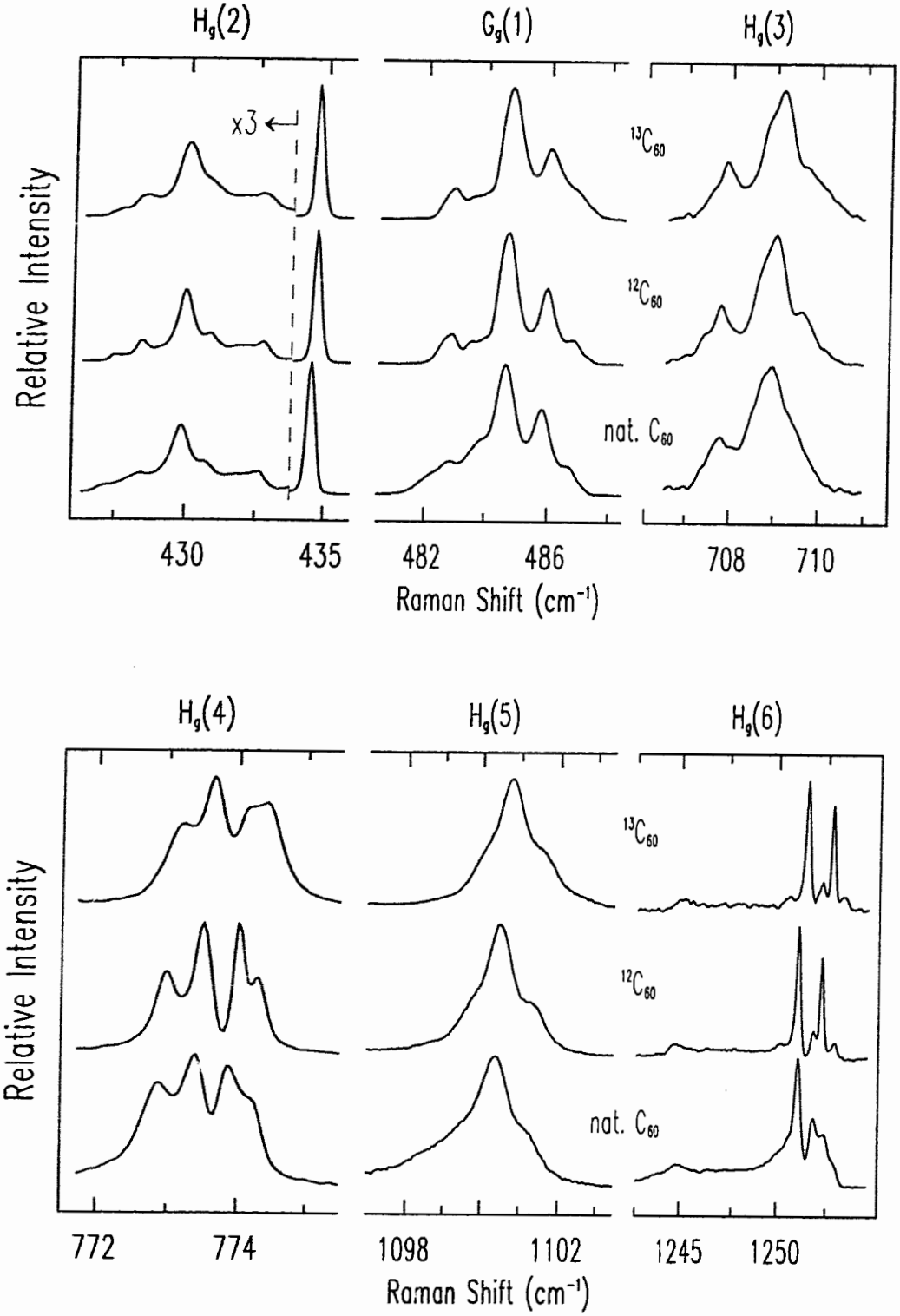

Fig. 4.5 $H_g(2)$, $G_g(1)$, $H_g(3)$, $H_g(4)$, $H_g(5)$, and $H_g(6)$ fine-structure of crystalline C_{60} made from naturally abundant carbon, 99.95% ^{12}C, and 99.7% ^{13}C; T=2 K. The $^{13}C_{60}$ spectra have been scaled up in energy by the factor $\left(\frac{13}{12}\right)^{0.5}$ to facilitate comparison.

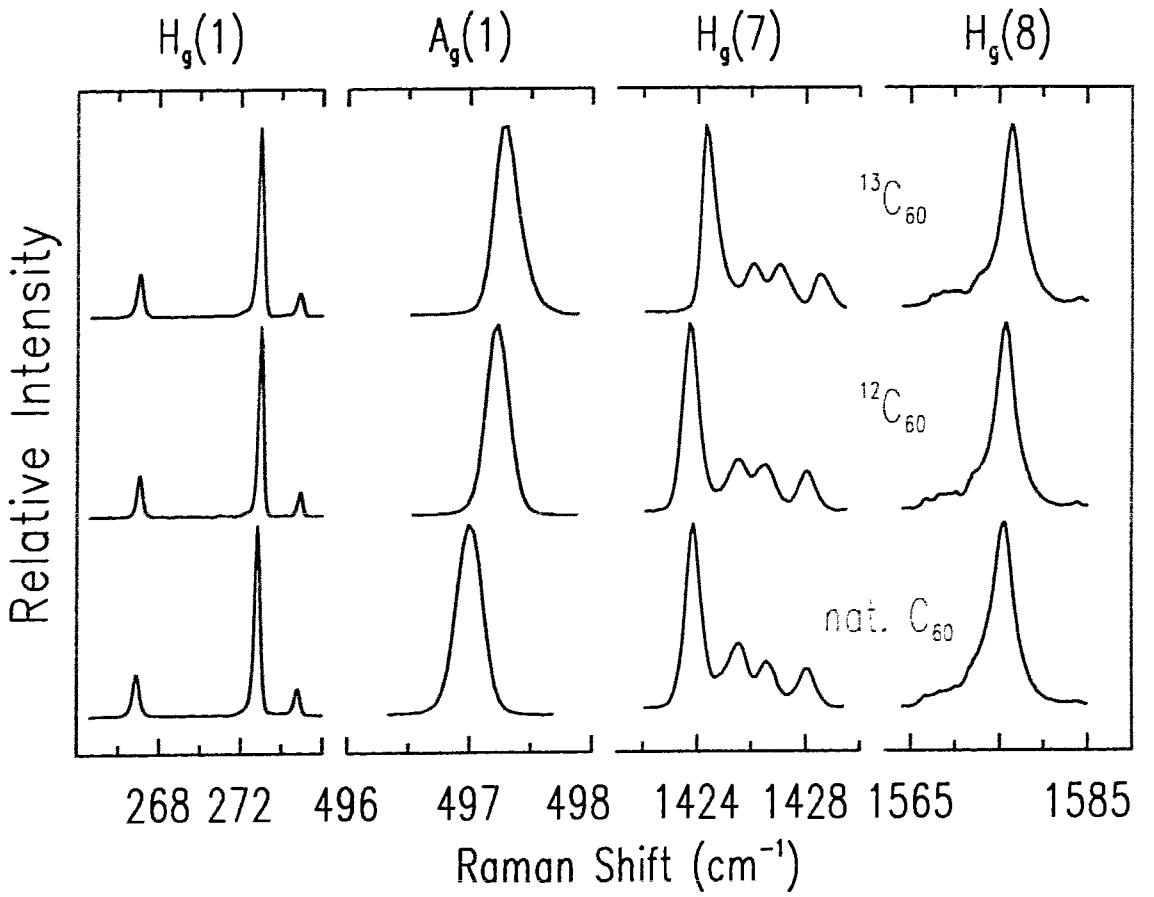

Fig. 4.6 $H_g(1)$, $A_g(1)$, $H_g(7)$, and $H_g(8)$ fine-structure of crystalline C_{60} made from naturally abundant carbon, 99.95% ^{12}C, and 99.7% ^{13}C; T=2 K. The $^{13}C_{60}$ spectra have been scaled up in energy by the factor $\left(\frac{13}{12}\right)^{0.5}$ to facilitate comparison.

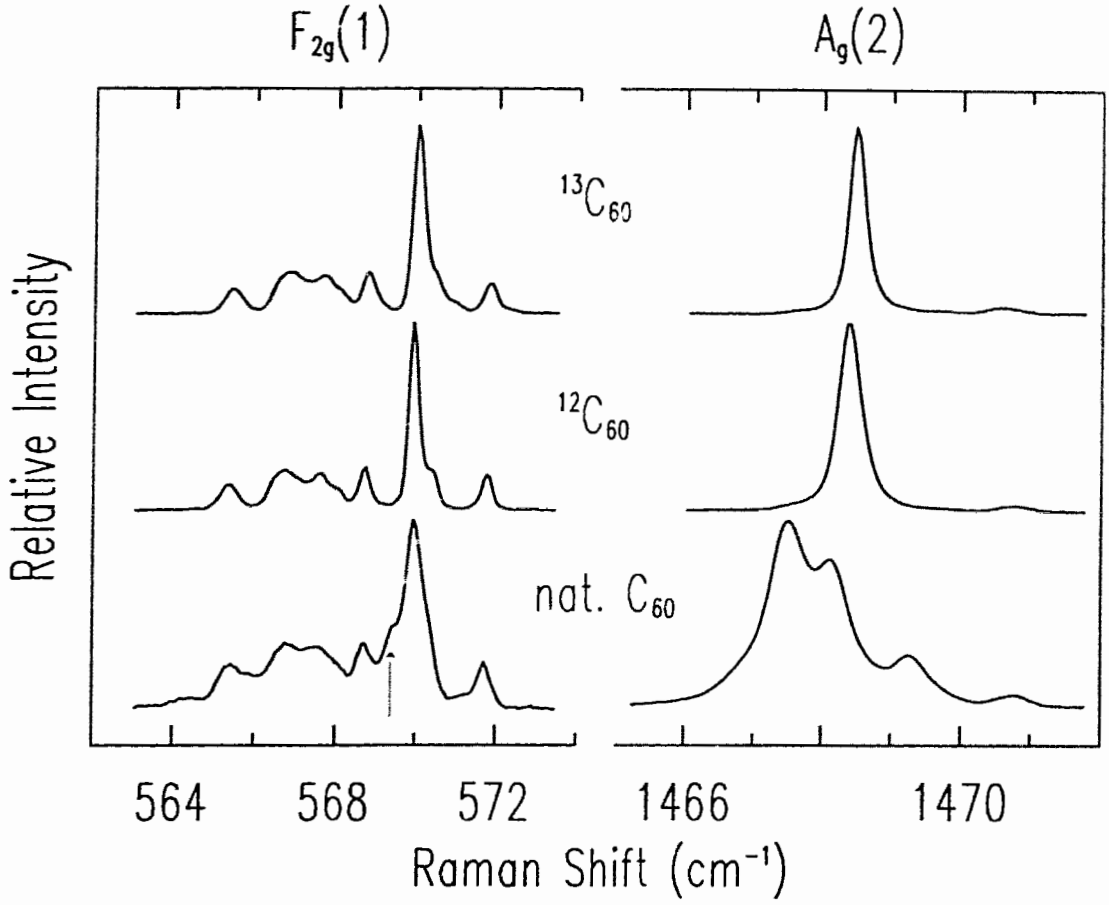

Fig. 4.7 $F_{2g}(1)$ and $A_g(2)$ fine-structure of crystalline C_{60} made from naturally abundant carbon, 99.95% ^{12}C, and 99.7% ^{13}C; T=2 K. The $^{13}C_{60}$ spectra have been scaled up in energy by the factor $\left(\frac{13}{12}\right)^{0.5}$ to facilitate comparison. The $F_{2g}(1)$ and $A_g(2)$ modes are the only two phonons in the first-order Raman spectrum which display additional splittings due to isotopic disorder.

of all the Raman bands. In natural C_{60}, $A_g(2)$ has at least five components at 1466.9, 1467.6, 1468.2, 1469.4, and 1470.8 cm^{-1}, while in crystalline $^{12}C_{60}$, only peaks at 1468.6 and 1470.8 cm^{-1} are visible. Thus the $A_g(2)$ band appears more molecular in nature than the other C_{60} phonons, in that the isotopic disorder is not averaged over. The fine-structure displayed in Fig. 4.7 cannot, however, be understood within a purely molecular description of the vibrational mode. Over 50% of the molecules present in natural C_{60} are $^{12}C_{60}$, but none of the $A_g(2)$ components seen in natural crystalline C_{60} are degenerate with the strongest peak in crystalline $^{12}C_{60}$.

The failure of the main crystalline $^{12}C_{60}$ peak to superimpose onto any of the natural crystalline C_{60} peaks is not an artifact, and must result from an interplay of isotopic and solid state effects. The situation is made even more clear by comparing the crystalline C_{60} spectra with the spectra of the same materials dissolved in frozen CS_2, shown in Figure 4.8. In Fig. 4.8, cC_{60} refers to the Raman spectra of C_{60} single crystals, while C_{60}/CS_2 refers to the frozen solution of C_{60}. The C_{60} in CS_2 spectrum can be understood on the basis of a superposition of vibrational modes of the various molecular masses present in natural C_{60} [94G, 95Hc]. This interpretation is confirmed by comparing the spectrum of natural C_{60} in CS_2 to the spectrum of $^{12}C_{60}$ in CS_2. The frozen solution of $^{12}C_{60}$ produces the expected spectrum of a single component at precisely the energy of the highest-energy peak of the frozen solution of natural C_{60}. As can be seen in Fig. 4.8, however, there is absolutely no resemblance between the $A_g(2)$ spectrum of natural crystalline C_{60} and natural C_{60} in CS_2. This again emphasizes the fact that in crystalline C_{60}, the isotopic effects are somehow strongly coupled to band structure effects for the $A_g(2)$-derived phonon.

The range of responses of the intramolecular phonons to isotopic disorder can be qualitatively understood by expressing the relative mass fluctuations as a frequency bandwidth, $\left(\Delta m/\bar{m}\right)\omega_o$, and comparing it to the bandwidth, $\Delta\omega_o$, of the intramolecular phonons, where ω_o is the mean phonon frequency. If the mass fluctuation bandwidth is

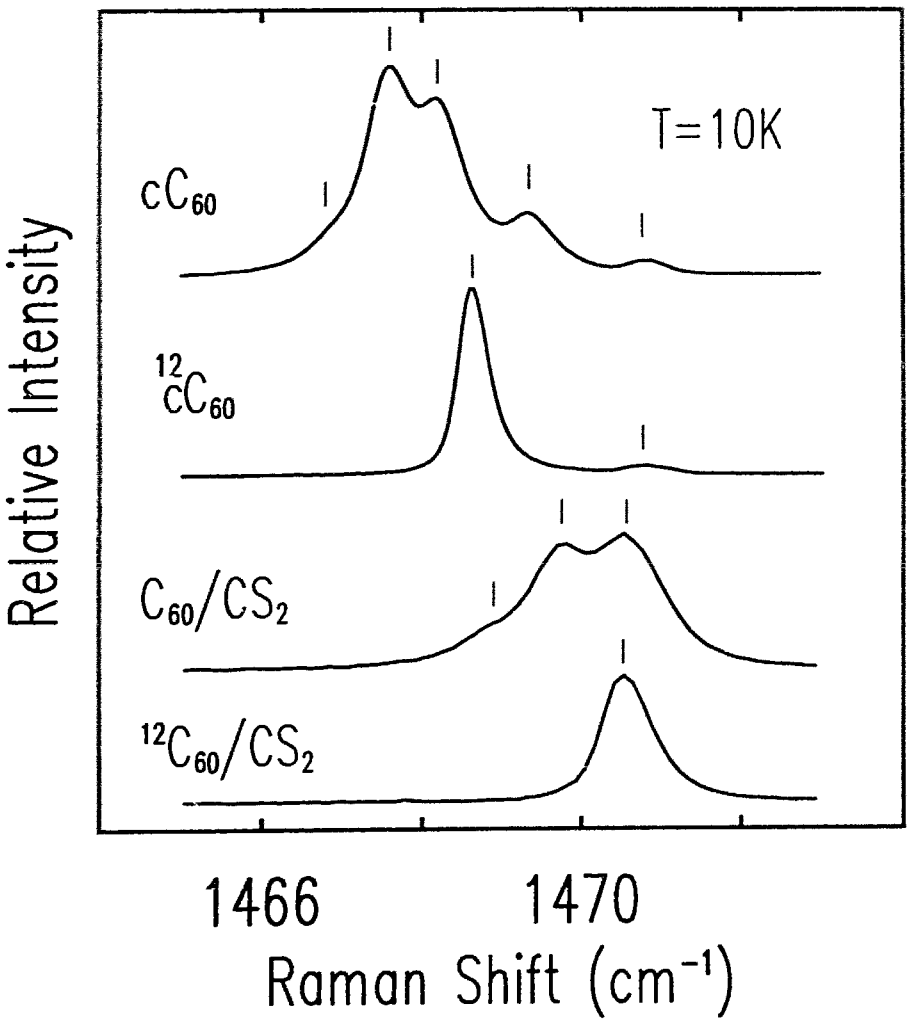

Fig. 4.8 Raman spectrum of the $A_g(2)$ mode of C_{60} single crystals (cC_{60}), C_{60} single crystals made from 99.95% ^{12}C ($c^{12}C_{60}$), natural C_{60} dissolved in CS_2 (C_{60}/CS_2), and 99.95% ^{12}C C_{60} dissolved in CS_2 ($^{12}C_{60}/CS_2$).

much smaller than the intrinsic phonon bandwidth, one would anticipate a simple linear averaging of the isotope masses to result, as is seen in 'conventional' crystals such as diamond [91Hc] or germanium [91Fc]. A more complicated behaviour could be expected when the mass fluctuation bandwidth becomes comparable in magnitude to the intrinsic phonon bandwidth. For the lower-energy intramolecular phonons, significant band dispersions (large bandwidths) have been predicted [94Yc] while the mass-fluctuation bandwidth is smallest, and so one would expect little response from these modes to increasing ^{13}C content beyond a uniform softening. The 0.11 cm^{-1} shift of $H_g(1)$, 0.15 cm^{-1} shift of $H_g(2)$, and 0.20 cm^{-1} shift of $A_g(1)$ observed between natural crystalline C_{60} and crystalline $^{12}C_{60}$ are, in fact, exactly the shifts predicted from a $\bar{m}^{-0.5}$ dependence of the phonon frequencies, where $\bar{m}$ is the average isotope mass. Conversely, the $A_g(2)$ mode is predicted to have a negligibly small phonon bandwidth [94Yc], while the isotopic-disorder bandwidth, which scales with the mode frequency, is significantly larger than it was for the lower-energy phonons. A complicated relationship between solid-state and isotope effects is therefore seen within the $A_g(2)$-derived phonon.
The energies of all the Raman modes discussed in this and the preceding section are summarized in Table 4.3.

To further explore the complex dependence of the $A_g(2)$ phonon on the isotopic composition of the crystal, additional samples with varying mass compositions have been fabricated and studied. Shown in Figure 4.9 are the mass spectra of the isotopically engineered crystals used in this study. As can be seen from Fig. 4.9, natural C_{60} contains significant concentrations of $^{13}C^{12}C_{60}$ and $^{13}C_2{}^{12}C_{58}$. By using a starting ^{13}C concentration of 0.5%, roughly half that of natural material (1.1% ^{13}C), C_{60} molecules with one and two ^{13}C atoms are still produced, but in reduced concentrations. This then provides a convenient isotopic composition between natural C_{60} and the 'pure' $^{12}C_{60}$ material. By increasing the ^{13}C concentration to 7.3%, the number of different molecular

Table 4.3. Intramolecular mode energies

265 K (fcc) natural C_{60}	2 K (sc) natural C_{60}	2 K $^{12}C_{60}$	2 K $^{13}C_{60}$	assignment
	260.96	260.13	251.03	
266.2	266.87	266.98	256.61	
272.4	272.83	272.94	262.31	$H_g(1)$
	274.76	274.89	264.17	
	427.19	427.66	410.88	
	428.32	428.40	411.80	
	429.82	429.96	413.24	
430.3	430.72	430.88	414.11	$H_g(2)$
	431.61	431.90	415.15	
	432.59	432.77	415.95	
434.3	434.54	434.69	417.84	
	482.79	482.79	464.10	
	483.79	483.59	465.17	
485.4	484.67	484.69	465.86	$G_g(1)$
	485.80	485.91	467.11	
	486.67	486.77	467.94	
496.1	497.00	497.22	477.89	$A_g(1)$
	565.52	565.35	543.35	
	566.73	566.71	544.69	
567.8	567.52	567.58	545.42	
	568.77	568.71	546.60	$F_{2g}(1)$
	569.39	-	-	
	569.94	569.92	547.75	
	570.36	570.34	548.20	
	571.70	571.75	549.51	
	707.46	707.40	679.95	
	707.81	707.79	680.28	
709.4	708.58	708.69	681.19	$H_g(3)$
	709.01	709.09	681.48	
	709.57	709.63	682.04	
	772.88	772.99	743.04	
772.4	773.41	773.50	743.46	$H_g(4)$
	773.87	774.01	743.96	
	774.23	774.30	744.19	

	-	1099.70	1057.33	
1100.0	1100.36	1100.50	1057.89	$H_g(5)$
	1101.38	1101.37	1058.67	
	1244.84	1244.85	1196.48	
1244.9	-	1250.18	1201.79	
	1251.08	1251.07	1202.65	$H_g(6)$
1250.5	1251.86	1251.86	1203.39	
	1252.41	1252.27	1203.88	
	1252.88	1252.86	1204.45	
	1423.80	1423.72	1368.82	
1423.4	1425.52	1425.51	1370.39	$H_g(7)$
	1426.57	1426.49	1371.48	
1425.5	1427.90	1427.92	1372.84	
	1466.9	-		
	1467.6	-		
1468.1	1468.8	1468.6	1412.00	$A_g(2)$
	1469.4	-		
	1470.8	1470.8	1414.00	
	1572.22	1572.32	1511.80	$H_g(8)$
1574.5	1575.51	1575.68	1514.95	

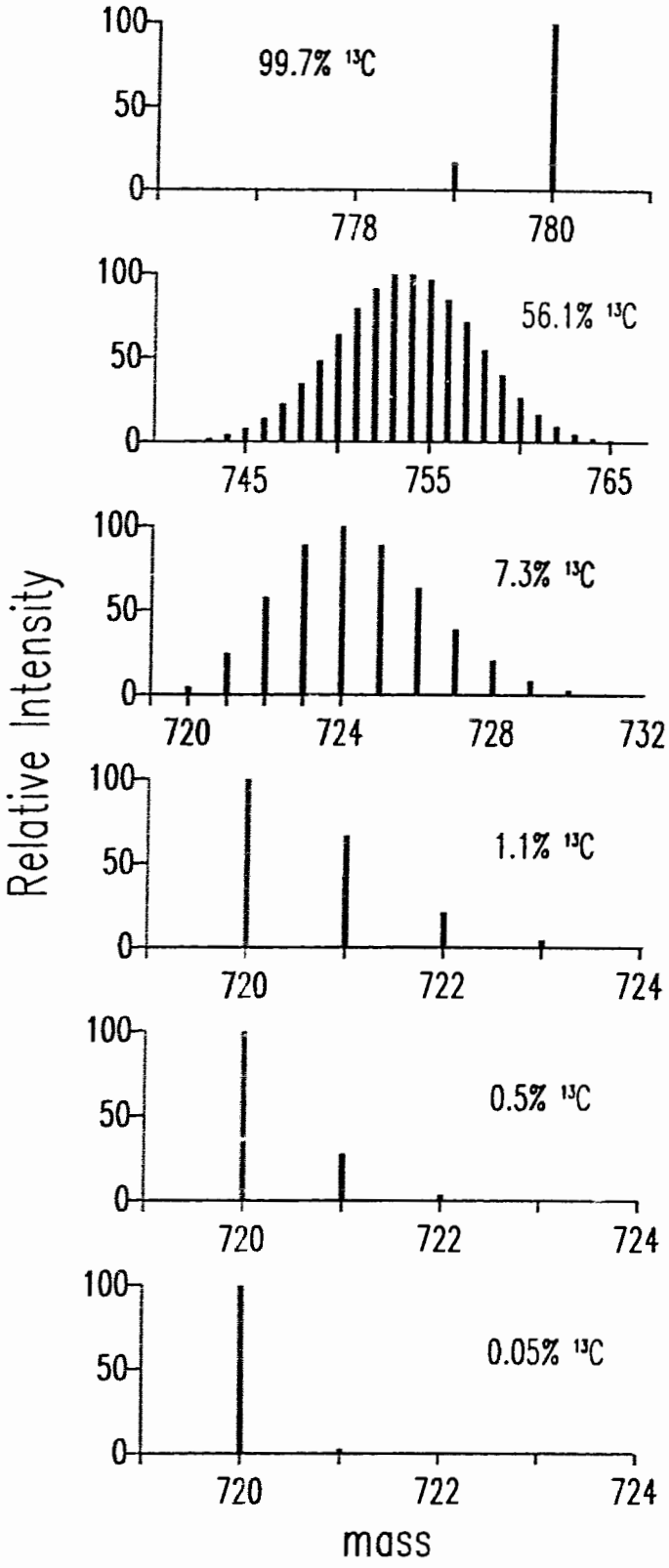

Fig. 4.9 Measured mass abundances of C_{60} crystals made from isotopically enriched graphite rods.

masses present is greatly increased, and the most abundant species is no longer the pure $^{12}C_{60}$ molecule. At 56.1% ^{13}C concentration, the isotopic disorder of the crystal is nearly maximized, both in the number of different molecular masses present, and in the number of possible isomers with a fixed molecular mass.

The $A_g(2)$ band of crystalline C_{60} as a function of isotopic composition is shown in Figure 4.10. While the mass spectrum of the 0.5% ^{13}C crystal depicts only a small departure from that of natural C_{60} crystals, substantial changes have occurred within $A_g(2)$. Only four components are visible in the 0.5% ^{13}C material, at 1467.7, 1468.1, 1469.0, and 1470.8 cm^{-1}. The highest energy component at 1470.8 cm^{-1} is clearly unchanged as the ^{13}C content is increased from the pure $^{12}C_{60}$ crystal to natural C_{60}; the correlation between the remaining components is somewhat ambiguous, however. One possibility has the four remaining components of natural crystalline C_{60} collapsing from both higher and lower energy to the single, intense peak seen in crystalline $^{12}C_{60}$ at 1468.6 cm^{-1}. Alternatively, the main peak of crystalline $^{12}C_{60}$ may be softening with increasing ^{13}C content according to an average atomic mass dependence as other modes such as $A_g(1)$ are seen to do, with the addition of further splittings occurring, induced by the isotopic disorder. The energy of the most intense $A_g(2)$ component of each isotopically engineered sample does in fact follow a $m^{-\frac{1}{2}}$ dependence, including the centroid of the 7.3% ^{13}C $A_g(2)$ band, which, as can be seen in Fig. 4.10, is considerably broader than in natural C_{60}, although a ladder of higher energy components is still resolvable. The 56.1% ^{13}C $A_g(2)$ band, shown in the inset of Fig. 4.10, displays a large broadening from that of natural C_{60}, and no fine-structure remains.

It is clear that an explanation of the dependence of the $A_g(2)$-derived phonon on the isotope composition of the crystal will require an interplay between isotopic and solid state effects which is presently not well-understood. Several theoretical studies of the impact of isotopic disorder on the molecular vibrations of C_{60} have been undertaken, with the prediction of energy shifts and splittings of the vibrational modes with increasing

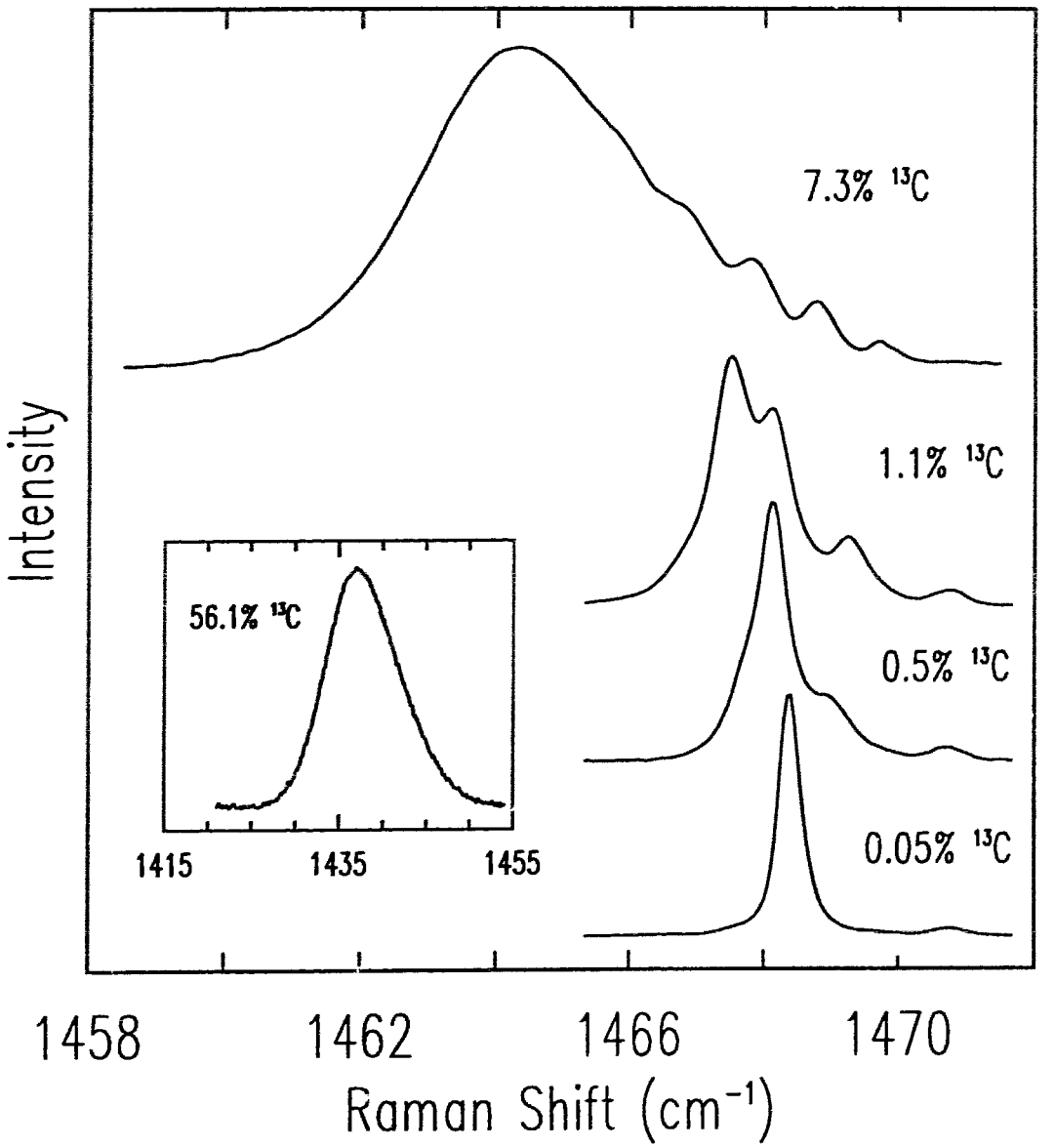

Fig. 4.10 $A_g(2)$-derived phonon band of crystalline C_{60} as a function of isotope content; T=2 K.

disorder [92W, 93N]. A strictly molecular treatment cannot, however, account for the shifting of the strongest crystalline $^{12}C_{60}$ component which occurs as mass substitutions are made in a fraction of the molecules of the solid. Conversely, a 'virtual crystal approximation', in which the solid is modeled by a crystal made up of identical atoms of average mass $\bar{m}$ cannot account for the splittings which occur with increasing ^{13}C content, or the softening of some components but not others within the same band.

In contrast to the complex behaviour of the $A_g(2)$ band, several of the lower energy intramolecular modes are well described within a 'virtual crystal approximation'. Shown in Figure 4.11 are the $H_g(1)$ and $A_g(1)$ bands for the isotopically engineered crystals described in the preceding paragraphs. As the ^{13}C concentration is increased, the phonons merely soften in energy by $m^{-\frac{1}{2}}$, where m is the average isotope mass. The increasing isotopic disorder in the higher ^{13}C concentration crystals does lead to increased linewidths, with a pronounced lower energy asymmetry appearing in the 56.1% ^{13}C crystals.

It has been seen in this Section that apart from $F_{2g}(1)$ and particularly $A_g(2)$, all of the splittings displayed in Fig. 4.2 do not arise from the isotopic disorder of natural C_{60} crystals. But as was previously discussed within the context of the intermolecular modes, additional disorder is present in the low-temperature phase in the form of orientational defects. The influence of the seemingly unavoidable inclusion of misoriented molecules on the Raman fine-structure is explored in the next Section.

4.4 The Impact of Merohedral Disorder

The crystal field of the low-temperature phase of C_{60} consists of both the influence of an ordered solid (translationally and orientationally), and the random perturbations associated with a not-necessarily small fraction of misoriented molecules. Generally, merohedral disorder has not been considered in theoretical or experimental studies of the vibrational dynamics of C_{60}, both because high-resolution experimental

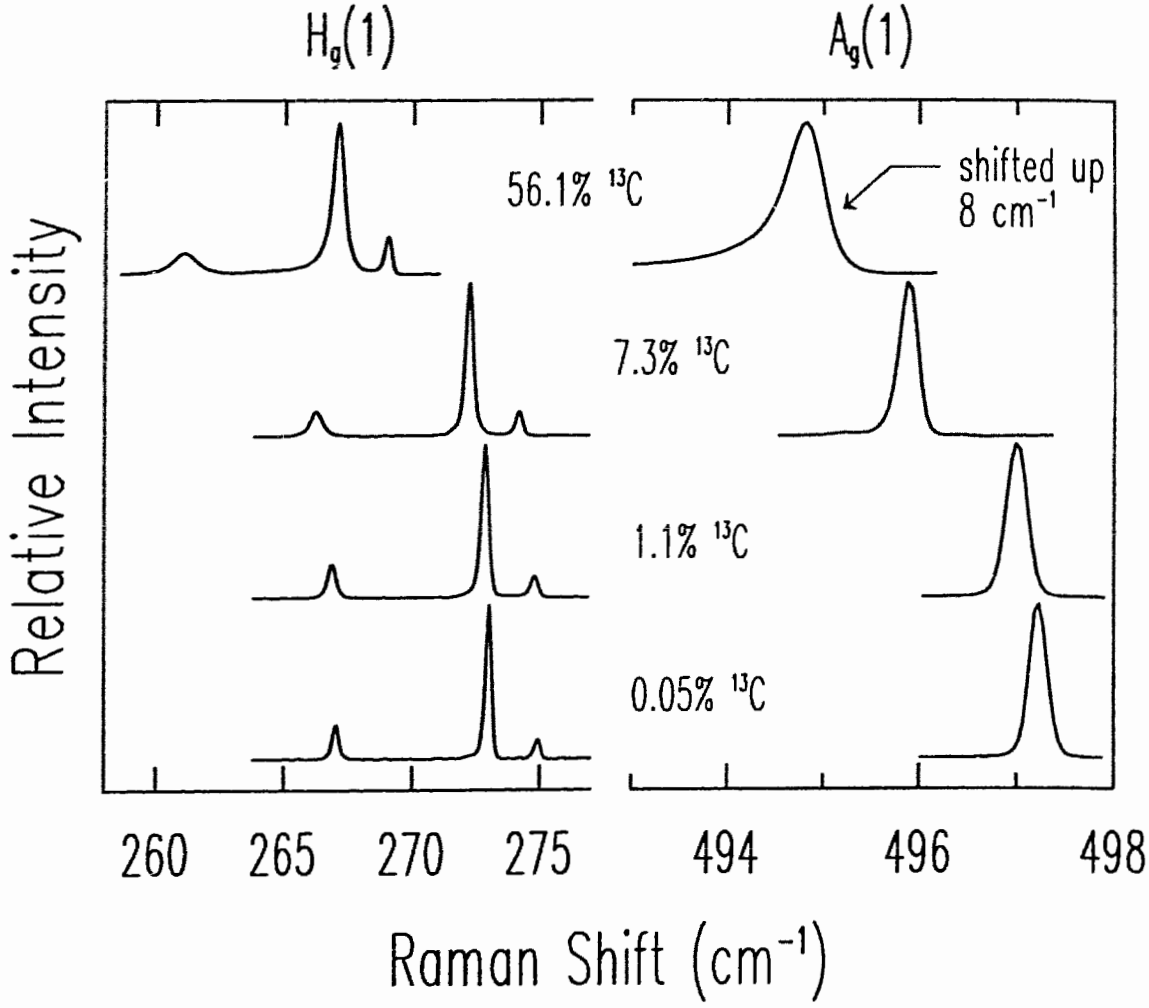

Fig. 4.11 $H_g(1)$ and $A_g(1)$ modes of crystalline C_{60} as a function of isotope content; T=2 K. The $A_g(1)$ spectrum of the 56.1% ^{13}C C_{60} crystal has been shifted upward in energy by 8 cm^{-1}.

data on the phonon modes did not exist prior to this work, and because an analysis of the vibrational dynamics of a crystal which possesses a 240 atom basis is sufficiently difficult assuming only a perfectly ordered crystal. But having proven that splittings of the intramolecular phonons due to the complete crystal field of the solid are observable, and indeed widely present, it now remains to be explored what differentiation can be made within the phonon fine-structure between the influence of a perfectly ordered solid and that of merohedral disorder.

As was done in the investigation of the intermolecular phonon spectrum, the impact of merohedral disorder on the intramolecular phonons can be experimentally probed via sample quenching. Below the glass transition temperature (~90 K), the residual concentration of misoriented molecules will be a function of how quickly the sample was brought out of equilibrium, i.e. the rate at which the sample was cooled through the glass transition temperature. Varying the merohedral disorder of the crystal in this manner affects the majority of the intramolecular phonon fine-structure, as shown in Figure 4.12. In Fig. 4.12a), six phonon bands of crystalline $^{12}C_{60}$ at 2 K are shown for two different cooling rates. Crystalline $^{12}C_{60}$ spectra are used in Fig. 4.12 since the fine-structure components are generally sharper and there is less background, while the pronounced isotope effects on $A_g(2)$ can be ignored. The slow quench corresponded to cooling the crystals from room temperature to 85 K over the span of 12 hours, and then cooling to 2 K, while the fast quench involved dropping the crystals directly from room temperature into superfluid helium. All of the modes shown in Fig. 4.12 display a dependence upon the quench rate, to varying degrees. Very pronounced changes in the relative intensities of $G_g(1)$, $H_g(4)$, and $A_g(2)$ fine-structure are evident, while the changes in $H_g(3)$, $H_g(6)$, and $H_g(7)$ are less dramatic. Although not shown in Fig. 4.12, the relative intensities of components within $H_g(2)$ and $F_{2g}(1)$ bands also display a minor dependence upon the quench rate.

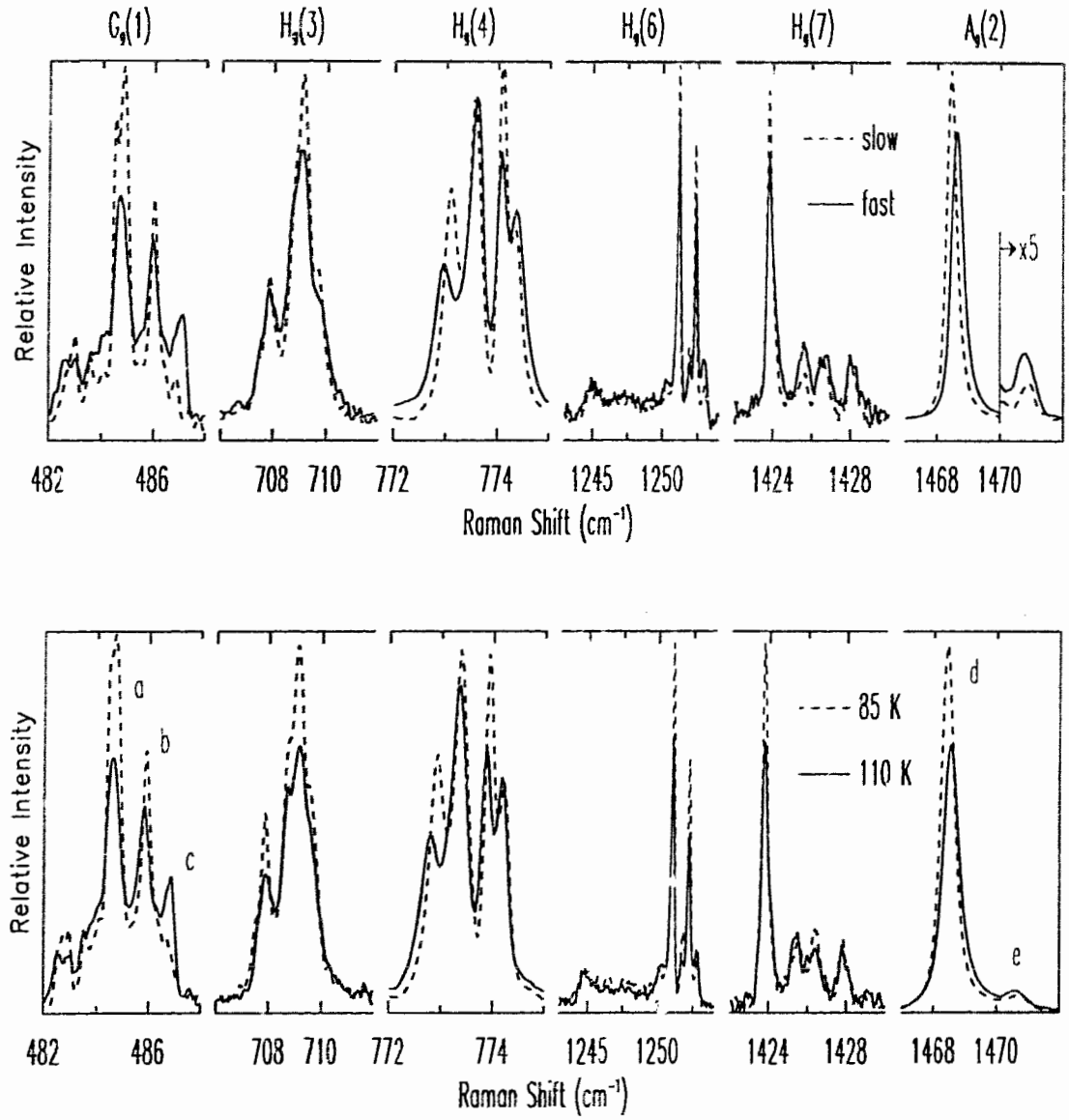

Fig. 4.12 $G_g(1)$, $H_g(3)$, $H_g(4)$, $H_g(6)$, $H_g(7)$, and $A_g(2)$ fine-structure of crystalline $^{12}C_{60}$ at T=2 K as a function of the rate of cooling into the glassy state. The 'fast' quench spectra have been scaled to the 'slow' quench spectra by matching the intensities of the $A_g(1)$ intramolecular mode which has no fine-structure in either natural or $^{12}C_{60}$. The weak, higher energy peak in the $A_g(2)$ spectra have been multiplied by a factor of 5 for clarity. See text for an explanation of fast and slow quench. Also shown are the fine-structure components for samples equilibrated at T=85 K and T=110 K.

Since the concentration of misoriented molecules increases as the sample is warmed above the glassy transition, the relative intensity changes which occur in the Raman fine-structure with quench rate should simply mirror the temperature evolution of the slowly-quenched sample above the glassy transition. This is clearly seen in Fig. 4.12b), which shows the Raman fine-structure of the samples equilibrated at 85 K and 110 K. The components within a band which grow in relative intensity as the temperature is raised are also those which show an increased intensity with the fast quench. This substantiates the assertion that the relative intensity changes seen in the Raman fine-structure with quench rate are due to the varying amounts of merohedral disorder within the crystal. The comparison between the quench rate and temperature evolution data is complicated, however, by the overall decrease of the Raman intensity of all the modes with increasing temperature. The decrease in integrated intensity stems possibly from a reduced transparency of the material with increasing temperature.

In order to directly delineate the merohedral disorder from the crystal field of a perfectly ordered crystal, it would be necessary to completely remove the residual concentration of misoriented molecules and study the phonon spectrum of the resultant crystal. Unfortunately, no means of studying this crystal structure without the presence of merohedral disorder has yet been discovered. It will be shown in Chapter 5 that a new orientational phase of solid C_{60} in which the disorder can be made arbitrarily small can be achieved through the application of hydrostatic pressure. However, the orientations of the molecules within this new phase are not those of the conventional low-temperature phase, and so the resultant phonon spectrum is obviously not that of the structure presently under consideration.

Although the merohedral disorder cannot be reduced to zero, its contribution to the Raman fine-structure can be quantified through a detailed temperature study of the fine-structure relative intensities. Shown in Figure 4.13 are the relative intensities of the $G_g(1)$ and $A_g(2)$ fine-structure (of crystalline $^{12}C_{60}$) between 85 K and 250 K. The

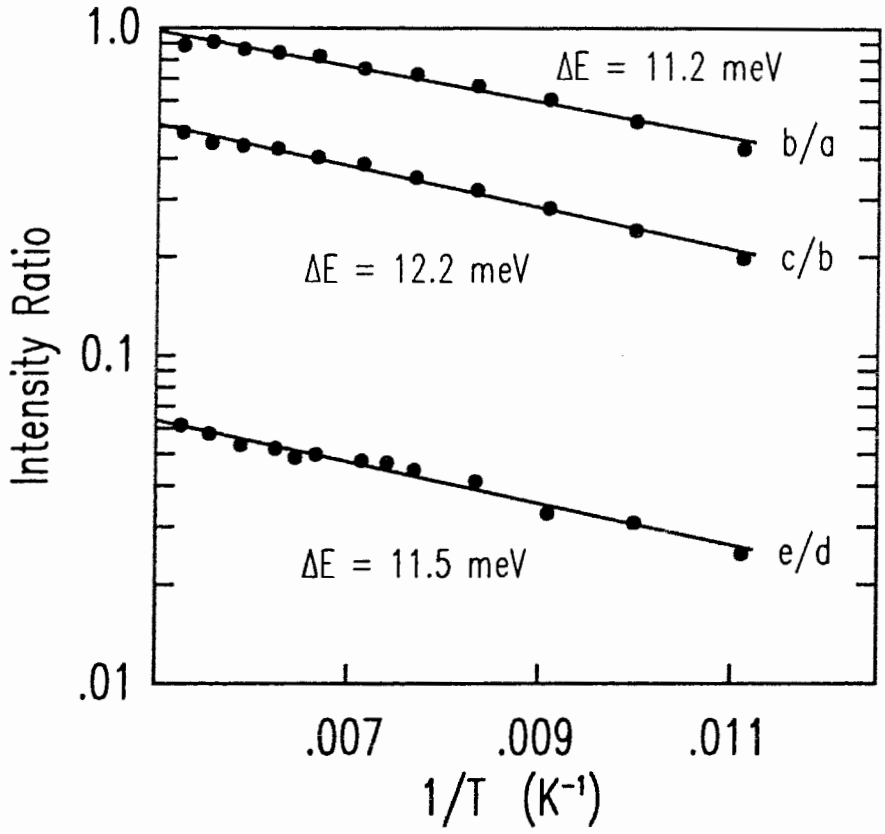

Fig. 4.13 Ratios of integrated intensities of the peaks labeled *a*, *b*, *c*, *d*, and *e* in Fig. 4.12 as a function of 1/T. The solid lines are a fit to the data using the functional form $I_{ratio} = I_o e^{-\Delta E / kT}$.

components plotted in Fig. 4.13 follow the labeling scheme used in Fig. 4.12. The solid lines in Fig. 4.13 are a fit to the intensity ratios using the functional form

$$I_{ratio} = I_o e^{-\Delta E/kT} \qquad (4.1)$$

The relative intensities of the $G_g(1)$ *b* vs *a* and *c* vs *b* components vary with an activation energy, ΔE, of 11.2 meV and 12.2 meV, respectively, while the $A_g(2)$ doublet has an activation energy of 11.5 meV. Within the estimated accuracy of ±2 meV, these values agree with the previously determined energy of a misoriented molecule of ~12 meV [92G, 92Sb, 92Yb]. The data strongly suggests, therefore, that the various components analyzed in Fig. 4.13 result directly from different numbers of misoriented nearest neighbours. For example, the *a* peak of $G_g(1)$ may result from molecules with no misoriented neighbours, the *b* peak from molecules with one misoriented neighbour, and the *c* peak from molecules with two - other possibilities could account for the increased unresolved background in the fast quench spectrum.

While the fine-structure of the $G_g(1)$ and $A_g(2)$ bands can be directly tied to the merohedral disorder, an equivalent dependence is not seen in the remaining modes shown in Fig. 4.12. While all of the modes shown in Fig. 4.12 are clearly affected by random orientational defects, no straightforward dependence can be determined. A complete description of the influence of merohedral disorder on the vibrational dynamics will therefore require a band-structure calculation which incorporates the orientational disorder in a non-trivial manner. The need to address the disorder and crystal field in a unified manner is underscored by noting that even the components of $A_g(2)$ which were proven to be activated by the ^{13}C substitutions present in natural C_{60} displayed an intensity variation with quench rate and increasing temperature above the glass transition.

The only phonon band whose fine-structure components did not display a dependence on the merohedral disorder of the low-temperature phase is the $H_g(1)$-derived band. The four components of $H_g(1)$ were independent of quench rate, and showed no temperature evolution above the glassy transition, apart from a linewidth broadening and

an overall decrease in the integrated Raman intensity, common to all the modes. The splittings of $H_g(1)$ can be therefore attributed solely to the crystal field of an ordered solid.

4.5 Summary and Discussion

Rich structure within the intramolecular phonon bands of crystalline C_{60} has been observed using Raman spectroscopy. The narrow linewidths of these modes, as small as 0.10 cm^{-1}, reveal a wealth of detail below the 260 K fcc to sc phase transition. While clear evidence of crystal field splittings in both phases is observed, the polarization measurements of the fine-structure components indicate that more than simply a factor-group splitting of the degenerate molecular vibrations has occurred. Unexpectedly, the presence of merohedral disorder in the low-temperature phase is seen to play a significant role. Very pronounced intensity changes within the intramolecular phonon bands are seen as the temperature is lowered from 260 K to ~90 K, below which temperature the relative intensities remain constant. This suggests a connection between the fine-structure and the orientational disorder of the crystal. The identification of the observed fine-structure with the merohedral disorder is strengthened by the discovery that these intensity changes can be mimicked at a fixed low-temperature by quenching the sample rapidly through the glass transition, thereby freezing in greater amounts of disorder. Through a detailed temperature study of the fine-structure components above the glass transition, activation energies for the temperature induced intensity variations of the $G_g(1)$ and $A_g(2)$ components were determined. The ~12 meV activation energy extracted from this study is in excellent agreement with the energy increase of a misoriented molecule, as previously determined by structural studies of the solid phase.

The isotopic disorder of natural C_{60} crystals was found to be a minor influence, except for the $A_g(2)$ mode, which in natural crystalline C_{60} has a complex structure quite different from that reported for isolated C_{60}. The interplay between isotope and solid state effects for the $A_g(2)$ band is not presently understood, and cannot be accounted for

within either the purely molecular treatments of the isotopic disorder which have been reported to date, or within the conventional solid state approaches in which some form of averaging of the disorder is performed by the phonon.

In closing, the possibility that portions of the splittings shown in this work stem from more rudimentary sources such as impurities must be addressed. None of the phonon fine-structure shown in this work displayed any sample to sample variation among the large number of crystals which we have produced in our lab, over a wide range of conditions. Crystals which were grown from commercial sources and from powder produced and purified in-house were found to produce identical Raman spectra. Samples which had been grown in vacuum and then transferred to a cold cryostat without breaking vacuum showed Raman fine-structure identical to that of samples which had been handled in air, as did samples subjected to multiple sublimation regrowths versus crystals grown from as-received powder. Nor was any variation in the Raman bands encountered with increasing laser irradiance (using near-infrared wavelengths), a phenomenon which is widely reported for visible excitation. The startling properties of the intramolecular phonons presented in this work are therefore clearly intrinsic to the solid.

CHAPTER FIVE

PRESSURE INDUCED STRUCTURAL METASTABILITY

5.1 Introduction

A powerful tool which can be employed to gain further insight into the orientational and rotational properties of the molecular solid is hydrostatic pressure. Hydrostatic pressure permits the continuous tuning of the strength of the intermolecular potentials and rotational barriers which control the motions of the C_{60} molecules. Results from high-pressure studies can therefore provide additional understanding of the ordering process and aid in the refinement of model intermolecular potentials.

A number of high-pressure studies have been undertaken to date, focusing predominantly on the pressure dependence of the fcc - sc ordering transition [91Sb, 93Sb, 94J]. Differential thermal analysis (DTA) [91Sb, 93Sb] and x-ray powder diffraction [94J] experiments have shown that the application of hydrostatic pressure stabilizes the ordered sc phase, leading to an increasing transition temperature with increasing pressure. The slope of the ordering transition is linear, with $^{dT_c}/_{dP} = 16.4$ K/kbar [93Sb], so that an ordered sc structure can be seen at room temperature when a pressure of ~2.4 kbar (.24 GPa) is applied. There was some initial confusion as to the true value of $^{dT_c}/_{dP}$ with values appearing in the literature varying by as much as 40%. It was quickly discovered, however, that the large interstitial sites of solid C_{60} would readily accommodate small molecules such as helium, so when used as a pressure conducting medium, the helium atoms would permeate into the lattice and reduce the observed value of $^{dT_c}/_{dP}$ [93Sb].

In the orientationally-ordered sc phase, each molecule is known to reorient between two energetically similar but crystallographically distinct orientations. The most

energetically favourable configuration is described by pentagons facing carbon-carbon double bonds in neighbouring molecules (the Γ_1 rotation angle), while the second bonding motif has hexagon faces opposing neighbouring C=C bonds (the Γ_2 rotation angle; refer to Section 1.2 for a more complete description of the orientational ordering of solid C_{60} at ambient pressure). At ambient pressure, the fraction of 'hexagon' oriented molecules is approximately 40% for temperatures near the sc - fcc phase transition temperature of 260 K. As the temperature is lowered, the fraction of misoriented molecules decreases smoothly from ~40% to ~17% at approximately 90 K, below which temperature the reorientation times become much longer than experimental time scales, and a 'static' amount of residual disorder is frozen in [92D]. From an analysis of the lattice constant behaviour at the glass transition, it was found, surprisingly, that the lower-energy 'pentagon' orientation has a larger volume than the 'hexagon' orientation [92G]. Motivated by this result, a neutron diffraction study of the orientationally ordered phase of solid C_{60} as a function of pressure was undertaken by David and Ibberson [93D]. At 150 K, they found that the relative population of the hexagon orientation increased with increasing pressure, in accordance with the finding that the hexagon orientation occupies a smaller volume. At a pressure of ~1.9 kbar, the hexagon and pentagon orientations appeared in equal proportions, while at higher pressures, the hexagon orientation became the more favourable configuration; 60% of the molecules were reported to assume this orientation by 3 kbar (at 150 K). This has significant implications for the ordering of the molecules within the crystal at higher pressures. If the free energy difference between the hexagon and pentagon configurations continues to increase with increasing pressures, then a virtually defect-free hexagon-oriented crystal may be attainable, at reasonably modest hydrostatic pressures.

In this Chapter, a new metastable phase of crystalline C_{60} is reported, stabilized by hydrostatic pressure. At pressures as low as 2 kbar, the normal low-temperature sc phase is metastable with respect to a new structure which manifests itself through very

pronounced changes in the Raman-active intermolecular and intramolecular phonon spectra. The new phase appears when the pressurized sample is warmed above a minimum temperature. Once formed, the pressure can be released and the new phase will be metastable with respect to the conventional low-temperature sc phase, provided the crystal is cooled below the (zero pressure) glass transition prior to releasing the pressure. It will be shown that the most probable explanation for these changes is a purely orientational transformation resulting from the pressure-induced lowering of the energy of the hexagon orientation relative to the pentagon orientation. At even modest pressures (12 kbar), the energy difference between hexagon and pentagon orientations is projected to be large enough that the concentration of misoriented molecules (now misoriented refers to the pentagon configuration) is less than 1%. The metastability of the new phase therefore allows a near-completely ordered crystal of C_{60} to be studied at ambient pressure.

5.2 The Pressure Dependence of the Libron and Phonon Fine-Structure

The new metastable phase of crystalline C_{60} is introduced through a discussion of the pressure and temperature evolution of the intermolecular mode spectrum, which is shown on the left hand side of Figure 5.1. In Fig. 5.1a), the libron spectrum of a single crystal of C_{60} at 70 K and atmospheric pressure is shown. The low-energy Raman spectrum shown in Fig. 5.1a) is identical to those detailed in Chapter 3, apart from a reduced signal-to-noise level stemming from the smaller sample volume accommodated by the hydrostatic pressure rig. In Fig. 5.1b), the libron modes are shown after the pressure cell has been sealed and the pressure is increased to 12 kbar (still at 70 K). The two main libron peaks have slightly different pressure derivatives [95Hc], and so are now better resolved. Apart from a frequency shift of the modes, no dramatic changes have occurred in the intermolecular mode spectrum. As the temperature is raised at constant pressure, significant changes begin to take place in the spectrum. In Fig. 5.1c) it is seen

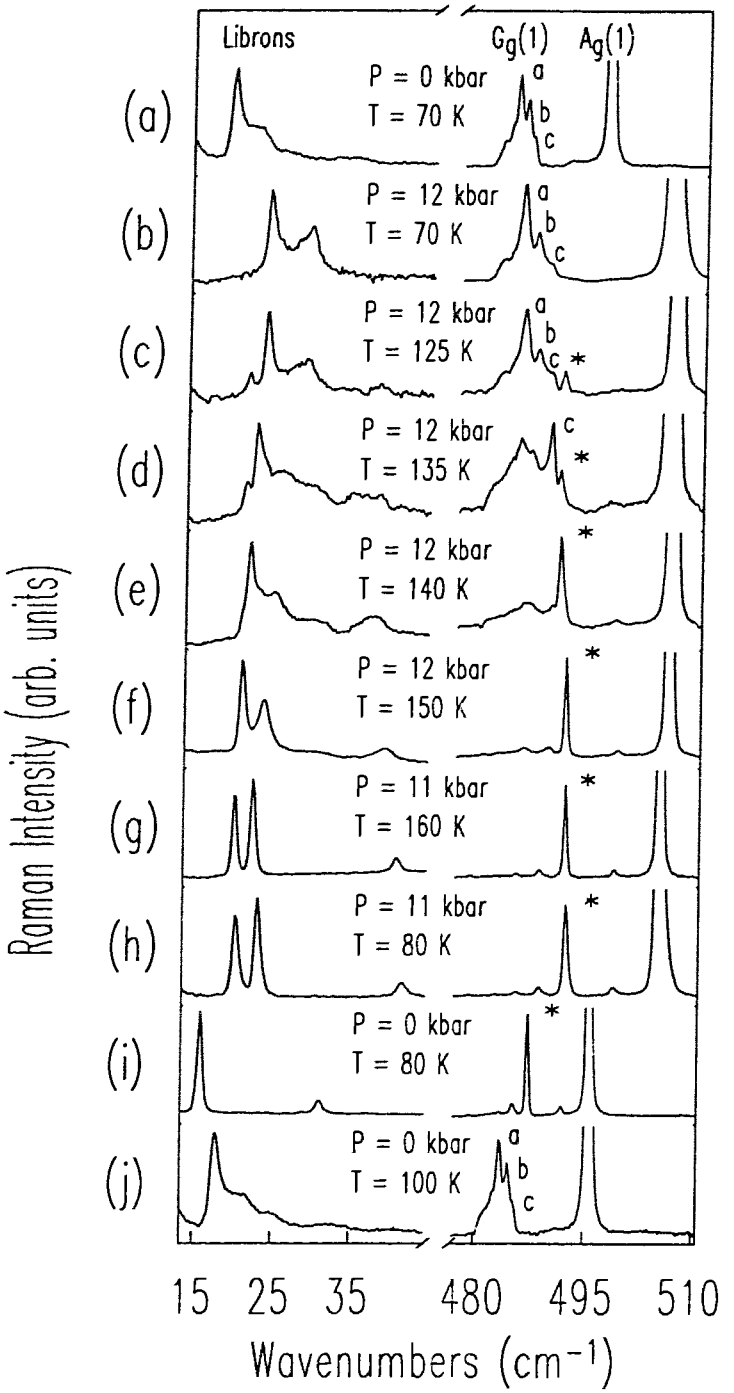

Fig. 5.1 Raman spectra covering the libron and $G_g(1)$ spectral regions (a) before sealing the pressure cell, (b) after bringing the crystal to high pressure at low-temperature, (c)-(g) then heating the sample, increasing the temperature until the normal sc to metastable phase transition is complete, (h) subsequently decreasing the temperature, (i) releasing the pressure, and (j) heating the sample until it reverts to the normal sc phase. Intensities have been scaled so that the peaks of interest are full-scale.

that at 125 K two new weak peaks have appeared: a sharp peak at lower energy than that of the 'normal' librons, and a broader peak at higher energy. At 135 K [Fig. 5.1d)], the new sharp peak is growing in intensity while the original libron peak is either softening or losing intensity to a new peak at slightly lower energy. Other broad structure is also apparent at higher energy. At 140 K [Fig. 5.1e)], the new sharp peak dominates the spectrum, and at 150 K [Fig. 5.1f)] the spectrum consists of two intense, well defined libron peaks, accompanied by a weaker third peak at higher frequency. The apparent improvement in signal-to-noise as the temperature is raised is due to very pronounced increases in the intensity of the libron peaks. By 160 K [Fig. 5.1g)], the transformation is complete. The new libron spectrum consists of two almost equal intensity modes which have peak intensities roughly 10 times stronger than the normal libron peaks at the same temperature (intensity comparisons were made relative to the $A_g(1)$ intramolecular mode), in addition to a weaker peak at 42.8 cm^{-1}. It is clear that the spectrum is entirely different from the libron spectrum of the crystal in the normal sc phase. The experimental sequence outlined in Fig. 5.1 was performed at several pressures up to 16 kbar, and the qualitative results are independent of pressure. To confirm the identification of these new peaks with lattice modes, a sample loaded at 2 kbar was heated above the order-disorder phase transition, which is ~290 K at this pressure [93Sb]. As expected, the new modes disappeared at the temperature where the C_{60} molecules began to rotate freely, and reappeared when the sample was cooled back into the ordered state.

The stability of this new phase is addressed in Figs. 5.1h) - 5.1j). If the sample is cooled to low temperature under pressure, the appearance of the spectrum is the same as at elevated temperature, as shown in Fig. 5.1h). This clearly signals that the sample is still in the new phase. If the pressure is then released at 80 K [Fig. 5.1i)], there are still no substantial changes except that the two most intense libron peaks in the new phase are now degenerate. In fact, the pressure cell can be resealed, repressurizing the crystal and

reproducing the high pressure results provided the temperature is kept below ~90 K prior to resealing the cell. If, instead, the crystal is kept at atmospheric pressure and warmed to 100 K, which is above the glass transition temperature at ambient pressure, the libron spectrum corresponding to the normal sc phase is immediately recovered, as shown in Fig. 5.1j).

Dramatic changes related to the new phase of the crystal are also seen in the intramolecular phonon spectrum. Shown on the right-hand side of Fig. 5.1 is the weakly allowed $G_g(1)$ mode. The spectrum of the normal sc phase $G_g(1)$ phonon at atmospheric pressure and low temperature is shown in Fig. 5.1a). The truncated $A_g(1)$ peak, which does not change during this transformation, is also shown (the apparent difference in the width observed for the $A_g(1)$ mode in different spectra is not real, but is an artifact of the differing intensity scales needed to normalize the structure near the $G_g(1)$ mode). The fine-structure peaks of $G_g(1)$ labeled *a, b,* and *c* follow the scheme used in Chapter 4. Upon raising the pressure to 12 kbar at low temperature [Fig. 5.1b)], the different components of the $G_g(1)$ mode merely separate due to different energy derivatives with respect to pressure. As the temperature is raised to 125 K, however, a completely new peak which is labeled (*) appears near the 'normal' $G_g(1)$ band. At 135 K, the peak labeled *c* shows a dramatic increase in intensity. As was established in Chapter 4, the relative intensity of this component is related to the amount of orientational disorder in the crystal, growing in intensity with increasing disorder. The C_{60} molecules are therefore beginning to reorient at this temperature. Clearly, the pressurized crystal was still in a glassy state, implying that just as the energy difference between the pentagon and hexagon orientations is affected by pressure, so is the reorientation barrier. As the lattice constant decreases with the application of hydrostatic pressure, the energy required for the molecules to reorient increases, causing the glass transition temperature to increase. In Figs. 5.1d) - 5.1e), significant reorientations have occurred, implying that the orientational glass transition temperature is ~140 K at 12 kbar. As the temperature is

raised to 150 K [Fig. 5.1f)], the normal $G_g(1)$ mode is almost completely suppressed with respect to the (*) peak. Several other new, less intense peaks are also evident. The transformation is complete by 160 K [Fig. 5.1g)], and the (*) peak is 4 times stronger than the normal $G_g(1)$ mode before the transformation begins (peak intensity comparisons were made relative to the $A_g(1)$ intramolecular mode). As with the librons, upon heating the crystal above the order-disorder transition temperature, the spectrum of the $G_g(1)$ mode is essentially identical to a zero pressure spectrum at that temperature, except for an energy shift. The anomalous spectrum is recovered upon cooling the sample. These results strongly suggest that the pressure-induced changes are purely orientational in nature.

As was seen in the libron mode spectrum, the new $G_g(1)$ spectrum persists at low temperature, as shown in Fig. 5.1h). The new phase is metastable with respect to the $G_g(1)$ band of the conventional sc structure at zero pressure, until the crystal is again warmed above the ambient pressure glass transition temperature, at which point the normal $G_g(1)$ is immediately recovered.

The changes seen in the intramolecular spectrum with hydrostatic pressure are not confined to $G_g(1)$; a majority of the Raman-active phonon fine-structure is transformed as the crystal enters into the new metastable phase. Shown in Figs. 5.2 and 5.3 are $H_g(2)$, $F_{2g}(1)$, $H_g(3)$, and $H_g(4)$, following the same experimental sequence as was outlined in Fig. 5.1. As can be seen from Figs. 5.2 and 5.3, the phonon fine-structure of these modes in the new metastable phase (at low T and ambient P) is quite different from that seen in the conventional (low T and ambient P) phase. As was the case with the $G_g(1)$ mode, when the pressurized crystal is warmed above the order-disorder transition temperature, all of the anomalous fine-structure shown in Figs. 5.2 and 5.3 appears identical (apart from an energy shift) to the respective bands seen in a sample in the freely rotating phase at ambient pressure.

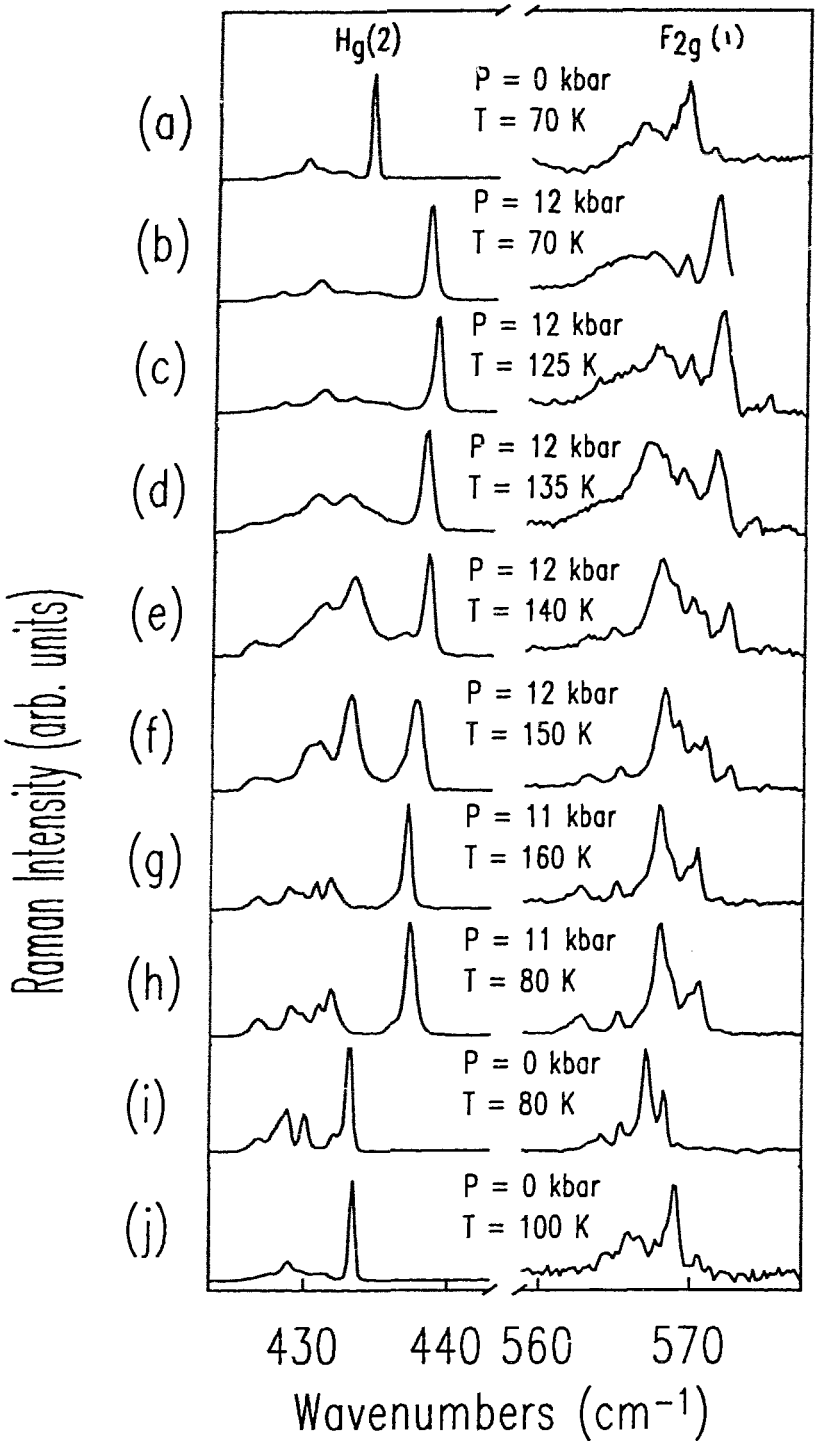

Fig. 5.2 Raman spectra covering the $H_g(2)$ and $F_{2g}(1)$ spectral regions (a) before sealing the pressure cell, (b) after bringing the crystal to high pressure at low-temperature, (c)-(g) then heating the sample, increasing the temperature until the normal sc to metastable phase transition is complete, (h) subsequently decreasing the temperature, (i) releasing the pressure, and (j) heating the sample until it reverts to the normal sc phase. Intensities have been scaled so that the peaks of interest are full-scale.

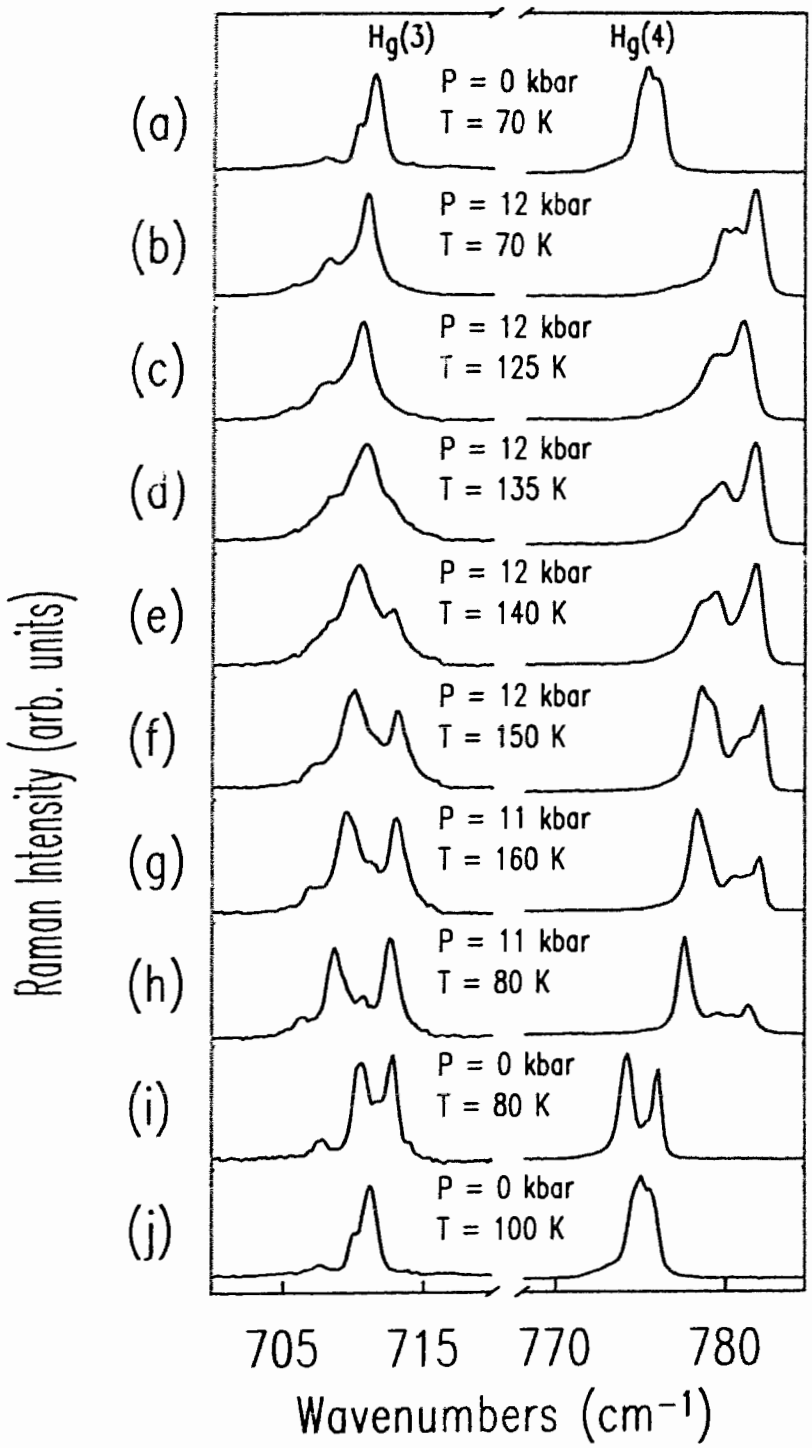

Fig. 5.3 Raman spectra covering the $H_g(3)$ and $H_g(4)$ spectral regions (a) before sealing the pressure cell, (b) after bringing the crystal to high pressure at low-temperature, (c)-(g) then heating the sample, increasing the temperature until the normal sc to metastable phase transition is complete, (h) subsequently decreasing the temperature, (i) releasing the pressure, and (j) heating the sample until it reverts to the normal sc phase. Intensities have been scaled so that the peaks of interest are full-scale.

5.3 A Model of the Pressure-Induced Metastability

In light of the x-ray diffraction study of David and Ibberson [93D] which found the energy difference between pentagon and hexagon orientations to be highly pressure-dependent, the simplest and most appealing model which accounts for the metastable phase outlined in the previous Section is that of an orientational ordering of the C_{60} molecules into the hexagon configuration with applied pressure, a configuration which becomes metastable below the glass transition temperature. The model is encapsulated schematically in Figure 5.4, which shows the experimental sequence discussed in Section 5.2 along with a graphical representation of the energy of a C_{60} molecule as a function of its orientation in the crystal. At the top of Fig. 5.4, the energy diagram for the conventional ordered sc phase of solid C_{60} is shown. At ambient pressure and below the glass transition temperature (~90 K), approximately 83% of the molecules occupy the pentagon orientation, while the remaining 17% lie 12 meV higher in energy in the hexagon orientation. This represents the minimum amount of disorder present in the sc phase, given the glass transition at ~90 K which prevents further low-temperature ordering. As the crystal is pressurized to 12 kbar, the hexagon orientation is favoured over that of the pentagon orientation. Extrapolating to 12 kbar the free energy difference between these two configurations reported by David and Ibberson [93D], the hexagon orientation should lie approximately 60 meV lower in energy at this pressure. A barrier to reorientation still exists, and since the sample has been kept at low temperature during the pressurizing, the relative populations of hexagon and pentagon orientations is not changed. The populations are qualitatively represented in Fig. 5.4 by the density of solid dots within the potential wells associated with the hexagon and pentagon orientations. As the temperature is increased at this high pressure, the molecules acquire sufficient thermal energy to overcome the reorientational barrier, and a new equilibrium ratio will be determined by the energy difference between the two configurations. As the energy difference between the hexagon and pentagon orientations is quite large (60 meV), the

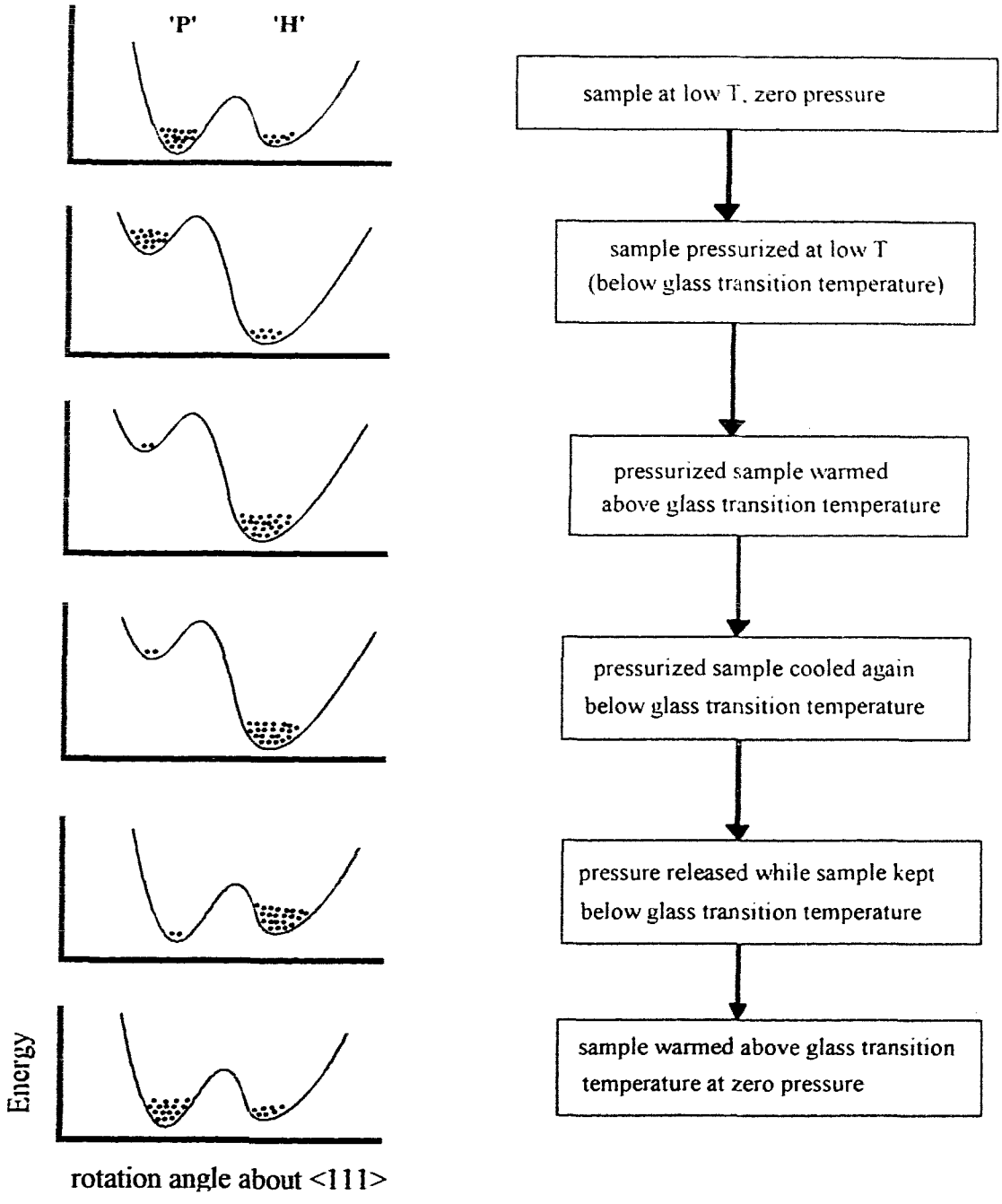

Fig. 5.4 Schematic representation of the two-state reorientation model of the pressure-induced metastability. Shown on the right are the experimental steps followed in the data presented in Figs. 5.1-5.3, while on the left, the orientational potential of a molecule within the crystal is pictorially represented at the corresponding step. The concentration of molecules within the two orientations is qualitatively depicted by the density of solid dots within each potential well.

concentration of misoriented molecules is quite small: less than 1% at 135 K. Now, however, a misoriented molecule is considered to be one which occupies a pentagon orientation, as the hexagon orientation is the ground state configuration at high pressure. Once the temperature has been fully raised above the new, high-pressure glass transition temperature, the sample may be cooled back to low temperature, and the new phase of the crystal persists. If the pressure is reduced to atmospheric once again, the orientational-energy diagram of the molecules returns to that of the conventional low-temperature phase, ie. the pentagon orientation is once again 12 meV lower in energy than that of the hexagon orientation. However, the molecules do not possess sufficient thermal energy to reorient to the new, preferred configuration, and so the large population of hexagon-oriented molecules remains metastable at zero pressure. Only by warming the crystal above the ambient-pressure glass transition temperature (~90 K), is the original ordered phase of solid C_{60} retrieved.

This model can account for the dramatic changes observed in the inter- and intramolecular Raman spectra as the temperature and pressure are cycled as outlined above, and is in accordance with the limited structural data reported for solid C_{60} under hydrostatic pressure. Further support of this orientational-ordering model of the metastable phase can be found in an experiment performed to determine the minimum pressure necessary to initiate the changes seen in the Raman fine-structure. Shown in Fig. 5.5a) are the zero pressure spectra of the librons and $G_g(1)$ mode at 130 K, a temperature which is above the glass transition. The sample was then pressurized to 0.5 kbar at 77 K, and heated back to 130 K. Even at this low pressure, it is seen in Fig. 5.5b) that changes to the $G_g(1)$ mode have already begun. The fine-structure component labeled *c* has become the most intense peak of the $G_g(1)$ band. Neutron diffraction of solid C_{60} at 0.5 kbar and 150 K found the concentration of hexagon-oriented molecules to be approximately 35% [93D]. This hexagon fraction can also be reached at atmospheric pressure by simply increasing the temperature (refer to Fig. 1.4).

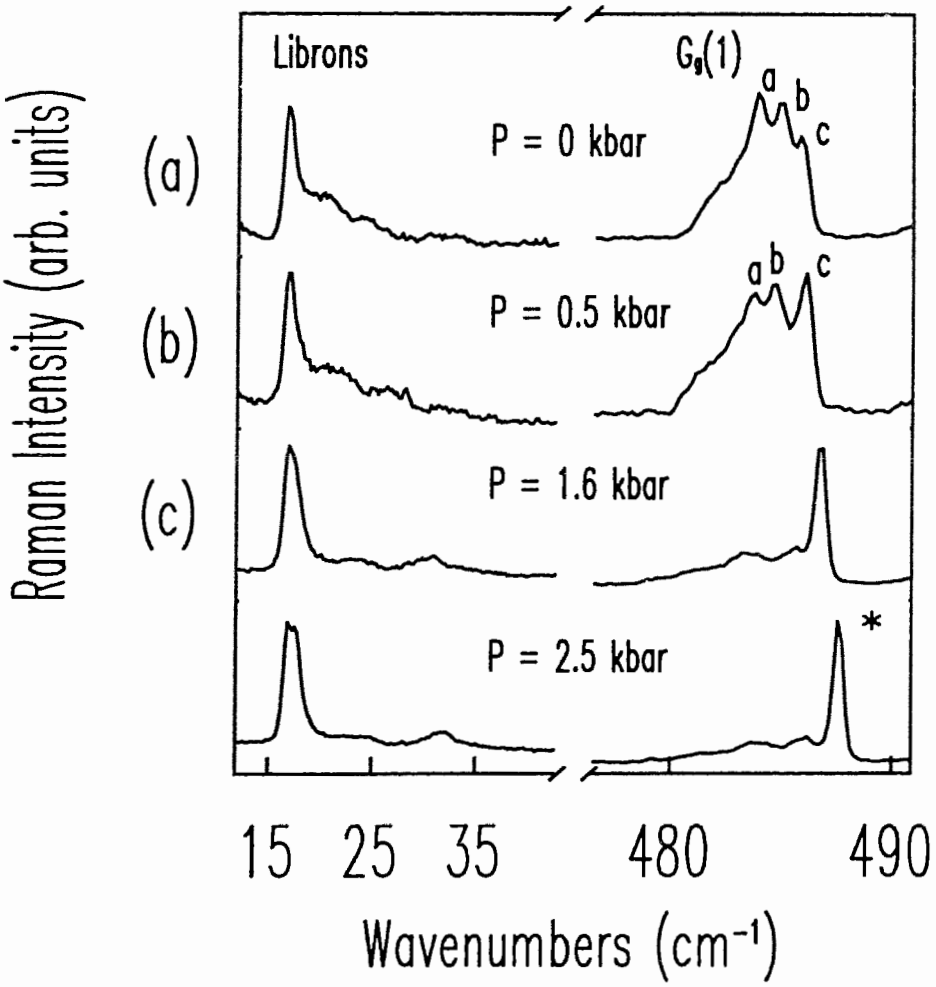

Fig. 5.5 Raman spectra of the libron and $G_g(1)$ spectral regions at 130 K (a) before sealing the pressure cell, (b) after increasing the pressure to 0.5 kbar, (c) increasing the pressure further to 1.6 kbar, and (d) 2.5 kbar. Intensities have been scaled so that the peaks of interest are full scale.

If the changes which occur in the $G_g(1)$ band at 0.5 kbar are purely from a changing pentagon-hexagon ratio, then they should also be present at atmospheric pressure at some elevated temperature. This is in fact the case, as seen in the 255 K spectrum of $G_g(1)$, shown in Fig. 4.2. As the pressure is increased to 1.6 kbar [Fig. 5.5b)], the (*) peak appears and dominates the $G_g(1)$ band, while substantial changes are also seen in the libron spectrum. By a pressure of 2.5 kbar [Fig. 5.5d)], the Raman spectra bear little resemblance to the zero pressure spectra shown in Fig. 5.5a). The proposal that the Raman fine-structure changes shown in Fig. 5.5 arise from an ordering of the molecules into the hexagon orientation is fully consistent with the neutron diffraction study of solid C_{60} under pressure by David and Ibberson, a study which found the pentagon and hexagon orientations to be degenerate at ~1.9 kbar [93D]. The normal $G_g(1)$ vibrational peaks are not fully suppressed at 2.5 kbar, nor is the broad structure between the main libron peak and the weaker peak at higher frequency fully suppressed. This is not surprising, as the hexagon orientation is only ~3.8 meV lower in energy than the pentagon orientation at this pressure, and so a significant amount of disorder (pentagon oriented molecules) is still present.

The orientational ordering deduced from the changes in the Raman bands can be summarized in an orientational 'phase diagram', as shown in Figure 5.6. The data depicted in Fig. 5.6 is not a true phase diagram, as the definition of the 'hexagon phase' is arbitrarily set as the pressure-temperature point at which the lowest energy configuration is that of the hexagon orientation, rather than the point at which a pure hexagon-oriented crystal is obtained, and similarly for the 'pentagon phase'. In Fig. 5.6, only two data points are given for the fcc-sc transition as this has been well studied by others, and we are only interested in the sc phase. The vertical dashed line marks the boundary between the low-pressure region (denoted "P") where the pentagon orientation is the ground state, and the higher-pressure region labeled "H", where the hexagon orientation becomes the ground state. At temperatures above the region defining the 'glass' transition, the two

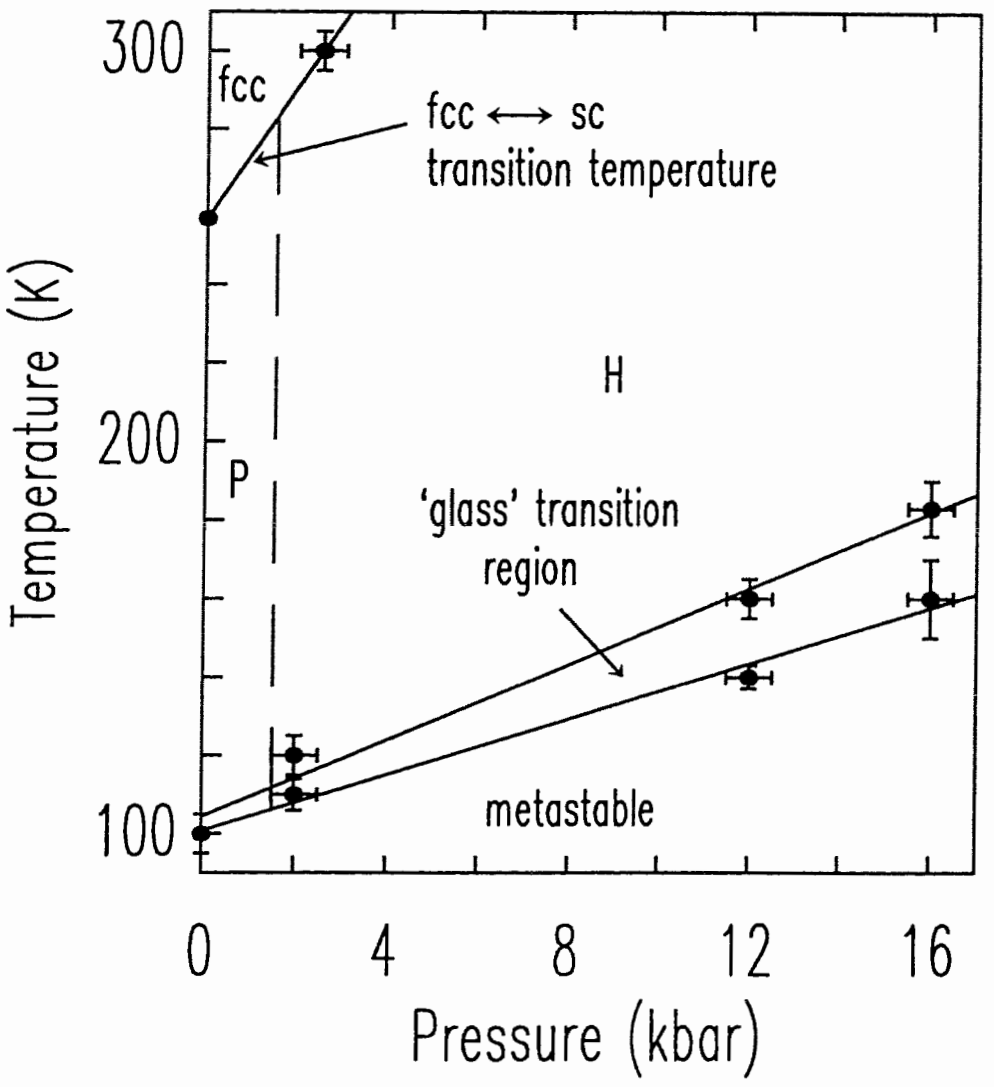

Fig. 5.6 Orientational "phase diagram" of crystalline C_{60}. "P" refers to a crystal in which a majority of the molecules are in the pentagon orientation, while "H" refers to the phase in which a majority of the molecules are in the hexagon orientation (see text for further explanations).

orientations are in thermal equilibrium (over the experimental time scales of several minutes used here), and there will be thermally activated misorientations present. The section below the glass transition region is labeled 'metastable' because once the crystal is brought into this region, the orientational order is independent of pressure and temperature until the line is again crossed.

The lower line of the 'glass' transition region was determined by pressurizing the crystal at low temperature, and then raising the temperature and noting at which temperature the changes within the Raman fine-structure began. The upper line of the 'glass' transition region shown in Fig. 5.6 was determined by noting the temperature at which the changes within the Raman fine-structure were completed. With such a definition, the pressure dependence of the upper bound of the glass transition region was determined to be 5.0 ± 0.5 K/kbar. Concurrent with the publication of this work was a report by Sundqvist *et al.* [95S] which also determined the pressure dependence of the glass transition temperature of solid C_{60}. By noting changes in the thermal conductivity of solid C_{60} as a function of temperature, they deduced the glass transition temperature of the material, and found its pressure dependence to be 5.4 K/kbar, in accordance with our determination. There is an important practical difference, however, between the results presented in this Chapter, and the results reported by Sundqvist *et al.* The thermal conductivity studies of Sundqvist *et al.* focused on cooling curves going from an equilibrium predominantly H state (hexagon oriented molecules) above T_g to a non-equilibrium but still predominantly H oriented crystal below T_g. Unfortunately, cooling curves show an increasingly smaller signature at T_g with increasing pressure, since as the pressure increases, the disorder present in the H state just above T_g is tending to zero. One can no longer observe T_g on cooling, then, as the amount of disorder above T_g becomes too small to observe experimentally. This has lead Sundqvist *et al.* to conclude that at ~7 kbar they observe a transformation to a completely hexagon-oriented crystal, and above this pressure there is no longer a glass transition. The results in this Chapter

would argue that such a conclusion is incorrect. By observing the changes which occur in the Raman spectrum as the crystal is warmed from a non-equilibrium predominantly pentagon-oriented state to an equilibrium predominantly hexagon-oriented state, the presence of a glass transition temperature is always readily observed.

5.4 Summary and Discussion

The existence of a new metastable phase of solid C_{60} has been clearly demonstrated through dramatic changes within the Raman fine-structure of the inter- and intramolecular phonon bands. While the new phase is stabilized by hydrostatic pressure, it remains metastable with respect to the conventional low-temperature sc phase of crystalline C_{60} at atmospheric pressure, provided the temperature is maintained below the glass transition temperature. Upon warming the sample above the glass transition temperature, the unpressurized crystal immediately reverts back to conventional sc phase. Similarly, when the pressurized crystal is warmed above the sc-fcc transition temperature into the freely rotating phase, the Raman bands appear identical to those of an unpressurized crystal at the same temperature (apart from a pressure-induced energy shift). These observations strongly suggest that the metastable phase involves purely a new orientational ordering of the C_{60} molecules within the sc phase. Comparison of the pressure-induced changes to those observed in the quench rate experiments discussed in Chapters 3 and 4 further corroborates the assertion that the changes are solely orientational in nature. Modes such as $G_g(1)$ which are seen to be strongly affected by disorder at ambient pressure also undergo dramatic alterations within the new metastable structure. Conversely, modes which appear unaffected by orientational disorder at ambient pressure are also seen to be largely unaffected by the pressure-induced restructuring. Specifically, the $A_g(1)$ and $H_g(1)$ bands have not been discussed in this Chapter because they undergo no change during the pressure-induced transformation.

This is similar to the results seen in the quench rate experiments detailed in Chapter 4, where the $A_g(2)$ and $H_g(1)$ bands were shown to be unaffected by orientational disorder.

CHAPTER SIX

CONCLUSION

6.1 Experimental Considerations

The results presented in this thesis were made possible by exploiting the transparency of crystalline C_{60} to wavelengths longer than its optical bandgap, which lies within the visible wavelength range. Well-resolved Raman features were obtained through the exclusive use of near-infrared laser excitation. The transparency of the material to these wavelengths permitted the use of greater excitation densities than would have been possible using visible sources, prevented sample fluorescence from underlying the Raman bands of interest, and led to increased Raman signals due to the larger volume of sample which was probed. Another invaluable experimental tool used in this work proved to be the atomic vapour filter. By tuning the laser wavelength to match the absorption filter rather than matching conventional filters to a fixed laser wavelength, a filtering technique was found which completely prevented elastically scattered light from saturating the detectors while still appearing transparent to extremely small wavelength shifts. This was essential in the study of the low-energy, weak intensity lattice modes, particularly during the hydrostatic pressure experiments. Due to the extremely small sample sizes which could be accommodated within the pressure rig, the highly sensitive CCD detector was needed in conjunction with the high throughput attained by using only a single stage of dispersion. Only in tandem with the atomic vapour filter could such an experimental configuration be used to observe the libron modes.

6.2 The External Modes

The first optical observation of libron modes in solid C_{60} has been presented in this work, showing the external phonons to be much sharper than suggested by inelastic neutron scattering measurements, and richly structured. The low-energy bands seen in Raman scattering have been unequivocally assigned to lattice modes of C_{60} through the study of isotopically pure $^{12}C_{60}$ and $^{13}C_{60}$ crystals, thereby resolving the theoretical debate as to whether libron modes in solid C_{60} could ever be observed using Raman spectroscopy.

The low-energy bands seen in Raman scattering display structure beyond what is expected from a group-theoretical analysis of the ordered sc phase. None of the structure was found to arise from the isotopic disorder present in solid C_{60} made from naturally abundant carbon, but the Raman fine-structure was found to be sensitive to orientational defects. Pronounced changes within the phonon bands were seen as varying amounts of orientational disorder were incorporated into the low-temperature structure. This, in addition to the hydrostatic pressure experiments which found the highly ordered metastable phase of C_{60} to produce a substantially simplified libron spectrum, strongly suggests that the additional fine-structure arises from the orientational disorder of the conventional sc phase. Whether the structure stems from splittings of the otherwise degenerate libron modes or from a Raman-activation of the translational modes cannot be determined unequivocally within the confines of this study. However, the large energy shift between the weaker intensity bands and the stronger peaks argues against a splitting of the main modes. Conversely, the close agreement between some of the weaker Raman peaks and the energy of the translational phonons measured using infrared absorption does suggest that the translational phonons are the origin of the additional Raman structure. Clearly, further theoretical modeling of the intermolecular interactions is required, with an emphasis on the inclusion of orientational disorder.

6.3 The Internal Modes

The phonon modes which arises from the intramolecular vibrations of C_{60} have also been shown to be much sharper in energy than previously believed, and richly structured. As was found with the external modes, the intramolecular phonon fine-structure is strongly affected by orientational defects. A number of fine-structure components were shown to arise directly from the seemingly inescapable inclusion of misoriented molecules within the low-temperature structure. For the bulk of the vibrational fine-structure, however, the deconvolution of 'normal' crystal field splittings and the influence of orientational disorder was not possible. The influence of isotopic disorder was shown to vary widely within the phonon spectrum; increasing disorder caused lower energy modes such as $H_g(1)$ and $A_g(1)$ to merely shift and broaden in energy, while the $A_g(2)$ mode displayed very pronounced splittings. The uniform softening of phonon modes with increasing ^{13}C content can be accounted for quite readily in terms of an averaging of the atomic masses present in the crystal, while the response of the $A_g(2)$ band is presently not well-understood

Purely molecular approaches have been sufficient for describing the coarse features of the intramolecular mode spectrum, but the splittings discovered in this work and the complicated dependence upon orientational and isotopic disorder they display clearly indicate that future theoretical descriptions of the solid must address the intramolecular and intermolecular interactions in a unified manner. Certainly the complex interactions among the orientational disorder, isotopic disorder, and the crystal field of the ordered solid suggest that the vibrational properties of C_{60} remains a fertile field for future theoretical and experimental research.

6.3 Pressure Induced Metastability

The phase diagram of solid C_{60} has been shown to be richer than previously known with the discovery of a pressure-induced metastable phase. The metastability is

proposed to arise from a two-state orientational transformation, a model which accounts for the bulk of the experimental observations and is consistent with previous structural studies of solid C_{60} under hydrostatic pressure. The metastable phase is assumed to consist of an ordered crystal of C_{60} molecules within the so-called hexagon configuration.

Finally, the metastability of the new phase provides a recipe for preparing a highly ordered crystal of C_{60}, a state which was not previously available to experimentalists.

REFERENCES

[95H] P. J. Horoyski, M. L. W. Thewalt, and T. R. Anthony, Phys. Rev. B **52**, R6951 (1995).

[95Hb] P. J. Horoyski and M. L. W. Thewalt, accepted for publication in Phys. Rev. B, (1995).

[95Hc] P. J. Horoyski, M. L. W. Thewalt, and T. R. Anthony, Phys. Rev. Lett. **74**, 194 (1995).

[95Hc] P. J. Horoyski, J. A. Wolk, and M. L. W. Thewalt, Solid State Commun. **93**, 575 (1995).

[95M] M. C. Martin, J. Fabian, J. Godard, P. Bernier, J. M. Lambert, and L. Mihaly, Phys. Rev. B **51**, 2844 (1995).

[95R] A. Rosenberg and C. Kendziora, Phys. Rev. B **51**, 9321 (1995).

[95S] B. Sundqvist, O. Andersson, A. Lundin, and A. Soldatov, Solid State Commun. **93**, 109 (1995).

[95W] J. A. Wolk, P. J. Horoyski, and M. L. W. Thewalt, Phys. Rev. Lett. **74**, 3483 (1995).

[95Wb] Y. Wang, J. M. Holden, A. M. Rao, P. C. Eklund, U. D. Venkateswaran, D. Eastwood, R. L. Lidberg, G. Dresselhaus, and M. S. Dresselhaus, Phys. Rev. B **51**, 4547 (1995).

[94B] W. S. Basca and J. S. Lannin, Phys. Rev. B **49**, 14750 (1994).

[94Bb] B. Burger and H. Kuzmany, in *Proceedings of the International Winterschool on Electronic Properties of Novel Materials* (edited by H. Kuzmany *et al.*), Springer, Berlin, 1994.

[94G] S. Guha, J. Menendez, J. B. Page, G. B. Adams, G. S. Spencer, J. P. Lehman, P. Giannozzi, and S. Baroni, Phys. Rev. Lett. **72**, 3359 (1994).

[94H] P. J. Horoyski and M. L. W. Thewalt, Appl. Spectrosc. **48**, 843 (1994).

[94J] A. P. Jephcoat, J. A. Hriljac, L. W. Finger, and D. E. Cox, Europhys. Lett. **25**, 429 (1994).

[94S] R. Saito, G. Dresselhaus, and M. S. Dresselhaus, Phys. Rev. B **50**, 5680 (1994).

[94Y] T. Yildirim, in *Proceedings of the International Winterschool on Electronic Properties of Novel Materials* (edited by H. Kuzmany *et al.*), Springer, 1994.

[94Yb] J. Yu, L. Bi, R. K. Kalia, and P. Vashishta, Phys. Rev. B **49**, 5008 (1994).

[93D] W. I. F. David and R. M. Ibberson, J. Phys.: Condens. Matter **5**, 7923 (1993).

[93Db] Z. H. Dong, P. Zhou, J. M. Holden, P. C. Eklund, M. S. Dresselhaus, and G. Dresselhaus, Phys. Rev. B **48**, 2862 (1993).

[93F] S. A. FitzGerald and A. J. Sievers, Phys. Rev. Lett. **70**, 3175 (1993).

[93H] P. J. Horoyski and M. L. W. Thewalt, Phys. Rev. B **48**, 11446 (1993).

[93I] A. Ito, T. Morikawa, and T. Takahashi, Chem. Phys. Lett. **211**, 333 (1993).

[93M] M. Matus and H. Kuzmany, Appl. Phys. A **56**, 241 (1993).

[93N] F. Negri, G. Orlandi, F. Zerbetto, G. Ruani, A. Zakhidov, C. Taliani, K. Kinuchi, and Y. Achiba, Chem. Phys. Lett. **211**, 353 (1993).

[93S] D. W. Snoke and M. Cardona, Solid State Commun. **87**, 121 (1993).

[93Sb] G. A. Samara, L. V. Hansen, R. A. Assink, B. Morosin, J. E. Schirber, and D. Loy, Phys. Rev. B **47**, 4756 (1993).

[93Sc] R. Saito, G. Dresselhaus, and M. S. Dresselhaus, Chem. Phys. Lett. **210**, 159 (1993).

[93W] X. Q. Wang, C. Z. Wang, and K. M. Ho, Phys. Rev. B **48**, 1884 (1993).

[93Wb] K. A. Wang, A. M. Rao, P. C. Eklund, M. S. Dresselhaus, and G. Dresselhaus, Phys. Rev. B **48**, 11375 (1993).

[93Y] J. Yu, R. K. Kalia, and P. Vashishta, Appl. Phys. Lett. **63**, 3152 (1993).

[93Z] P. Zhou, Z. H. Dong, A. M. Rao, and P. C. Eklund, Chem. Phys. Lett. **211**, 337 (1993).

[92C] C. Coulombeau, H. Jobic, P. Bernier, C. Fabre, D. Schutz, and A. Rassat, J. Phys. Chem. **96**, 22 (1992).

[92D] W. I. F. David, R. M. Ibberson, T. J. S. Dennis, J. P. Hare, and K. Prassides, Europhys. Lett. **15**, 295 (1992).

[92Db] V. N. Denisov, B. N. Mavrin, G. Ruani, R. Zamboni, and C. Taliani, Sov. Phys. JETP **75**, 158 (1992).

[92Dc] G. Dresselhaus, M. S. Dresselhaus, and P. C. Eklund, Phys. Rev. B **45**, 6923 (1992).

[92F] J. L. Feldman, J. Q. Broughton, L. L. Boyer, D. E. Reich, and M. D. Kluge, Phys. Rev. B **46**, 12731 (1992).

[92G] F. Gugenberger, R. Heid, C. Meingast, P. Adelmann, M. Braun, H. Wühl, M. Haluska, and H. Kuzmany, Phys. Rev. Lett. **69**, 3774 (1992).

[92H] P. A. Heiney, J. Phys. Chem. Solids **53**, 1333 (1992).

[92Hb] S. Huant, J. B. Robert, G. Chouteau, P. Bernier, C. Fabre, and A. Rassat, Phys. Rev. Lett. **69**, 2666 (1992).

[92I] R. Indralingam, J. B. Simeonsson, G. A. Petrucci, B. W. Smith, and J. D. Winefordner, Anal. Chem. **64**, 964 (1992).

[92J] R. A. Jishi, R. M. Mirie, and M. S. Dresselhaus, Phys. Rev. B **45**, 13685 (1992).

[92Jb] Q. Jiang, H. Xia, Z. Zhang, and D. Tian, Chem. Phys. Lett. **192**, 93 (1992).

[92K] R. F. Kiefl, J. W. Schneider, A. McFarlane, K. Chow, T. L. Duty, S. R. Kreitzman, T. L. Estle, B. Hitti, R. L. Lichti, E. J. Ansaldo, C. Schwab, P. W. Percival, G. Wei, S. Woldek, K. Kojima, W. J. Romanow, J. P. McCauley, N. Coustel, J. E. Fischer, and A. B. Smith, Phys. Rev. Lett. **68**, 1347 (1992).

[92L] J. P. Lu, X. -P. Li, and R. M. Martin, Phys. Rev. Lett. **68**, 1551 (1992).

[92Lb] P. H. M. van Loosdrecht, P. J. M. van Bentum, and G. Meijer, Phys. Rev. Lett. **68**, 1176 (1992).

[92Lc] P. H. M. van Loosdrecht, P. J. M. van Bentum, M. A. Verheijen, and G. Meijer, Chem. Phys. Lett. **198**, 587 (1992).

[92Ld] X. P. Li, J. P. Lu, and R. M. Martin, Phys. Rev. B **46**, 4301 (1992).

[92Le] S. Leach, M. Vervloet, A. Despres, E. Breheret, J. P. Hare, T. J. Dennis, H. W. Kroto, R. Taylor, and D. R. M. Walton, Chem. Phys. **160**, 451 (1992).

[92N] D. A. Neumann, J. R. D. Copley, W. A. Kamitakahara, J. J. Rush, R. L. Cappelletti, N Coustel, J. E. Fischer, J. P. McCauley, A. B. Smith, K. M.

Creegan, and D. M. Cox, J. Chem. Phys. **96**, 8631 (1992).

[92Nb] F. Negri, G. Orlandi, and F. Zerbetto, Chem. Phys. Lett. **190**, 174 (1992).

[92Nc] M. K. Nissen, S. M. Wilson, and M. L. W. Thewalt, Phys. Rev. Lett. **69**, 2423 (1992).

[92Nd] F. Negri, G. Orlandi, and F Zerbetto, J. Chem. Phys. **97**, 6496 (1992).

[92O] G. Onida and G. Benedek, Europhys. Lett. **18**, 403 (1992).

[92P] K. Prassides, H. W. Kroto, R. Taylor, D. R. M. Walton, W. I. F. David, J. Tomkinson, R. C. Haddon, M. J. Rosseinsky, and D. W. Murphy, Carbon **30**, 1277 (1992).

[92Pb] L. Pintschovius, B. Renker, F. Gompf, R. Heid, S. L. Chaplot, M. Haluska, and H. Kuzmany, Phys. Rev. Lett. **69**, 2662 (1992).

[92Pc] G. Peters and M. Jansen, Angew. Chem. Int. Ed. Eng. **31**, 223 (1992).

[92Pd] D. H. Parker, K. Chatterjee, P. Wurz, K. R. Lykke, M. J. Pellin, L. M. Stock, and J. C. Hemminger, in *The Fullerenes* (edited by H. W. Kroto, J. E. Fischer, and D. E. Cox), Pergamon Press (1992).

[92Pe] M. J. Pelletier, Appl. Spectrosc. **47**, 69 (1992).

[92S] M. Sprik, A. Cheng, and M. L. Klein, J. Phys. Chem. **96**, 2027 (1992).

[92Sb] X. D. Shi, A. R. Kortan, J. M. Williams, A. M. Kini, B. M. Savall, and P. M. Chaikin, Phys. Rev. Lett. **68**, 827 (1992).

[92Sc] R. Saito, G. Dresselhaus, and M. S. Dresselhaus, Phys. Rev. B **46**, 9906 (1992).

[92T] G. van Tendeloo, S. Amelinckx, M. A. Verheijen, P. H. M. van Loosdrecht, and G. Meijer, Phys. Rev. Lett **69**, 1065 (1992).

[92V] M. A. Verheijen, H. Meeks, G. Meijer, E. Raas, and P. Bennema, Chem. Phys. Lett. **191**, 339 (1992).

[92W] D. E. Weeks, J. Chem. Phys. **96**, 7380 (1992).

[92Wb] Y. Wang, J. M. Holden, A. M. Rao, W. T. Lee, G. T. Hager, X. X. Bi, S. L. Ren, G. W. Lehman, G. T. Hager, and P. C. Eklund, Phys. Rev. B **45**, 14396 (1992).

[92Y] N. Yao, C. F. Klein, S. K. Behal, M. M. Disko, R. D. Sherwood, and D. M. Cox, Phys. Rev. B **45**, 11366 (1992).

[92Yb] R. C. Yu, N. Tea, M. B. Salamon, D. Lorents, and R. Malhotra, Phys. Rev. Lett. **68**, 2050 (1992).

[92Yc] T. Yildirim and A. B. Harris, Phys. Rev. B **46**, 7878 (1992).

[92Yd] K. Yabana and G. Bertsch, Chem. Phys. Lett. **197**, 32 (1992).

[92Z] P. Zhou, A. M. Rao, K. A. Wang, J. D. Robertson, C. Eloi, M. S. Meier, S. L. Ren, X. X. Bi, P. C. Eklund, and M. S. Dresselhaus, Appl. Phys. Lett. **60**, 2871 (1992).

[91C] R. L. Cappelletti, J. R. D. Copley, W. A. Kamitakahara, F. Li, J. S. Lannin, and D. Ramage, Phys. Rev. Lett. **66**, 3261 (1991).

[91Cb] A. Cheng and M. L. Klein, J. Phys. Chem. **95**, 6750 (1991).

[91D] W. I. F. David, R. M. Ibberson, J. C. Matthewman, K. Prassides, T. J. Dennis, J. P. Hare, H. W. Kroto, R. Taylor, and D. R. M. Walton, Nature **353**, 147 (1991).

[91Db] S. J. Duclos, R. C. Haddon, S. H. Glarum, A. F. Hebard, and K. B. Lyons, Solid State Commun. **80**, 481 (1991).

[91F] R. M. Fleming, T. Siegrist, P. M. March, B. Hessen, A. R. Kortan, D. W. Murphy, R. C. Haddon, R. Tycko, G. Dabbagh, A. M. Mujsce, M. L. Kaplan, and S. M. Zahurak, in *Clusters and Cluster-Assembled Materials* (Edited by R. S. Averback, D. L. Nelson, and J. Bernholc). MRS Symposium Proceedings No. 206, Materials Research Society, Pittsburgh (1991).

[91Fb] H. D. Fuchs, C. H. Grein, C. Thomsen, M. Cardona, W. L. Hansen, E. E. Haller, and K. Itoh, Phys. Rev. B **43**, 4835 (1991).

[91G] Y. Guo, N Karasawa, and W. A. Goddard, Nature **351**, 464 (1991).

[91H] P. A. Heiney, J. E. Fischer, A. R. McGhie, W. J. Romanow, A. M. Denenstein,

J. P. McCauley, A. B. Smith, and D. E. Cox, Phys. Rev. Lett. **66**, 2911 (1991).

[91Hb] J. B. Howard, J. T. McKinnon, Y. Marovsky, A. Lafleur, and M. E. Johnson, Nature, **352**, 139 (1991).

[91Hc] K. C. Hass, M. A. Tamor, T. R. Anthony, and W. F. Banholzer, Phys. Rev. B **44**, 12046 (1991).

[91L] S. Liu, Y. J. Lu, M. M. Kappes, and J. A. Ibers, Science **254**, 408 (1991).

[91P] K. Prassides, T. J. S. Dennis, J. P. Hare, J. Tomkinson, H. W. Kroto, R. Taylor, and D. R. M. Walton, Chem. Phys. Lett. **187**, 455 (1991).

[91S] R. Sachidanandam and A. B. Harris, Phys. Rev. Lett. **67**, 1467 (1991).

[91Sb] G. A. Samara, J. E. Schirber, B. Morosin, L. V. Hansen, D. Loy, and A. P. Sylwester, Phys. Rev. Lett. **67**, 3136 (1991).

[91T] R. Tycko, R. C. Haddon, G. Dabbagh, S. H. Glarum, D. C. Douglass, and A. M. Mujsce, J. Phys. Chem. **95**, 518 (1991).

[91Tb] R. Tycko, G. Dabbagh, R. M. Fleming, R. C. Haddon, A. V. Makhija, and S. M. Zahurak, Phys. Rev. Lett. **67**, 1886 (1991).

[90A] H. Ajie, M. M. Alvarez, S. J. Anz, R. D. Beck, F. Diederich, K. Fostiropoulos, D. R. Huffman, W. Krätschmer, Y. Rubin, K. E. Schriber, D. Sensharma, and L. Whetten, J. Phys. Chem. **94**, 8630 (1990).

[90B] E. Brendsdal, J. Brunvoll, and B. N. Cyvin, in *Quasicrystals, Networks, and Molecules of Fivefold Symmetry,* edited by I. Hargittai (VCH, New York, 1990).

[90K] W. Krätschmer,L. D. Lamb, K. Fostiropoulos, and D. R. Huffman, Nature **347**, 354 (1990).

[90T] R. Taylor, J. P. Hare, A. Abdul-Sada, and H. Kroto, J. Chem. Soc. Chem. Commun., 1423 (1990).

[89W] D. E. Weeks and W. G. Harter, J. Chem. Phys. **90**, 4744 (1989).

[88W] D. E. Weeks and W. G. Harter, Chem. Phys. Lett. **144**, 366 (1988).

[87W] Z. C. Wu, D. A. Jelski, and T. F. George, Chem. Phys. Lett. **137**, 291 (1987).

[85K] H. W. Kroto, J. R. Heath, S. C. O'Brien, R. F. Curl, and R. E. Smalley, Nature (London) **318**, 162 (1985).

[81D] W. Demtroder, *Laser Spectroscopy*, Springer-Verlag, 1985.

[78H] W. Hayes and R. Loudon, in *Scattering of Light By Crystals*, John Wiley & Sons, 1978.

[75H] R. Folland, D. A. Jackson, and S. Rajagopal, Mol. Phys. **30**, 1063 (1975).

[72F] R. A. Forman, G. J. Piermiani, J. D. Barnett, and S. Block, Science **176**, 284 (1972).

[71D] G. E. Devlin, J. L. Davis, L. Chase, and S. Geschwind, Appl. Phys. Lett. **19**, 138 (1971).

[30R] F. Rasetti, Nuovo Cimento **7**, 261 (1930).